

Faculty of Science and Engineering
Western Australian School of Mines: Minerals, Energy and Chemical
Engineering

**Effect of Stress Magnitude and Stress Rate on Elastic Properties of
the Reservoir Rocks**

Nazanin Nourifard

This thesis is presented for the Degree of
Doctor of Philosophy
of
Curtin University

June 2019

Declaration

To the best of my knowledge and belief this thesis contains no material previously published by any other person except where due acknowledgment has been made.

This thesis contains no material which has been accepted for the award of any other degree or diploma in any university.

Signature:

.....

Acknowledgements

I am always grateful for the journeys where I get to know beautiful people and gain invaluable experience, and this PhD has surely surpassed all other experiences. It is my pleasure and honour to call these people my inspiration and motivation from first teacher to last professor they all have my respect and a special place in my heart.

I wish to express my appreciation to my supervisor, Professor Maxim Lebedev, for his dedication, constant support, patience and guidance along the way. Maxim, your lab is a dream platform for rock physicists and there is no test you cannot design or perform. You are the best in this field and I am honoured to have learned rock physics from you. Thank you for taking the time to walk me through every step. I owe you my knowledge and confidence in rock physics.

My special thanks go to Professor Boris Gurevich, Professor Elena Pasternak, Dr. Mohammad Sarmadivaleh, Professor William Harbert, Dr. Eduard Mashinskii and Professor Andre Bona, for their invaluable comments and contributions. I would like to extend my sincere thanks to my fabulous editor Ms. Pia Charlotte Smith for her amazing work on proofreading this thesis.

I dedicate this thesis to my husband, Dr. Alireza Rabieh. Your authentic passion for solving problems by novel approaches is your true signature. I thank you, for your generosity in giving time to my endless questions. Being your life partner is the greatest privilege of my life. I admire your big heart and unique talent.

My sincerest gratitude goes to my wonderful parents, Farzaneh Torabi and Professor Yadollah Noorifard, who provided me with best environment to study and nourished my curiosity with passion and courage. Thank you mom and dad, you are the true gifts of my life. And my sister, Pegah Nourifard, deserves a lot of credit for her ongoing support and love. Thank you for being my sweet little guide.

Abstract

Wave propagation through a material is widely used in many applications to estimate the elastic properties of natural and engineered materials. It is well known that stress has an effect on the elastic properties of various materials; for geoscience materials in particular this effect is quite prominent. Stress can be generated by external forces and/or internally, i.e. produced by changing the pore pressure. By applying stress to rocks that are always initially anisotropic, we can influence the degree of anisotropy, at the same time, such anisotropy can be affected by different fluids inside the rocks.

Regarding the investigation of the effects of stress on elastic properties, many questions remain. In particular, (i) the link between static and dynamic moduli is still uncertain, especially for sedimentary rocks. That link is the ultimate goal for oil and gas industry, civil engineering, and mining – to predict static moduli from dynamic measurements. Such prediction is crucial for drilling, stability, production, mine safety and underground construction. In limited studies of predicting the static moduli from dynamic measurements, the measurement procedure was not done according to standards accepted in rock mechanics; moreover, this measurement were not performed simultaneously to study the comparability of static and dynamic moduli. (ii) Can stress inside a wave affect its velocity? That may be the case, because a deformation of materials produced by a propagating wave can be significant and thus such deformation may be non-linear. (iii) Stress inside the wave can be measured by emerging techniques, such as Laser Doppler Interferometry (LDI); however, the feasibility of such techniques and comparison with standard ultrasonic techniques is still under investigation. In this thesis we answer these questions.

Firstly, we designed an experiment to simultaneously measure the dynamic and static moduli of reservoir rock samples. The static moduli tests were conducted according to the International Society for Rock Mechanics standards (ISRM). The dynamic moduli were extracted from the measurement of ultrasonic P- and S-wave velocities. We found that for sandstone with porosity ranging from 8% to 24%, the dynamic Bulk moduli can be up to 44% higher than the static moduli. The results are in agreement with some, but not all of the existing empirical equations in the literature, and it has

been confirmed that by using the P-wave velocity – a non-destructive method – unconfined compressive strength value (UCS) for soft rocks can be estimated.

To quantify the effects of wave's amplitude on the longitudinal and transverse velocities in porous media, a series of experiments implementing LDI and Ultrasonic Time of Flight method were conducted. We introduced two new concepts in the experiments: Direct measurement of strain amplitude based on particle displacement on the surface of the samples, (which can be conducted by LDI techniques), and analysis of the ultrasonic transducer data, (which is measuring the rate of displacement). The results of this study show that P-wave velocity increases while S-wave velocity decreases when the P-wave and S-wave amplitude is increased.

Laboratory measurement of elastic anisotropy was performed using three plugs cut from one sample at different bedding plane orientations. We found that the anisotropy of both dry and water-saturated sandstones decreases when hydrostatic pressure is applied. Interestingly, a non-elliptical anisotropic sample in a dry state becomes elliptical after 100% saturation of this sample with water.

Finally, we conducted a detailed comparison of the LDI and ultrasonic techniques. We concluded that LDI, as the smallest receiver in the lab, can be used for the precise measurement of velocities. Moreover, the LDI signal waveforms averaged over a large area is similar to that measured by the ultrasonic transducer. We also confirmed that a shear wave transducer can be implemented as a source- and a receiver- transducer for the measurement of P-waves.

Journal articles

The following publications have resulted from the research presented in this thesis:

1. Nourifard, N., Lebedev, M., 2018, "Research note: the effect of strain amplitude produced by ultrasonic waves on its velocity": *Geophysical Prospecting*, 67, 715-722.
2. Nourifard, N., Mashinskii, E., Lebedev, M., 2019, "The effect of wave amplitude on S-wave velocity in porous media: An experimental study by Laser Doppler Interferometry": *Exploration Geophysics*, 50 683-691.
3. Nourifard, N., Pervukhinab, M., Urosevica, M., Lebedev, M., 2019, "The effects of stress and fluid on the anisotropy of reservoir rock: case study of a sandstone from the Harvey 3 CCS site, Western Australia" accepted: *Exploration Geophysics*.
4. Nourifard, N., Lebedev, M., 2020, "Bulk moduli of sandstones subjected to isotropic stress: Simultaneous static and dynamic experimental study": *Applied Geophysics*, submitted.
5. Nourifard, N., Lebedev, M., 2020, "Petrophysical analysis of Gosford sandstone using ultrasonic waves by Laser Doppler Interferometry": *Geophysical Prospecting*, Submitted.

Table of Contents

Declaration.....	ii
Acknowledgements	iii
Abstract.....	iv
Journal articles.....	vi
Chapter 1 Introduction.....	8
1.1 Research objectives.....	8
1.2 Background and motivation.....	8
1.2.1 Static and dynamic elastic moduli	9
1.2.2 Stress-induced anisotropy	10
1.2.3 Strain amplitude.....	13
1.3 Approach and chapter descriptions	15
1.4 References to Chapter One	17
Chapter 2 Static and dynamic moduli of sandstones.....	22
2.1 Foreword.....	22
2.2 Abstract.....	22
2.3 Introduction.....	23
2.3.1 Dynamic elastic moduli.....	25
2.3.2 Static elastic moduli	28
2.3.3 Dynamic and static experiments to determine elastic Young's and Bulk moduli	30
2.4 Sample preparation	30
2.5 Experimental set up	32
2.5.1 Ultrasonic equipment.....	33
2.5.2 Initial measurement of the sample before installation of the stress cell..	33
2.5.3 Uniaxial and hydrostatic (Hook's cell) set-ups	35
2.6 Method and data	37
2.6.1 Dynamic and static approaches to determining of the elastic moduli	37
2.6.2 Static set-up	41
2.7 Results and discussion	45
2.7.1 Young's modulus results in comparison with the empirical equations to predict E static.....	45
2.7.2 Bulk's modulus results from static and dynamic measurements	49
2.7.3 Comparison of static and dynamic Bulk moduli for half of the stress cycle /loading)	50

2.7.4	Pre- and Post-stress measurement on the samples (accumulated residual stress)	52
2.8	Dynamic elastic modulus experiment versus classic static elastic modulus experiment	58
2.9	Strength Analogues – Uniaxial compressive stress (UCS)	60
2.10	Conclusion and recommendations	62
2.11	References to Chapter Two	64
Chapter 3 The effect of wave amplitude on ultrasonic wave velocities in porous media		68
3.1	Foreword	68
3.2	Abstract	68
3.3	The effect of strain amplitude produced by ultrasonic waves on its velocity .	69
3.3.1	Introduction	69
3.3.2	Experiment	71
3.3.3	Results and discussion	75
3.4	The effect of wave amplitude on S-wave velocity in porous media: An experimental study by Laser Doppler Interferometry	80
3.4.1	Introduction	80
3.4.2	Materials and Methods	80
3.4.3	Results and Discussion	83
3.5	Conclusion	91
3.6	References to Chapter Three	92
Chapter 4 The effects of stress and fluid on the anisotropy of reservoir rock: case study of a sandstone from a Harvey-3 CCS site		96
4.1	Foreword	96
4.2	Abstract	96
4.3	Introduction	97
4.3.1	Literature review	98
4.4	Elastic anisotropy review	99
4.5	Closure of the pores and cracks to create isotropic background	105
4.6	Materials and Methods	108
4.6.1	Experimental set-up	110
4.6.2	Initial velocity measurement at ambient	112
4.6.3	Aluminium calibration	113
4.7	Results and discussions	114
4.7.1	Ultrasonic velocities and anisotropy	118

4.7.2	Anisotropy affected by saturation and stress	120
4.8	Conclusion	124
4.9	References to Chapter Four	125
Chapter 5 Petrophysical analysis using ultrasonic waves in porous media by Laser Doppler Interferometry		128
5.1	Foreword	128
5.2	Abstract	128
5.3	Introduction	129
5.4	Literature review	132
5.5	Method and material	134
5.5.1	Sample preparation	135
5.5.2	Experimental set-up	137
5.5.3	Experimental procedure	140
5.6	Results and discussion	142
5.6.1	Raw waveform comparison between LDI points and a pair of S-wave transducers	142
5.6.2	Shift of the P-wave polarisation of wavelets on half of the monitored area	143
5.6.3	Displacement caused by Shear-Wave Polarisation	144
5.7	Conclusion and recommendations	147
5.8	References to Chapter Five	148
Chapter 6 Conclusion		154
6.1	Summary	154
6.2	Recommendations for future work	156

Table of Figures

Figure 2-1 Stress-strain curve for the computation of Young's modulus: a) linear value measured from zero stress to a fixed percentage of ultimate strength usually up to 50% and, b) regional linear value at $50\% \pm 15\%$ of the ultimate strength.	29
Figure 2-2 Side and top view of sandstone core-plugs of Berea, Upper gray, Sister gray, Bandera gray and Castle gate after cut and before installation of the strain gauges.	32
Figure 2-3 Core-plugs of Bentheimer sandstones drilled from quarried block and prepared by installation of strain gauges on the layer of epoxy resin at the centre point.	32
Figure 2-4 The dynamic and static set-up consists of: 1) oscilloscope, 2) pulser, 3) stress frame, 4) pumps, and 5) voltmeter set attached to strain gauges on the samples.	33
Figure 2-5 Initial set-up to measure P and S velocities out of the stress cell with two types of 1 MHz transducers: P transducer and S transducer (a). The primary experiments to measure velocities outside of the pressure cell consists of : (d) measurement of the deadtime (electronics time delay) by measuring direct contact of transducers surface, (e) ultrasonic measurement of the PEEK parts with a length of 200.04 mm (top and bottom plates of PEEK); (f and b) samples have been tested by S-wave transducer, (c) samples have been tested by P-wave transducer and (g) samples have been tested by S-wave transducer while in contact of top and bottom plates of the PEEK.	34
Figure 2-6 Schematic demonstration of the uniaxial (a) and hydrostatic (b) pressure cell used in this study consists of the following parts: 1) S-wave transducer moulded inside the steel actuator for axial pressure axis, 2) PEEK top and bottom plates for best noise cancellation of wave propagation, 3) core-plunge, 4) strain gauges attached on the surface of the sample, 5) Hook's cell for applying hydrostatic pressure (the membrane inside the cell enables the access through of the high-pressure-resistant wires attached to strain gauges on the surface of the sample).	36
Figure 2-7 (a) Sample before putting into the Hook's cell, (b) Set-up during the experiment. Hook's cell parts consists of: 1) S-wave moulded transducer inside the steel actuators, 2) PEEK plates and parts for the top and bottom of the sample, and 3) Hook's pressure cell to apply hydrostatic stress by pressurized oil on the back of the membrane.	36
Figure 2-8 Hydrostatic and uniaxial experimental set-ups: (a) Hook's cell set-up for hydrostatic experiment and (b) set-up for uniaxial experiment with pressure applied on the Z-axis (all other elements of the set-up are described in Figures 6 and 7).	37
Figure 2-9 Wavelets of sample 31 on two cycles of hydrostatic experiment up to 24 MPa loading–unloading. The black wavelet in the middle of each cycle represents the	

reference wavelet at the highest applied stress. The first arrivals of P- and S-waves are marked on the graphs for the reference wavelets.....	39
Figure 2-10 (Reference wave) first arrivals picking technique used for all the experiments in this chapter. 1a and 1b are the registered first arrivals for the best sharp wavelet (usually at the highest load cycle), 2a and 2b are the best peak that is obvious and sharp enough to be detected on all wavelets at all pressures, and 3a and 3b are the second-best observable features for confirmation of first feature.....	39
Figure 2-11 Calibration experiment (a) deadtime measurement for S-wave transducers in direct contact with one another, and (2) PEEK plates and S-wave transducers in the stress frame to get the PEEK equation of the line for the correction of first arrivals once the samples are inserted in between the PEEK parts (total length of the PEEK is 200.04 mm).	40
Figure 2-12 Waveforms of the calibration test of the PEEK for both uniaxial and hydrostatic dynamic test for a full cycle of loading and unloading. The black wavelet in the middle of each cycle represents the reference wavelet at the highest applied stress. The first arrivals of P- and S-waves are marked on the graphs for the reference wavelets.....	40
Figure 2-13 PEEK calibration results (PEEK length is 200.04 mm) and the equation of the line at varying stresses for uniaxial and hydrostatic test on correction of P- and S-first arrivals.....	41
Figure 2-14 Stress-strain graph of Bentheimer sandstone in one cycle of loading and unloading.....	42
Figure 2-15 Young's modulus and Poisson's ratio of Bentheimer sandstone measured by dynamic and static set-ups simultaneously.	42
Figure 2-16 Dynamic results of Upper gray sample 31 experiment on the Vp/Vs ratio and dynamic Bulk modulus.....	43
Figure 2-17 Static Bulk modulus for sample 31 calculated on volumetric changes recorded by strain gauges.....	44
Figure 2-18 Comparison between Bulk modulus for sample 31 by dynamic and static measured simultaneously by hydrostatic experiment.	45
Figure 2-19 Measured static and dynamic Young's modulus vs the static estimated Young's modulus by empirical equations at Table 1-2.	47
Figure 2-20 Poisson's ratio measured by uniaxial experiment for both static and dynamic approaches for Berea, Bandera gray, Donny brook and PMMA samples. .	48
Figure 2-21 Static and dynamic Bulk moduli measured by hydrostatic experiment on five tested sandstones and PMMA.....	50
Figure 2-22 Bulk moduli of static and dynamic ratio for Bandera gray, Castlegate, Upper gray, Sister gray sandstones and PMMA.	51

Figure 2-23 Fifteen tested samples: P-and S-wave velocities measured before, immediately after, 20 days after and two months after loading cycles to study the effect of the relaxation of stress on velocities.	53
Figure 2-24 The plot of V_p/V_s ratio in pre- and post-stressed conditions for all the tested samples outside the stress cell.	55
Figure 2-25 Dynamic elastic Young's modulus comparison for pre- and post-stressed samples outside of the stress cell.	57
Figure 2-26 Dynamic Poisson's ratio for pre- and post-stressed samples outside of the stress cell	58
Figure 2-27 Sample 44 Berea failed on the static experiment while the dynamic results showed it did reach failure point (the surface of the sample near the strain gauges chipped, which failed the static experiment).....	60
Figure 2-28 UCS estimated values by empirical equations in Table 2-3 compared with UCS value of the samples (base lines marked in same colour solid lines).	62
Figure 3-1 (a). Experimental setup. 1: Sample, 2: Source of ultrasonic waves (piezoelectric transducer), 3: Laser Doppler interferometer (LDI), 4: laser beams (emitted and backscattered), 5: Oscilloscope, 6: Pulse generator, (b). Laser beam incident angle of 90degree on the top of the sample, (c). Schematic position of transducer as source of ultrasonic wave and Laser beam as receiver focused on the on the sample surface, (d). PMMA sample during measurement using Transducer - LDI experiment platform set up, (e). Schematic conventional setup; transducer as a source and transducer as a receiver, and (f). Measurement of PMMA sample using "conventional" setup ultrasonic platform set up.	73
Figure 3-2 Recorded signals: Top - By ultrasonic transducer; Middle – by LDI (LDI measures particle velocity) Bottom: Displacement obtained from the LDI signal. Sample Aluminium, 40 mm length, applied voltage to ultrasonic source is 400V....	74
Figure 3-3 (a) Amplitude of displacement in Aluminium cube measured by LDI and, (b). Signal recorded by ultrasonic transducer, at different voltages applied to the source transducer. No shift in wave arrival is observed.	76
Figure 3-4 Displacement of the free surface of PMMA (50 mm thickness) upon arrival of ultrasonic P-wave measured by LDI, at different voltages applied to source transducer from 100 to 400 V.	76
Figure 3-5 Recorded waveforms for Gosford sandstone for set of voltages applied to the source transducer voltages: (a). displacement of the surface upon P wave arrival measured by LDI., (b). Ultrasonic signal recording. Arrows indicate the decrease in travel time with increasing of applied voltage, and (c). First arrival signals and the shifts according to input voltages, (signals were modified to have same amplitude for illustration purpose) dark green arrow presents the shift in first arrivals.	77

Figure 3-6 P wave velocity dependence on the strain inside ultrasonic wave for Al, Gosford sandstone and PMMA. Labels inside graphs show the applied voltage to the source transducer.....	78
Figure 3-7. (a) Experimental setup. 1: S-wave transducer (Source of ultrasonic waves), 2: Sample, 3: Survey line on the top of the sample where the laser beam is emitted and scattered back, 4: Pulse generator, 5: Vibrometer Controller OFV-5000, 6: Oscilloscope, 7: Laser Doppler interferometer (LDI).....	82
Figure 3-8 (a) Raw waveform of S-transducer on centre point in three directions before matrix transformation by LDI on 400V, (b) Displacement after matrix transformation in x and z directions of S-transducer on centre point by LDI on 400V.	84
Figure 3-9 (a) Horizontal (x-axis) displacement of particles on the surface of S-wave transducer, (b) Horizontal displacement on the surface particle of Bentheimer sandstone (32 mm thickness) on the walk-away line (3 mm divisions).	85
Figure 3-10 Horizontal displacement of the particles on the surface of Bentheimer sandstone in horizontal direction (x-axis) in the walk-away experiment and at the range of applied voltages from 43V to 400V. Numbers show the maximum particle displacement for 400V and minimum particle displacement for 43V respectively...	86
Figure 3-11 Displacement of aluminium surface particles in horizontal x direction measured by LDI 3C in all applied voltages.....	87
Figure 3-12 P-wave full wavelets measured by P-transducers of Bentheimer sandstone original (left) and normalised amplitude on P first break and first peak (right) at all applied voltages.....	88
Figure 3-13 S-wave full wavelets measured by S-transducers of Bentheimer sandstone original, (The full wavelet saturation effect at peaks corresponding to 300 and 400 Volts graphs is due to measurement settings chosen to have the same accuracy).	88
Figure 3-14 S first arrival measured by S-wave transducer for Aluminium sample at all applied voltages (The full wavelet saturation effect at peaks corresponding to 300 and 400 Volts graphs is due to measurement settings chosen to have the same accuracy).	89
Figure 3-15 Velocities of Bentheimer sandstone on the first peaks measured by P- and S-wave transducers at different applied voltages to the transducers shows 0.63% increase for P velocity and 4.75% decrease for S wave velocity.....	89
Figure 3-16 (top) the dependency of P and S- waves velocities on strain amplitude measured by P and S transducers and LDI in x direction in aluminium; (bottom) in Bentheimer sandstone.	90
Figure 3-17 The dynamic Young's modulus dependence on strain amplitude measured by P and S transducers and LDI for Bentheimer sandstone.....	91

Figure 4-1 V_p and V_s subject to hydrostatic stress on dry sandstone and PMMA core samples.....	106
Figure 4-2 Raw wavelets of PMMA in the loading and unloading process. The sample displays linear elastic and following unloading the velocities of both P- and S-waves return to their original states (the red solid lines indicate the return of first arrival to the original state). For the loading the intervals sat for 2 MPa while for unloading the intervals were 10 Mpa and the sharper change is due to this change of intervals. It should be noted that wavelets have not modified for first arrivals based on equation of the line by PEEK plates.....	107
Figure 4-3 (1) Harvey-3 samples extracted in three directions: horizontal, vertical and diagonal to the deposition system; (2) mutual orthogonal cross-sectional slices, obtained from micro-CT images, field of view is 3 mm; and (3) schematic demonstration on terms parallel and perpendicular to the layering states of the samples	109
Figure 4-4 Layout of the experimental set-up: 1) Hook's cell and injection valves a) axial actuator, b) S-wave transducer, c) PEEK part, d) Hook's cell, e) input valve for fluid injection, and f) output valve for discharge and vacuum of the liquid. 2) a) hydrostatic pressure frame, b) pore pressure pump, and c) Ultrasonic bench equipment to record wavelets.	111
Figure 4-5 Initial measurement of Harvey-3 samples in the lab before being subjected to stress. (a b) vertical sample, (c d) diagonal sample, and (e f) horizontal sample. The rigid yellow line defines the noise and dotted yellow line defines the wavelet for both P- and S- transducers measurements.....	113
Figure 4-6 The equation of the line to the correct first arrival by passing through the PEEK blocks located at the top and the bottom of the tested samples.	114
Figure 4-7 Velocities of P- and S-waves at applied effective stress for dry and saturated Harvey-3 sandstones in three directions.....	115
Figure 4-8 V_p/V_s ratio changes at applied effective stresses for dry and saturated Harvey-3 sandstones in three directions.....	115
Figure 4-9 The effect of saturation on P-wave first arrivals of Harvey-3 at maximum hydrostatic effective stress (32 MPa) for horizontal, vertical and diagonal orientations.....	116
Figure 4-10 The effect of saturation on S-wave first arrivals of Harvey-3 at maximum hydrostatic effective stress (32 MPa) for horizontal, vertical and diagonal orientations.....	117
Figure 4-11 The recorded P-wave and S-wave velocities for horizontal, vertical and diagonal orientations in the hydrostatic and uniaxial experiments. Error! Bookmark not defined.	

Figure 4-12 P-wave velocities of vertical and horizontal in comparison to P-wave velocity diagonal in a dry condition.....	119
Figure 4-13 P-wave velocities of vertical and horizontal in comparison to P-wave velocity diagonal in a saturated condition.....	120
Figure 4-14 Synthetic Transverse Isotropic (TI) media (paper-reinforced phenolic material) tested as calibration to present the elliptical anisotropy based on placement of diagonal location on the elliptical of the vertical and horizontal velocity of the P-wave.	120
Figure 4-15 Comparison of P-wave anisotropies for hydrostatic condition.	121
Figure 4-16 The differences to the elliptical condition caused by the effective stress for dry and saturated conditions.....	122
Figure 5-1 a) cubic cut of 50mm Gosford sandstone, b) surface treatment with a layer of smooth epoxy resin. The measurement points have been marked on the sample for laser points with regards to the location of source transducer, c) the location of the bottom (source) S-wave transducer and the attachment to the rotational top plate, and d) 17 surface measurement points for the laser on the Gosford sample.	137
Figure 5-2 Layout of the experimental set-up consisting of LDI and ultrasonic equipment. The LDI laser beam was fixed at α for all the measured points in all directions.	138
Figure 5-3 a) free surface of the source S-wave transducer monitored by LDI to measure the raw wavelets in three directions (each 120 degrees apart and marked by the red rigid line). A is the incident angle of the laser beam collinear to the surface (horizontal surface marked by dotted black line), α kept at fixed angle for X_1 , X_2 and X_3 at 46 degrees. X_1 , X_2 and X_3 are apart from one another by 120 degrees, and, b) the raw waveform before processing to calculate the displacement. The first arrival of these three wavelets (3.9 μ s) is also the indication of system dead-time and will be used to correct the time of first arrival once the sample is attached to the source transducer.	139
Figure 5-4 a) the particle displacement on the free surface of the source S-wave transducer, which has been calculated from LDI raw wavelets and by matrix transformation converted to the Cartesian coordinate system of X,Y, and Z. b) calculated displacement in three Cartesian coordinate system as the indication of particle displacement in nanometres on the surface of the free transducer. This S-wave transducer will later be attached to the bottom of the sample as the source of ultrasonic wave.	140
Figure 5-5 Seventeen measurement points on the surface of the Gosford sandstone divided into two orbits: inner orbit, representative of the area with the same diameter as the ceramic piezoelectric ceramics disk of the source transducer, and outer orbit, the	

area at the far edges of the source transducer zone on the opposite face of the sample.	141
Figure 5-6 Averaging of LDI raw waveforms in three individual directions (3C measurement) vs raw waveform recorded by ultrasonic transducer measurement. X2 and X3 measurement can be compared with parallel S-wave polarisation conducted by a pair of transducers, and X1 is comparable with perpendicular polarisation of S-waves for a pair of S-wave transducers.....	143
Figure 5-7 the recorded raw wavelets showing positive and negative P-poles of the source transducer.....	144
Figure 5-8 The recorded displacement by S-wave transducer in X axis on the surface of cubic Gosford sandstone (the counter values are in nanometres). The location of measuring points are mapped in Figure 5-7.....	145
Figure 5-9 The recorded displacement by S-wave transducer in Y axis on the surface of cubic Gosford sandstone (the counter values are in nanometres) The location of measuring points are mapped in Figure 5-7.....	146
Figure 5-10 The recorded displacement by S-wave transducer in Z axis on the surface of cubic Gosford sandstone (the counter values are in nanometres). The location of measuring points are mapped in Figure 5-7.....	147

List of Tables

Table 2-1 Properties of the tested samples in this study (UCS values for the Berea family have been extracted from kiptonquarry.com).....	31
Table 2-2 The proposed linear and nonlinear empirical equations for sandstone to estimate the static Young's modulus.....	46
Table 2-3 Empirical equations used in this study to estimate the UCS value for tested samples based on the velocity of P-wave measured at ambient.....	61
Table 4-1 Harvey-3 samples' properties in three directions.....	108
Table 5-1 Average elastic properties and mineralogical content of tested Gosford sandstone.....	135
Table 5-2 Normal Laboratory Testing Conditions (After Aydin, 2015; ASTM Standard D2845-08).....	142

Chapter 1 Introduction

1.1 Research objectives

The main objective of this research is to better understand the effect of stress magnitude and stress rate on the elastic properties of reservoir rocks. Our study is based on data we extracted using novel rock physical approaches. These approaches were well controlled and well documented and can also be used for future rock physics projects. The general objectives and specific goals of this research are:

- 1- To gain an understanding of the relationship between the static and dynamic elastic moduli of sandstones via detailed, petrophysical experiments, and to calibrate and extend the current empirical equations with data recorded in our study.
- 2- To investigate strain amplitude, which is the main reason for the difference between the static and dynamic elastic moduli (large strain magnitude difference) by the use of Laser Doppler Interferometry (LDI) technique.
- 3- To determine experimentally the effects of stress-induced anisotropy on wave propagation data for a typical rock physics sample versus a typical reservoir rock by analysing the velocities in three directions to determine and investigate the anisotropy parameters.
- 4- To investigate the effect of the receiver size and location on the recorded ultrasonic velocities, specifically amplitude versus offset, and to differentiate with the average velocity recorded by conventional receivers on a lab scale.

The main challenges and motivations for the objectives listed above are outlined in the following sections.

1.2 Background and motivation

This section provides an overview of rock physical approaches to determine the elastic properties of sandstones in the course of induced stress. Section 1.2.1 summarises static and dynamic elastic moduli, and the relationship between them and describes the main causes of such difference. Section 1.2.2 describes the stress-induced anisotropy in reservoir rocks and the effect of saturation on anisotropy parameters, as well as previous studies on this subject.

1.2.1 Static and dynamic elastic moduli

An accurate estimation of the elastic moduli and strength of a material using non-destructive techniques is extremely important for all engineering designs and, in particular, rock mechanics projects such as hydraulic fracturing. Evaluation of the dynamic elastic moduli is an affordable, non-destructive and well-trusted approach to estimate the elastic moduli of the samples. These compelling reasons are a strong motivation to expand the research into implementing such experiments and more thoroughly understanding. Therefore, multiple studies have investigated the relationship between material static and dynamic moduli (Ide 1936; Sutherland 1962; King 1983; Vanheerden 1987; Eissa and Kazi 1988; Christaras et al. 1994; Lacy 1997; Nur and Wang 1999; Horsrud 2001; Martinez et al. 2012; Najibi et al. 2015; Brotons et al. 2014, 2016).

A classic study by Lama and Vutukuri (1978) showed that the dynamic Young's modulus can be up to 300 percent higher than the corresponding static modulus (McCann and Entwisle 1992). In modern studies this percentage has been recorded at about 40 percent. This sheds light on one of the reasons behind this difference, which could be the technology of extracting the dynamic modulus and, to be more specific, the knowledge behind wave propagation and the correct estimation of velocities, which has improved over the years of experimental rock physics. Although numerous experimental results in the literature indicate that the static Young's modulus is smaller than the dynamic modulus (Vovk 1971; Rabotnov 1979; Tutuncu et al. 1998; Mashinsky 2003), the static Poisson's ratio is reported to have a higher, lower or equal value with regards to the dynamic Poisson's ratio (Howarth 1984) . The main physical cause of this difference has been unclear for many years and remains under investigation. Understanding this difference is quite important in theoretical and practical applications, such as hydraulic fracturing problems and so on (Gik 1997, 2000). This discrepancy between the static and dynamic elastic moduli may be related to differences in elastic wave frequency and strain amplitudes in which each approach calculated (Tutuncu et al. 1998). The dynamic Young's moduli calculated from ultrasonic experimental measurement using ultrasonic elastic waves between 100 kHz–1 MHz are higher than log-derived moduli measured at 10–20 kHz, and these two measured moduli possess a higher value than the low-frequency and static moduli:

$E_{\text{ultrasonic}} > E_{\text{log}} > E_{\text{lowfrequency}} > E_{\text{static}}$ (Mashinsky 2003). Porous material such as sandstone becomes stiffer once the frequency of applied strain increases; consequently, this leads to the modulus increase. In static experiments we deal with low strain rates; however, in dynamic measurement (strain amplitude) this rate can be above critical values (Mashinsky 1994, 2001).

The objective of this study is to develop a better understanding of the static and dynamic moduli in reservoir rocks by simultaneous, controlled laboratory measurements of both moduli at equal stress rates.

1.2.2 Stress-induced anisotropy

Anisotropy is defined as a variation of a physical property depending on the measurement direction; however, it is not the same as heterogeneity. Heterogeneity is defined as a lack of spatial uniformity (Sheriff 2002). Although these two terms describe different phenomena they are related to one another. All heterogeneous materials are anisotropic to a certain degree (Winterstein 1990). In other words, ordered heterogeneity which is smaller than the seismic wavelength increases the anisotropy of the material. Anisotropy plays a major role in controlling seismic wave velocities. If this parameter is not considered, an error arises in the processing or inversion of seismic data, resulting in incorrect reflection amplitude and travel-times and incorrect interpretations (Gavin 2015). Anisotropy has been treated as both an undesirable complication (Helbig and Thomsen 2005) and a great detector for hidden small features (smaller than the seismic wavelength) (Thomsen 2002).

When speaking of geo-material, and in particular rocks, we cannot expect homogeneity because rock consists of a random or oriented distribution of grains, pores, fractures and mineral crystals. In addition rock fabric or mineral alignment can result from burial and compaction processes following deposition. Even for the so-called isotropic rocks there is not a unique pattern or identical inner structure due to the multiple geological events over the course of geological times. The arrangement and composition of the mineral frameworks and pore topologies determines P- and S-wave velocities. The change of wave signature (wavelets) allows us to detect the inner structure change on a micro scale depending on the transmitted seismic wavelength.

The velocity of sandstones depends on: 1) Porosity (Wyllie et al. 1956, 1958); 2) effective pressure (Eberhart-Philips et al. 1989); 3) degree of cementation (Dvorkin and Nur 1996; Avseth et al. 2003 and 2005); 4) clay content (Tosaya and Nur 1982; Han 1986; Marion et al. 1992); and 5) grain size (Hamilton 1956; Beard and Weyl 1973). Velocity changes when elastic waves encounter a distinguished boundary inside the medium and therefore it is one of the best means of detecting the inner structure for a geo- or engineered structure (Mueller 1991).

Applying anisotropic stress ($X \neq Y \neq Z$) also causes velocity anisotropy by inducing random cracks (Nur and Simmons 1969), dilatancy of pre-existing micro-cracks (Crampin 1991), or anisotropic stiffening of compliant grain contacts (Sayers 2002; Lockner and Stanchits 2002; Gurevich et al. 2011). Stress-induced anisotropy can affect granular media in two ways: 1) A change in fabric anisotropy in the contact network, and 2) development of an anisotropy force chain network (Cambou et al. 2004; Majmudar and Behringer 2005; Gavin 2015). Generalized Hooke's law states that for general anisotropic elastic linear media the stress (σ_{ij}) is proportional linear to strain (ϵ_{ij}) by elastic stiffness tensor (C_{ijkl}). The elastic stiffness tensor has 81 components; however, not all of them are independent. The symmetry of stress and strain dictates that $C_{ijkl} = C_{jikl} = C_{ijlk} = C_{jilk}$. This reduces the number of independent components to 36. Moreover, due to the energy potential of the strain this number is reduced to 21 ($C_{ijkl} = C_{klij}$). These 21 components are quite important in representing the full anisotropic medium; however, in reality knowing all 21 is quite challenging. Therefore symmetry assumptions are necessary in order to further simplify this matrix. These symmetry assumptions come in different classes. Each of the classes has its own individual matrix pattern of non-zero and independent values. Where two non-zero components, indicates isotropic medium and adding to this number adds anisotropy until we reach 21 components (the most complex anisotropic medium) (Musgrave 1970).

The first class of anisotropy is the simplest, with only five independent components (Nye 1985). This class is called transverse isotropy (TI), and is divided into two groups based on the orientation of the symmetry axis: Vertical Transverse Isotropic (VTI) and Horizontal Transverse Isotropic (HTI). Most geological scenarios can be fitted into TI models (Gavin 2015) due to the nature of the deposition and framework mineral fabric

of the layers. Azimuthal anisotropy is a general TI model that defines a change of velocities in the horizontal plane by use of travel-time or amplitude (Byun et al. 1989; Lynn et al. 1995). This anisotropy can be measured by: i) P-wave velocity, which changes due to a transmitter–receiver azimuth change and ii) vertical propagating shear wave splitting into S-fast and S-slow (Gavin 2015). The formula and detailed description of weak anisotropy (TI) that is the subject of this experimental study is in Chapter 4 of the thesis and can be also found in Mavko et al. (1995).

In the past, anisotropy of any classes was treated as an undesirable and ignored factor due to the complications it causes (Helbig and Thomsen 2005). However, this factor is quite important for modelling and processing seismic data and, for that reason, Thomsen (1986) introduced the dimensionless anisotropic parameters γ , ϵ and δ for weakly anisotropic media (TI). The ϵ parameter defines the P-wave anisotropy, γ defines the S-wave anisotropy or splitting, and δ describes the near vertical phase velocity. These parameters were later modified by Tsvankin (1997) and Ruger (1997) to account for the vertical axis. By calculating the anisotropy parameters and incorporating them into classic operators, 3D seismic processing flows improved (Gavin 2015).

It is not easy to parameterise the anisotropy via real data, and most of the time these parameters should be predicted by rock physical models. Since we are dealing with geo-material, developing a rock physical model is quite challenging. Unlike engineered material, rocks forms have a unique distribution of pores, micro-fractures, crystals and grains. In other words, the composition and arrangement of such elements control the velocity and amplitude of P- and S-waves. This unique signature of the rocks cannot easily be predicted by theoretical models. Yet a good number of empirical relationships and rock physical models proposed to predict the elastic moduli of a medium subjected to stress (Eberhart-Philips et al. 1989; Zimmerman et al. 1999; Saul et al. 2013). While subjected to stress, the medium's discontinuities – including pre-existing micro-cracks and grain boundaries – will close in the direction of maximum stress (Nur and Simmons 1969). This closure stiffens the rock in the direction of applied stress and, at the same time, creates stress anisotropy due to this secondary non-uniformity change (Tocher 1957). To be more realistic, rock physical models had

to consider some shapes for the pre-existing fractures and discontinuities. Some chose penny-shaped cracks (Nur 1971; Sayers 1988), some considered no specific shape for these discontinuities (Mavko et al. 1995; Sayers 2002), and some assumed a spherical contact between the grains for their models (Johnson et al. 1998; Gallop 2013). Rock physical models at the current stage can be assumed to be approximations of reality because they are designed for limited geometries and limited stress ranges, which in reality covers only a small, ideal group of rocks and conditions. These models are not yet entirely valid for predicting anisotropy for deeper ranges (higher and more complex stresses) or covering different lithologies (full length of boreholes for example) (Gavin and Lumley 2016). Every small change in the recording conditions has an effect on controlling parameters, and the end results will be affected. Models can be significantly improved via more complex and detailed laboratory data, where the conditions can be well controlled and repeated. With the advancement of technologies and equipment, it is possible to create more complex scenarios. To achieve more flexible and complex models to predict the real behaviour of the rocks we need more complex and flexible laboratory test designs. To provide accurate and reliable data to calibrate more accurate rock physical models we need to break each experiment into its own components and into its own by-products, such as strain amplitude inside the waves.

1.2.3 Strain amplitude

The dependency of elastic wave velocity on wave amplitude has been studied for many years without knowing the exact mechanism of the phenomenon (Winkler & Nur 1979; Johnson et al. 1996; Ten Cate & Shankland 1996; Zinszner et al. 1997). Studies by Winkler et al. (1979) and Johnston and Toksoz (1980) on sandstone wave attenuation and velocity showed that compressional wave (P-wave) velocity decreases with strain amplitude increase over $\epsilon > 10^{-6}$. Stewart et al. (1983) reported that this change in velocity is insignificant for a number of sandstones under confining pressure (below 50 MPa). Tutuncu et al.'s (Tutuncu et al. 1998) studies of P-wave velocity measured using a longitudinal resonant method on sedimentary rocks concluded that the dynamic Young's modulus decreases with increasing strain amplitude in a number of sandstones. The results of the studies mentioned above show a decrease in wave

velocity with increase of strain amplitude (Johnson et al. 1996; Ten Cate & Shankland 1996, Zinszner et al. 1997); however, a study by Cook and Hodgson (1965) on sandstone deformation shows that the static modulus rises with increasing strain on the stress–strain curves.

The assumption of both increasing and decreasing of the velocity due to increasing the amplitude made earlier by Mashinskii (1994, 2003). In his studies, the influence of microplasticity on the modulus–stress relation was established. This was achieved via the direct and separate measurement of both the elastic and microplastic components of the total deformation in the quasi-static load–unload regime.

The theoretical work by McCall and Guyer (1994) claimed that the dynamic modulus (and thus the wave velocity) increases with stress if there is a positive curvature in the static stress–strain relationship. In a later study (Mashinskii 2001), a multilevel character of the stress–strain relations (an increase, a decrease or a constant behaviour) was demonstrated by the strain as a result of the proposed microplasticity effects. This study showed that the increase in wave velocity caused by increasing the amplitude happens on the positive curvature of dynamic stress–strain curve (Mashinskii 2004).

The amplitude dependence of the wave velocity was measured on a monocrystal of natural quartz for confining pressure less than 10 MPa (Mashinskii 2008). The results showed that the P-wave velocity generated by 1 MHz P-transducer decreased with increasing wave amplitude, while the S-wave velocity increased by 0.5%. An earlier study using field measurements of 500Hz reported an increase in the P-wave velocity with increasing amplitude (Mashinskii 1999). Both studies show open hysteresis behaviour of velocities in the strain range of 10^{-7} – 10^{-6} (Mashinskii 2004).

In theoretical studies, a direct dependence between P-wave velocity and attenuation on strain amplitude has been reported: as the attenuation increases the velocity decreases (Mavko 1979; Stewart et al. 1983). It has to be taken into account that most of the theoretical calculations are based on negative curvature stress–strain diagrams (Van Den Abeele et al. 1997). McCall and Guyer's (1994) theoretical study introduced a model combining the possibility of both decreasing and increasing the quasistatic

and dynamic moduli by increasing the strain. The study obtained both negative and positive curvature, representative of a decrease and increase in elastic modulus respectively. The data in the literature regarding amplitude dependence on wave velocities mainly focuses on attenuation and the wave velocity estimations based on attenuation. A lack of direct measurement of wave amplitude in dynamic experiments lends uncertainty to previous experimental studies and may lead to incorrect interpretation of the results. Thus, to evaluate the effect of velocity dependency on wave amplitude (or strain inside the wave) we designed a special experimental set-up (described in chapter three) to link the velocity of wave propagation with the strain inside the wave.

1.3 Approach and chapter descriptions

This dissertation consists of six chapters. All the chapters are related to the main objective of the study on the experimental investigation of the effect of stress magnitude and stress rate on elastic properties in a group of reservoir rocks. We designed and conducted laboratory experiments on a group of sandstones across Western Australia and the central United States.

Chapter Two presents the experimental study on simultaneous static and dynamic elastic modulus and the relations between the two measured moduli. The experiments designed in this chapter are documented in detail: experiments are performed for uniaxial and hydrostatic conditions to measure Young's modulus and Bulk modulus separately by two static and dynamic approaches. The empirical equations in the literature are then applied to predict the static values from the dynamic, and the results compared. Our results suggest that measured S-wave first arrival gives a more accurate prediction of the dynamic moduli compared with estimating S-wave first arrival from P-wave velocity. We also show that, as an alternative to expensive unconfined compressive strength (UCS) tests, a UCS value estimated by P-wave velocity possesses acceptable accuracy. If calculated based on direct measurement, the velocity of propagating waves provides invaluable information that can replace destructive tests and resolve the geometry limitations if conducted correctly. The Bulk's modulus study in chapter two has been submitted to *Applied Geophysics* (Nourifard and Lebedev 2020).

Chapter Three aims to investigate one of the main reasons for the difference between static and dynamic elastic moduli: strain amplitude. In this chapter we directly measured the strain inside the ultrasonic wave using Laser Doppler interferometry (LDI). With this technique we could measure the effect of strain inside the waves on their velocities. Our results show a new pattern for P-wave velocity compared with previous studies; however, the experimental results for S-wave velocity are in agreement with past studies, where a reduction in velocity was expected from an increase in the strain inside the wave. The extended version of part one of Chapter Three has been published in *Geophysical Prospecting* (Nourifard and Lebedev 2018) and the full text of the second part has been published in *Exploration Geophysics* (Nourifard, Mashinskii and Lebedev 2019).

Chapter Four describes a typical experimental study to estimate the stress-induced anisotropy in a typical weak, anisotropic reservoir sandstone from Western Australia. Three directions of the sample were subjected to hydrostatic stress in dry and saturated forms, and anisotropy parameters were calculated to show the effect of stress and fluid on the degree of anisotropy. The results of this chapter show full saturation and full closure of the pores in an isotropic stress regime decrease the degree of anisotropy as expected. This experimental study controlled for undisturbed initial direction. The process of saturation was conducted inside the pressure cell while wave propagation was monitored. This technique eliminated any deviation from the initial direction and that helped to check the effect of each controlling parameter in isolation (the effects of saturation and increasing stress). The key findings of this chapter has been accepted for publication in *Exploration Geophysics* (Nourifard, Pervukhinab, Urosevica and Lebedev 2019).

Chapter Five considers the local velocity versus averaging velocity recorded by the bigger receiver. In this chapter we designed an experiment on regular geometry of sandstone at ambient conditions to investigate the effect of poles of the source transducer and the impact and displacement this causes at different locations on the surface of the sample. We used LDI as the smallest possible receiver to pick the points and compare the averaging with the recorded wavelet by standard procedures. We mapped the displacement on the surface of the sample caused by the S-wave source transducer. The results of this chapter indicate that LDI is capable of recording

accurate local first arrivals for both P- and S-waves. This chapter confirms the potential of LDI to detect localised micro-structures inside the sample. The experimental results of this chapter has been submitted in *Geophysical Prospecting* (Nourifard and Lebedev 2020).

In Chapter Six we summarised the major conclusions of all the chapters. This includes recommendations for future research and contribution to knowledge.

1.4 References to Chapter One

Avseth, P., Flesche, H. & Wijngaarden, V. A. 2003. AVO classification of lithology and pore fluids constrained by rock physics depth trends: *The Leading Edge*, 22, 1004–1011, doi: 10.1190/1.1623641.

Avseth, P., Mukerji, T. & Mavko, G. 2005. *Quantitative seismic interpretation: Applying rock physics tools to reduce interpretation risk*: Cambridge University Press.

Beard, D.C. & Weyl, P.K. 1973. Influence of texture on porosity and permeability of unconsolidated sand. *AAPG Bull.*, 57: 349-369.

Byun, B. S., Corrigan, D. & Gaiser, J. 1989. Anisotropic velocity analysis for lithology discrimination: *Geophysics*, 54, 1564–1574, doi: 10.1190/1.1442624.

Cambou, B., Dubujet, P. & Nouquier-Lehon, C. 2004. Anisotropy in granular materials at different scales: *Mechanics of Materials*, 36, 1185–1194, doi: 10.1016/j.mechmat.2002.12.002.

Crampin, S. 1991. Wave propagation through fluid-filled inclusions of various shapes: Interpretation of extensive-dilancy anisotropy: *Geophysics Journal International*, 103, 611–623.

Dvorkin, J. & Nur, A. 1996. Elasticity of high-porosity sandstones: theory for two North Sea datasets: *Geophysics*, in press.

Eberhart-Phillips, D., Han, D. H. & Zoback, M. D. 1989. Empirical relationships among seismic velocity, effective pressure, porosity and clay content in sandstone: *Geophysics*, 54, 82–89.

Gallop, J. 2013. Extended Walton third-order elastic coefficients modified by an anisotropic and stress-dependent coordination number: *Geophysics*, 78, no. 6, D545–D556, doi: 10.1190/geo2013-0127.1.

- Gavin, L. 2015. Stress-induced seismic azimuthal anisotropy offshore NW Australia, Doctor of Philosophy thesis, The University of Western Australia.
- Gavin, L. & Lumley, D. 2016. Stress-induced seismic azimuthal anisotropy in the upper crust across the North West Shelf, Australia: *Journal of Geophysical Research: Solid Earth*, 121, 1023–1039, doi: 10.1002/2015JB012568.
- Gik, L.D. 1997. Physical modelling for travel of seismic waves in porous and fractured media, *Geologiya i Geofizika (Russian Geology and Geophysics)*, 38, 4, 804–815(848–858), 1997.
- Gik, L.D. 2000. The use of results of physical modelling for diagnosis of East Siberian carbonate reservoirs, *Geologiya i Geofizika (Russian Geology and Geophysics)*, 41, 2, 268–279(269–280), 2000.
- Gurevich, B., Pervukhina, M. & Makarynska, D. 2011. An analytic model for the stress-induced anisotropy of dry rocks: *Geophysics*, 76, no. 3, WA125–WA133, doi: 10.1190/1.3567950.
- Hamilton, E. L. 1956. Low sound velocities in high porosity sediments, *J. Acoust. Soc. Amer.*, 28, 16-19, 1956.
- Han, D. H. 1986. Effects of porosity and clay content on acoustic properties of sandstones and unconsolidated sediments: Ph.D. thesis, Stanford University.
- Helbig, K. & Thomsen, L. 2005. 75–plus years of anisotropy in exploration and reservoir seismics: A historical review of concepts and methods: *Geophysics*, 70, no. 6, 9ND–23ND.
- Howarth, D. F. 1984. “Apparatus to determine static and dynamic elastic moduli”, *Rock Mechanics and Rock Engineering*, 17: 255–264.
- Johnson, D. L., Schwartz, L. M., Elata, D., Berryman, J. G., Hornby, B. & Norris, A. N. 1998. Linear and nonlinear elasticity of granular media: Stress induced anisotropy of a random sphere pack: *Journal of Applied Mechanics*, 65, 380–388, doi: 10.1115/1.2789066.
- Jones, M. 1995. Use of anisotropy in P-wave and S-wave data for fracture characterization in a naturally fractured gas reservoir: *The Leading Edge*, 14, 887–893, doi: 10.1190/1.1437179.

- Lockner, D. A. & Stanchits S. A. 2002. Undrained poroelastic response of sandstones to deviatoric stress change: *Geophysics Journal International*, 107, ETG-13, doi: 10.1029/2001JB001460.
- Majmudar, T. S. & Behringer R. P. 2005. Contact force measurements and stress-induced anisotropy in granular materials: *Nature*, 435, 1079–1082, doi: 10.1038/nature03805.
- Marion, D., Nur, A., Yin, H. & Han, D. 1992. Compressional velocity and porosity in sand-clay mixtures: *Geophysics*, v. 57, p. 554-563.
- Mashinsky, E.I. 2003. Differences between static and dynamic elastic moduli of rocks: Physical causes. *Geologiya i Geofizika*. 953-959, 2003.
- Mavko, G., Mukerji, T. & Godfrey, N. 1995. Predicting stress-induced velocity anisotropy in rocks: *Geophysics*, 60, 1081–1087, doi: 10.1190/1.1443836.
- Mueller, M. C. 1991. Prediction of lateral variability in fracture intensity using multicomponent shear-wave surface seismic as a precursor to horizontal drilling in the Austin Chalk: *Geophysical Journal International*, 107, 409–415, doi: 10.1111/j.1365-246X.1991.tb01402.x.
- Musgrave, M. J. P. 1970. *Crystal acoustics: Introduction to the study of elastic waves and vibrations in crystals*. San Francisco: Holden-Day.
- Nur, A. & Simmons, G. 1969. Stress-induced velocity anisotropy in rock: An experimental study: *Journal of Geophysical Research*, 74, 6667–6674, doi: 10.1029/JB074i027p06667.
- Nur, A. 1971. Effects of stress on velocity anisotropy in rocks with cracks: *Journal of Geophysical Research*, 76, 2022–2034, doi: 10.1029/JB076i008p02022.
- Nye, J.F. 1985. *Physical Properties of Crystals: Their Representation by Tensors and Matrices*. Oxford University Press, Oxford.
- Rabotnov, Yu. N. 1979. *Mechanics of strained solids [in Russian]*, 744 pp., Nauka, Moscow, 1979.
- Rüger, A. 1997. P-wave reflection coefficients for transversely isotropic models with vertical and horizontal axis of symmetry: *Geophysics*, 62, 713–722, doi: 10.1190/1.1444181.

- Saul, M. J. & Lumley D. E. 2013. A new velocity-pressure-compaction model for uncemented sediments: *Geophysical Journal International*, 202, 905–913, doi: 10.1093/gji/ggt005.
- Sayers, C. M. 1988. Stress-induced ultrasonic wave velocity anisotropy in fractured rock: *Ultrasonics*, 26, 311–317, doi: 10.1016/0041-624X (88) 90028-5.
- Sayers, C. M. 2002. Stress-dependent elastic anisotropy of sandstones: *Geophysical Prospecting*, 50, 85–95, doi: 10.1046/j.1365-2478.2002.00289.
- Sheriff, R. E. 2002. *Encyclopedic dictionary of applied geophysics*, 4th ed.: SEG
- Winterstein, D. F. 1990. Velocity anisotropy terminology for geophysicists: *Geophysics*, 55, 1070–1088, doi: 10.1190/1.1442919.
- Thomsen, L. 1986. Weak elastic anisotropy: *Geophysics*, 51, 1954–1966, doi: 10.1190/1.1442051.
- Thomsen, L. 2002. *Understanding seismic anisotropy in exploration and exploitation: SEG/EAGE Distinguished Instructor Series*.
- Tocher, D. 1957. Anisotropy in rocks under simple compression: *Trans. Am. Geophys. Union*, v. 38, p.89.-94.
- Tosaya, C., Nur, A. 1982. Effects of diagenesis and clays on compressional velocities in rocks, *Geoph³/s. Res. Lett.*, 9, 5-8, 1982.
- Tsvankin, I. 1997. Anisotropic parameters and P-wave velocity for orthorhombic media: *Geophysics*, 62, 1292–1309, doi: 10.1190/1.1444231.
- Tutuncu, A.N., Podio, A.L., Gregory, A.R. & Sharma, M.M. 1998. Nonlinear viscoelastic behavior of sedimentary rocks, Part I: Effect of frequency and strain amplitude, *Geophysics*, 63, 184–194, 1998.
- Vovk, A.A. 1971. *Deformation of compressible solids at dynamic loading [in Russian]*, 175 pp., Naukova Dumka, Kiev.
- Wyllie, M.R.J., Gregory, A.R. & Gardner, L.W. 1956. Elastic wave velocities in heterogeneous and porous media: *Geophysics*, 21, 41-70.
- Wyllie, M.R.J., Gregory, A.R. & Gardner, G.H.F. 1958. An experimental investigation of factors affecting elastic wave velocities in porous media: *Geophysics*, 23, 459-493.

Zimmerman, M.E., Zhang, S., Kohlstedt, D.L. & Karato, S. 1999. Melt distribution in mantle rocks deformed in shear. *Geophysical Research Letters* 26: doi: 10.1029/1999GL900259. issn: 0094-8276.

Chapter 2 Static and dynamic moduli of sandstones

2.1 Foreword

Chapter two demonstrates that using the dynamic measurements of a material in evaluating its elastic property is not only reliable but also necessary to monitor the precise behaviour of the material when subjected to stress. It also highlights that to compare static modulus to dynamic modulus we need to conduct simultaneous measurements to avoid any directional deflection, which causes uncertainty in the results. This chapter builds on the hundreds of laboratory measurements of the static and dynamic results for sandstones, which have been recorded at the same time. Chapter two has been submitted in *Applied Geophysics* and is currently under review.

2.2 Abstract

The dynamic and static elastic moduli of a number of isotropic sandstones were measured using ultrasonic measurement of the elastic velocities of P- and S-waves and standard uniaxial and hydrostatic stress tests. We developed and modified an experimental method to simultaneously measure the stress-strain and stress-velocities (P- and S-waves) to calculate the static and dynamic Young's modulus, Bulk modulus and Poisson's ratio. The rate of loading for this experiment was planned to be similar for the static and dynamic measurements. Past studies measured the static modulus and dynamic modulus at different rates (static experiments are usually 60 times faster than dynamic measurements). We made uniform the loading-unloading stress at 1 MPa/minute for all of our uniaxial and hydrostatic experiments. These measurements were conducted at a central dominant frequency of 1 MHz. Dynamic Young's modulus ranges of 4–30 GPa and dynamic Bulk's modulus ranges from 4–13 GPa were recorded for all the tested samples. The static Young's modulus were simultaneously measured and ranged from 4–17 GPa, and static Bulk modulus ranged from 2–11 GPa for the same samples. The static and dynamic results were obtained simultaneously while on the proportional limit of the stress-strain graph. The study determined that the use of the dynamic elastic moduli in an isotropic material provides good correlation to static moduli and adds useful engineering information to the study of the strain pattern and deformation properties of homogeneous reservoir rocks. This study was extended to measure dynamic Young's modulus and Poisson's ratio for four individual

times of the study to investigate the effect of stress and time relaxation on the properties of the sandstones. We measured the elastic properties at ambient state outside of the pressure cell before applying the stress, right after the unloading, 20 days, and 60 days after the experiment. The pattern for all the samples showed an increase of the Young's modulus right after the stress application and the gradual decrease of this value over time; however, most of the samples could not recover to the original state due to the some permanent deformation inside the rock matrix.

The difference between the static and dynamic modulus may be related to the observed dependent strain amplitude, which will be investigated in the next chapter.

2.3 Introduction

To plan, design and build structures, one needs to know the engineering properties of the rock involved (i.e., the foundation base). Rock behaviour plays a major role in the safety and sustainability of the exploration for, and extraction of, natural resources. To understand the properties of intact rocks, site investigation has been the most important part of the majority of engineering projects. It determines the deformational characteristics of the base material involved (McCann and Entwisle 1992). Such evaluations have been conducted in laboratory experiments on intact rock samples for decades. They started with the simplest types of measurement, such as applying uniaxial stress to break the samples to estimate the uniaxial compressive strength (UCS) of the samples, and gradually developed to more complex measurement of the rock behaviour through wave propagation. Such analysis gives more insight to a rock and associated elastic properties for natural and engineered material.

It is not always possible to conduct experiments in the field; therefore, to perform measurements the samples are extracted and sent to laboratories for analysis. The important question is how accurate, reliable and representative the laboratory experiments are in gaining in-situ properties of the rocks (McCann and Entwisle 1992). In-situ stress experiments can enhance the knowledge of the engineering properties of rocks in the field where the original state of stress combination has not been violated (i.e., Plate load and Goodman Jack tests) (Anon 1981; Marsland 1971; Lane 1964; Burland and Lord 1970; Hobbs 1973 and ISRM 1981; Goodman 1980). However, due to the high cost of such experiments it is not always possible for projects to conduct

such field evaluations. Laboratory experiments using well designed and documented approaches will add value to the accuracy of the results. Great examples of such experiments are dynamic and static experiments to determine the elastic modulus of the material.

For engineered material – i.e., steel, aluminium and synthetic material – measurements of P- and S- velocities at ultrasonic frequencies is a long-trusted method for determining the so called “dynamic elastic” moduli. However, for more compliant material, the reliability of this technique has been questioned due to the difference in results with static moduli. Yet dynamic elastic moduli have been used in preference to static moduli in civil engineering in projects where the structures are subjected to dynamic loading effects – i.e., wave action on a marine structure – for their foundation design (McCann and Entwisle 1992).

This uncertainty with respect to the dynamic approach in isotropic and homogenous samples may be caused by natural pores and micro-cracks inside natural rocks – especially sandstones, which have higher pore density. Even rock samples with the lowest degree of anisotropy and a homogeneous mineral framework matrix contain the pores and micro-cracks that lead to different wave behaviour and, therefore, different elastic moduli for the same material. Once subjected to static stress most geological samples do not react in a perfectly linear elastic manner and that is the main reason for the difference between dynamic and static values. The second important difference between the two approaches is the different strain level at which both moduli are measured. It should be noted that strain levels measured in a dynamic test are smaller than strain levels measured in static experiments. In dynamic experiments the strain value is below 10^{-6} while in static experiments this value is greater than 10^{-3} .

The evaluation of dynamic elastic moduli is cost efficient and non-destructive to perform both in the lab and in field. Multiple past studies have tried to formulate the relationship between static and dynamic moduli (Ide 1936; Sutherland 1962, King 1983, Van Heerden 1987, Eissa and Kazi 1988, Christaras et al. 1994, Lacy 1997, Nur and Wang 1999, Horsrud 2001, Martinez et al. 2012, Brotons et al. 2014, Najibi et al. 2015). In a classic study by Lama and Vutukuri (1978) it was mentioned that the dynamic Young’s modulus can be up to 300% higher than the corresponding static

modulus (McCann and Entwisle 1992). In modern studies by various researchers this percentage has been recorded at about 40%. This shows that one of the reasons behind this difference is the technology of extracting the dynamic modulus and, the knowledge of wave propagation and the correct estimation of velocities, which has been enhanced over decades of experimental rock physic studies.

2.3.1 Dynamic elastic moduli

The P- and S-velocities of the elastic body waves propagating through the body of the sample, and the bulk density of the material are related to the deformational characteristics of the sample. The dynamic elastic moduli of a material are formulated as below:

Young's modulus (E_d)

$$E_d = 2\rho V_s^2 (1 + \nu_d) \quad (\text{Eq 2.1})$$

Poisson's ratio (ν_d)

$$\nu_d = (0.5(V_p/V_s)^2 - 1) / (V_p/V_s) - 1 \quad (\text{Eq 2.2})$$

Shear modulus (μ_d)

$$\mu_d = \rho V_s^2 \quad (\text{Eq 2.3})$$

Bulk modulus (K_d)

$$K_d = \rho(V_p^2 - 4/3V_s^2) \quad (\text{Eq 2.4})$$

Where V_p is the compressional wave velocity, V_s is the shear wave velocity and ρ is the bulk density.

In the laboratory V_p and V_s can be measured by the time-of-flight technique, which calculates the time of first arrival for P- and S-waves propagating from the known distance of the sample. It is common procedure to measure P-wave velocity by a P transducer and S-wave velocity by an S transducer; however, some of the S-wave transducers are able to record first arrival of P-waves, although they are designed to register only shear displacement. Picking the first arrival of S-waves is often more difficult and complex than picking the P first arrivals, especially for porous, soft sedimentary rocks under low effective pressure.

One of the complications of past experimental studies in regard to dynamic testing is the registering of S-wave first arrival not being reported in detail. This is a general pattern throughout the literature. Usually in experimental studies the lab data is limited to the measurement of P-wave velocity only; however, the S-wave first arrival will be estimated from different sources by empirical equations. The reasons for not directly measuring the S-wave velocity can be summarized as follows: Laboratory limitations, low transmitted shear wave energy, and the uncertainty of picking the S-wave first break, especially for high-porosity material. Even in the few cases in the literature where the S-wave is directly recorded there remains a lack of information on how the first arrivals of the S-wave were picked. Christensen's equation (Christensen 1985) is one of the suggested methods in the literature to identify the S-wave first arrival where direct measurement is not possible (Eq 2.5 and 2.6). A later study by Entwisle and McCann (1990) reported that for soft sandstones Christensen's equation overestimates the velocity of the S-wave. This overestimation leads to a calculation of a higher value of dynamic elastic modulus than real elastic modulus. Castagna et al. (1985) summarised the data from past experimental studies to determine the relationship between P- and S-wave velocities for soft rocks. This study concluded that V_p/V_s of soft rocks is highly variable, from 1.8 for quartz rich samples to over 5 for water-saturated loose sediments (McCann and Entwisle 1992).

$$V_s = V_p \left((1 - 1.15 \left(\frac{1}{\rho} + \frac{1}{\rho^3} \right) / e^{1/\rho}) \right)^{3/2} \quad (\text{Eq 2.5})$$

$$V_p = 1.16 V_s + 1.36 \quad (\text{Eq 2.6})$$

Most empirical equations for the estimation of S-wave first arrival are based on the V_p/V_s ratio of about 1.5. One issue in estimating the S-wave first arrival – which has caused issues in previous dynamic studies – is the consideration of this ratio. Our experimental data shows that the ratio is not entirely correct for all states of a material. In the following sections we will present the ratio of V_p/V_s for the direct measurement of both P- and S-wave velocities of a number of so-called homogeneous sandstones that do not follow the accepted general pattern.

Dispersion – i.e., frequency dependence of the velocity of wave propagation – is the other important parameter in the computation of accurate velocities. While it was previously believed that the propagation of P- and S-waves in geo-material was

independent of frequency (O'Brien 1953), a later study by Winkler (1986) indicated that frequency-dependent velocities can be observed, which are associated with a high attenuation coefficient (low-Q) in porous samples. Therefore, the dynamic elastic moduli will be affected by frequency and this parameter should be considered in estimations of S-wave velocities.

To eliminate these uncertainties in S-wave velocity determination it is best to directly measure S-wave velocity using a variety of effective pressures. Recording accurate V_p and V_s is crucial and the smallest error in picking introduces significant differences in dynamic elastic moduli. In order to highlight the importance of picking first arrivals for the presented dynamic study, all first-arrival pickings are described in detail and accompanied by full recorded wavelets as well as a couple of techniques to tackle the uncertainty issues of the first arrivals.

An S-wave oscillates in two perpendicular directions (x and y for vertically propagating S-wave), unlike the P-wave, which propagates in only one direction. For S-waves we have considered two orthogonal directions when the S-wave is passing through the material. If a sample is isotropic then the S-wave velocities are independent to direction; however, if a sample possesses even small anisotropy then the propagation of shear wave in some directions is faster than others, depending on the direction of the inside cracks and pores. In such cases we can record two kinds of S-wave: Fast S-wave (S_f or S_1) and slow S-wave (S_s or S_2). This S-wave splitting can be easily observed in the lab by changing the wave propagation while doing the experiment. We call this 'S-wave splitting' to distinguish S-fast and S-slow and as an obvious sign of the anisotropy. To be consistent in all our measurements the original direction of the ultrasonic measurements has been marked on each sample and all further investigations for stress and post-stress ultrasonic experiments conducted for this particular direction. The initial measurement of the S-wave for most of the samples was independent of the direction (a sign of isotropy); however, by introducing stress on the sample (specifically uniaxial stress) we are inducing anisotropy, and having the original reference direction can help to evaluate the change in one direction for the sample through the whole experiment.

2.3.2 Static elastic moduli

To measure the deformation of the samples subjected to stress, strain gauges and/or Linear Variable Differential Transformer (LVDT) are usually implemented. Strain gauges are small sensors attached to the surface of a sample at the middle of the sample length. For elastic, non-porous samples, the stress-strain graph demonstrates pure linear behaviour before entering into the plastic region of the graph (*Figure 2-1 (a)*). By unloading the stress, the graph returns to the original unstressed state with a closed loop. The slope of the linear part of the graph can be calculated by equation 2.7:

$$E_{static} = \delta\sigma / \delta\epsilon \quad (\text{Eq 2.7})$$

Where σ is the deviator stress and ϵ is the change in length with respect to the initial length. Majority of the rock samples behave non-linear even on elastic region of the stress-strain graph and therefore a number of methods have been proposed by International Society of Rock Mechanics standards (ISRM 2007) to pick the correct location of the graph and extract the static Young's modulus (*Figure 2-1(b)*). These methods mainly explain the general procedure for calculating the slope of the line where different slopes are presented on the graph. These methods are summarized below:

(a) Tangent Young's modulus, E_t , is measured at a stress level that is a fixed percentage of the ultimate strength. It is generally taken at a stress equal to 50% of the ultimate uniaxial compressive strength. Figure 2-1 (b) illustrates this method by picking a linear part of 50% of UCS $\pm 15\%$ and getting the tangent of the selected line as the corresponding elastic modulus as $\Delta\sigma/\Delta\epsilon$.

(b) Average Young's modulus, E_{av} , is determined from the average slope of the straighter portion of the stress-strain curve (*Figure 2-1(a)*).

(c) Secant Young's modulus, E_s , is usually measured from zero stress to some fixed percentage of the ultimate strength (generally at 50%). This method has been used for static measurement in this study.

Young's modulus E is presented in stress units and usually expressed in Gigapascal (GPa = 10^9 Pa).

Poisson's ratio, ν , can be calculated from equation 2.8,

$$\nu = -E / (\text{slope of diametric stress-strain curve}) \quad (\text{Eq 2.8})$$

Where the slope of the diametric graph is measured by the same steps as Young's modulus. Poisson's ratio has a positive value because by conventions the diametric curves show negative value.

The volumetric strain, ϵ_v , can be calculated from equation 2.9:

$$\epsilon_v = \epsilon_{\text{axial}} + 2\epsilon_{\text{diametric}} \quad (\text{Eq 2.9})$$

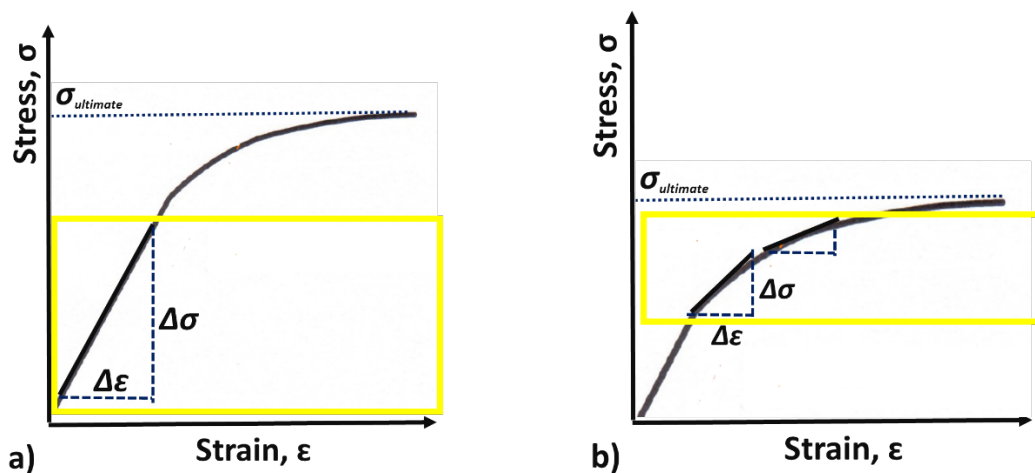


Figure 2-1 Stress-strain curve for the computation of Young's modulus: a) linear value measured from zero stress to a fixed percentage of ultimate strength usually up to 50% and, b) regional linear value at 50%±15% of the ultimate strength (ISRM 2007).

Static Young's modulus experiments can be affected by several factors, such as the rate of strain, the sample's lack of initial alignment, and yielding of the sample at low strains (McCann and Entwisle 1992). The static Young's modulus reduces by the low rate of the strain (Atkinson et al. 1990). According to the ISRM standard the proposed loading rate of the UCS experiment is 0.5-1 MPa/sec (ISRM 2007). Thus, to test the sample by applying 60 MPa loading would take 1–2 minutes. If carrying out a simultaneous dynamic experiment while doing the static tests the mentioned rate is too high and does not allow sufficient time for the operator to monitor the wave propagation and record the corresponding wavelets at a variety of stresses. In this study we took static and dynamic measurements by a loading rate of 1 MPa/min. This rate is 60 times slower than the recommended static uniaxial and hydrostatic tests because of the limitations of the acquisition system used in standard rock physics experiments.

In cyclic measurement (loading and un-loading) of elastic modulus, the effect of stress relaxation should be taken into account (McCann and Entwisle 1992). The relaxation time varies for different materials and some geologic materials may not return to an unstressed state. The loading–unloading loop is usually closed for the tests in the pure elastic region and an open loop for porous natural material. For the porous soft sandstones that have been tested in this experiment, the relaxation time has been considered by measuring the velocities at three different times: right after stress unloading, 20 days, and 60 days after the experiment. Therefore, Young’s modulus (dynamic) has been recalculated at four different points in the experiment and the results compared to study this important factor.

2.3.3 Dynamic and static experiments to determine elastic Young’s and Bulk moduli

The dynamic moduli of rocks are those calculated from the bulk density and elastic wave velocities. The static moduli are those directly measured in a deformational experiment. The static and dynamic moduli of the same rock may significantly differ from one another. The main reason for this is likely to be the difference in the deformation (strain) amplitude between the dynamic and static experiments. In the dynamic wave propagation experiment the strain is about 10^{-7} while static strain may reach 10^{-2} .

2.4 Sample preparation

The core plugs of 15 homogeneous isotropic sandstone samples from seven groups of sandstones with a diameter of 38 ± 0.4 mm and different lengths of 56-75 mm were trimmed and prepared for static and dynamic study (*Figure 2-2*). It should be noted that all the groups are different forms of the Berea sandstone family. The specifications of each sample are listed in *Table 2-1*. This table contains the P and S ultrasonic velocities, and densities measured at ambient condition right before the stress tests. The average porosity and unconfined compressive strength (UCS) values have been reported from the mine site. The porosity and UCS of a couple of the samples have also been tested inside the lab as a control check of the values. A thin layer of epoxy resin was applied on a small portion of each sample at the middle points to create a smooth base for the LVDT strain-gauge attachment. Strain gauges were glued on to the smooth centre

points and wires were attached for the static measurements (*Figure 2-3*). For the calibration and initial tests to check the accuracy of the results for simultaneous dynamic and static elastic modulus, Polymethylmethacrylate (PMMA) samples were chosen to demonstrate pure elastic behaviour. PMMA samples were cut and prepared, and strain gauges attached on the centre points using the same approach to the sandstone samples.

	<i>Samples (sandstones and PMMA)</i>	<i>Length (mm)</i>	<i>Density (gr/cm³)</i>	<i>Average porosity %</i>	<i>UCS (MPa)</i>	<i>Initial Vp by P transducer (m/s)</i>	<i>Initial Vp by S transducer (m/s)</i>	<i>Initial Vs by S transducer (m/s)</i>
<i>11</i>	Bandara gray	59.78	2.3	21	34.5	3236	3165	2137
<i>12</i>	Bandara gray	63.46	2.1	21	34.5	3319	3294	2167
<i>13</i>	Bandara gray	63.38	2.0	21	34.5	3045	3034	2009
<i>21</i>	Castlegate	65.74	1.9	26	13.8	2023	2025	1356
<i>22</i>	Castlegate	69.72	1.9	26	13.8	2291	2278	1526
<i>31</i>	Upper gray	69.73	2.2	18	41-55	2556	2545	1674
<i>32</i>	Upper gray	66.12	2.1	18	41-55	2690	2673	1787
<i>41</i>	Berea	63.49	1.7	28	45-55	3317	3614	2386
<i>42</i>	Berea	36.89	1.8	28	45-55	3062	3123	2072
<i>43</i>	Berea	63.44	1.8	28	45-55	3070	3115	2094
<i>44</i>	Berea	63.39	1.9	28	45-55	3060	3018	1998
<i>51</i>	Sister gray	69.71	2.1	21	48.3	2771	2802	1903
<i>52</i>	Sister gray	65.85	2.2	21	48.3	2592	2531	1694
	Donny	63.88	2.3			3010	2944	1951
	Brook			15				
	Bentheimer	74.52	2.0	24	26- 27.6	2677	2652	1381
	PMMA	55.91	1.2	-	60-90	2619	2618	1762

Table 2-1 Properties of the tested samples in this study (UCS values for the Berea family have been extracted from kiptonquarry.com)

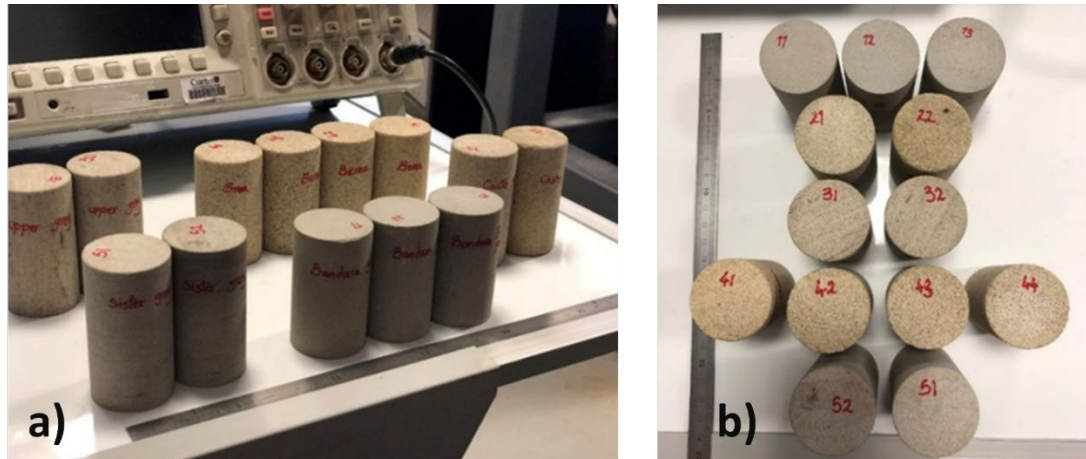


Figure 2-2 a) side and b) top view of sandstone core-plugs of Berea, Upper gray, Sister gray, Bandera gray and Castle gate after cut and before installation of the strain gauges.



Figure 2-3 Core-plugs of Bentheimer sandstones drilled from quarried block and prepared by installation of strain gauges on the layer of epoxy resin at the centre point.

2.5 Experimental set up

This section outlines the combination of static and dynamic equipment required for simultaneous measurements of both static and dynamic Young's and Bulk moduli. The ultrasonic set-up measures the wave propagation while the stress cell applies pressure on the top and bottom plates and/or through the Hook's cell (uniaxial or hydrostatic). This technique enables us to test the same sample on the same cycle of pressure. In each sample group, uniaxial and hydrostatic experiments were performed to obtain Young's modulus and Bulk modulus. The set-up for all experiments contained the standard ultrasonic equipment for the dynamic part of the study and conventional static equipment to determine static deformation of the rocks (*Figure 2-4*).

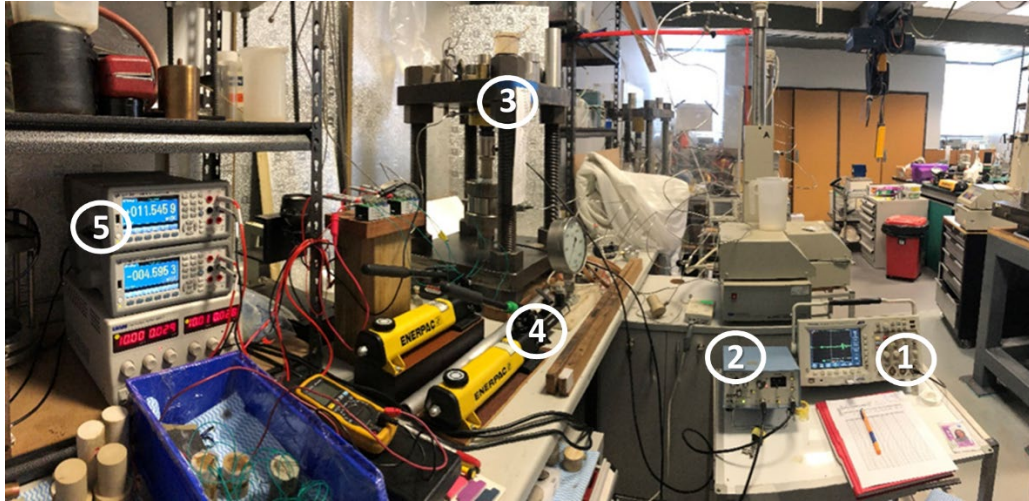


Figure 2-4 The dynamic and static set-up consists of: 1) oscilloscope, 2) pulser, 3) stress frame, 4) pumps, and 5) voltmeter set attached to strain gauges on the samples.

2.5.1 Ultrasonic equipment

The ultrasonic equipment for the experiment included a pair of 1 MHz, videoscanner-type S-wave transducers V153 (Olympus Ltd). A pulser/receiver 5077PR (Olympus Ltd) electronic block and a digital, 300 MHz 2.5 GS/s, 4-channel oscilloscope TDS3034C (Tektronix Ltd) were used to apply and record electrical signals. A square electrical pulse of 1 μ s in duration with the amplitude voltage of 400 was applied to the source transducer. This creates a mechanical pulse at the sample's boundary and generates an ultrasonic elastic wave that propagates inside the sample. The S-wave transducers were moulded inside the steel actuator in the direction of axial stress. The first round of dynamic measurements was performed right after the sample preparations outside of the cell to record the initial velocities of P- and S-waves by both types of transducer. These velocities were registered as the pre-stress velocities, to be compared with the post stress velocities at the end of the experiment to allow 'before' and 'after' comparison for stress relaxation analysis.

2.5.2 Initial measurement of the sample before installation of the stress cell

The velocity of the P- and S-waves of all samples was measured by P and S transducers separately. The test was carried out by ultrasonic equipment at zero stress. The steps in the initial tests is illustrated in *Figure 2-5*. This data enables us to check the effect of pressure on the post-stress behaviour of each sample. Since the samples were chosen from homogeneous and so-called 'isotropic' sandstones, the directional elastic wave properties were assumed to be the same. However, by changing the S-wave

polarisation by 90 degrees, a couple of samples showed less than 0.5% change in S-wave velocity. Therefore, the initial measurement direction of the samples was fixed and marked for the rest of the experiments for the uniformity and elimination of directional effect as a result of small possible anisotropy. The ratio of V_p/V_s was found to have a good agreement with the literature as having the value of 1.5 for dry sandstones. The Poisson's ratio and initial dynamic Young's modulus of the samples were then calculated.

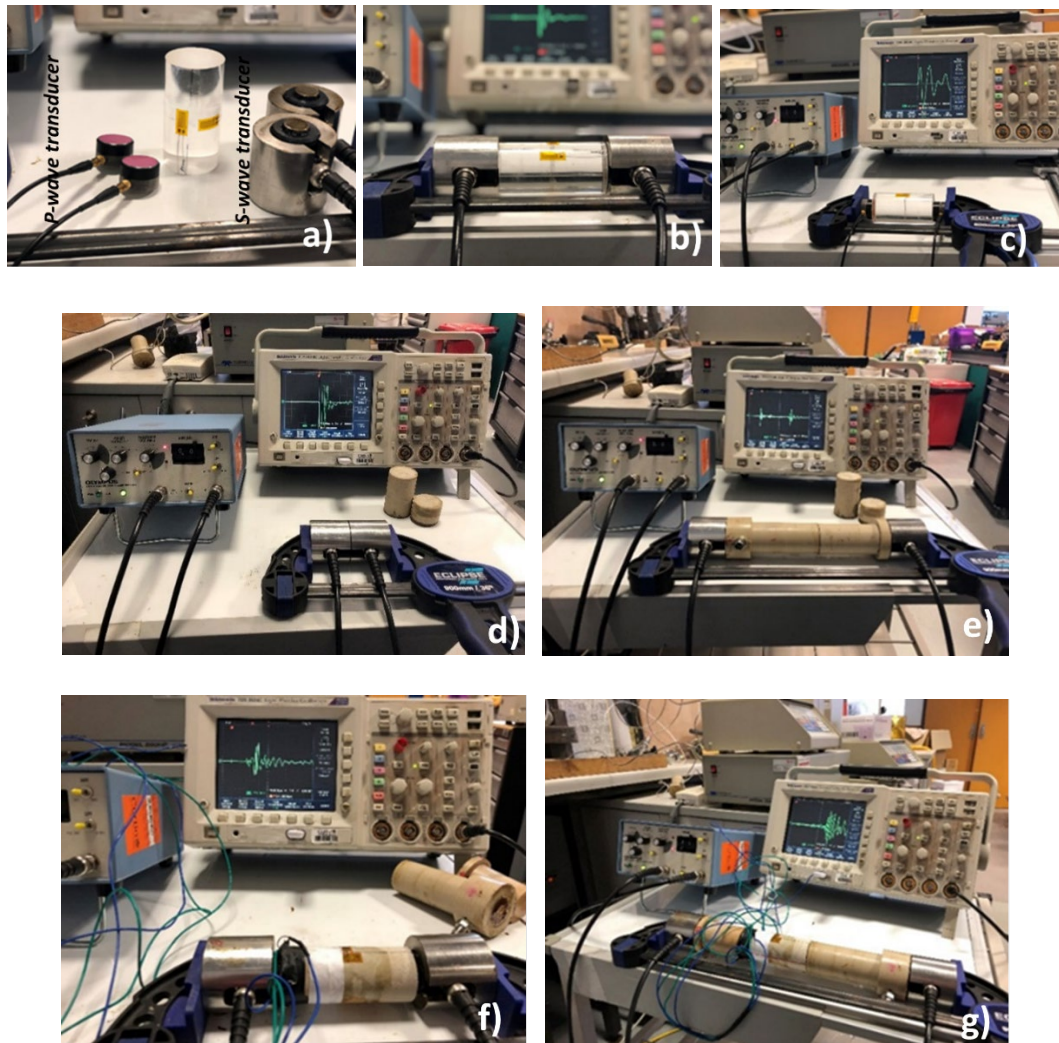


Figure 2-5 Initial set-up to measure P and S velocities out of the stress cell with two types of 1 MHz transducers: P transducer and S transducer (a). The primary experiments to measure velocities outside of the pressure cell consists of : (d) measurement of the deadtime (electronics time delay) by measuring direct contact of transducers surface, (e) ultrasonic measurement of the PEEK parts with a length of 200.04 mm (top and bottom plates of PEEK); (f and b) samples have been tested by S-wave transducer, (c) samples have been tested by P-wave transducer and (g) samples have been tested by S-wave transducer while in contact of top and bottom plates of the PEEK.

2.5.3 Uniaxial and hydrostatic (Hook's cell) set-ups

The elastic property of the material can be determined if two moduli are known (either Young's modulus, Shear modulus, Bulk modulus, or Poisson's ratio). Most engineered materials exhibit nearly incompressible behaviour with a Poisson's ratio close to 0.3; however, for natural porous material (sandstones) the ratio is usually between 0.1–0.3. In rare cases of very soft rocks, particle suspension or water-saturated sediment under no pressure (ie pelagic ooze) the Poisson's ratio approaches 0.5 (Mavko et al. 2009). The elastic Young's modulus and Poisson's ratio of the samples were measured by uniaxial tests and the Bulk modulus computed by hydrostatic tests. Knowing the Bulk modulus is important when large hydrostatic stresses are present (e.g., high-pressure seals, deep sea exploration, etc) but most importantly this modulus is the best representative of in-situ conditions for rocks where they experience not only axial stress but circumferential stress at the same time. We conducted volumetric compression (Bulk modulus) laboratory experiments by compressing a cylindrical specimen inside the Hook's cell. This set-up prevents free radial expansion of the specimen (as occurs in a uniaxial compression test). The set-up enables us to measure both static and dynamic properties simultaneously while applying hydrostatic pressure. Analysis of the applied load and resulting strains produces a measure of the specimen's Bulk modulus. The set-up determines the Bulk modulus as a function of hydrostatic loading.

The mechanical parts of the uniaxial stress cell consist of a pressure frame of 200 kN capacity, an axial actuator, one pair of moulded S-wave transducers, Polyether ether ketone (PEEK) top and bottom plates and digital multimeters to record strain gauge variation of the resistivity. The hydrostatic set-up consists of the same uniaxial set-up for application of axial stress, and for hydrostatic stress a Hook's cell was used. The sample was placed inside the Hook's cell membrane and fine wires, durable in high pressure, were designed to exit safely from the cell. *Figure 2-6*, *Figure 2-7* and *Figure 2-8* illustrate the schematic and laboratory configuration of both set-ups.

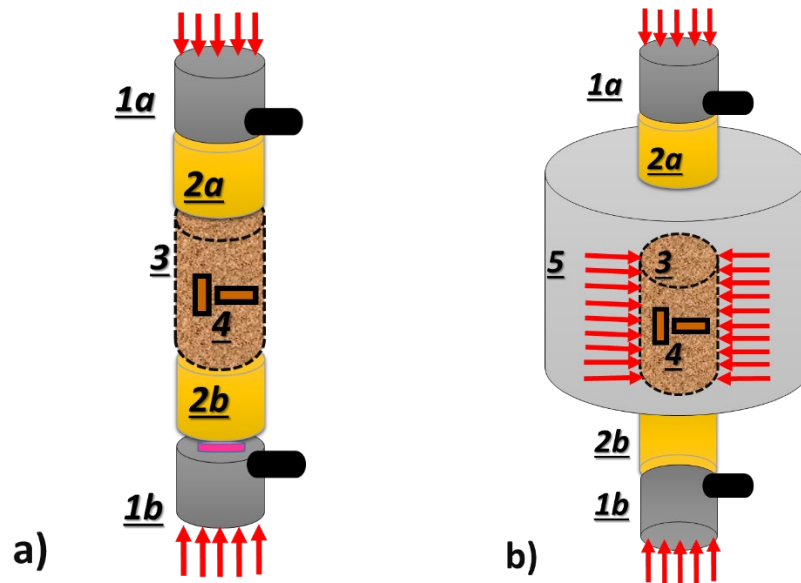


Figure 2-6 Schematic demonstration of the uniaxial (a) and hydrostatic (b) pressure cell used in this study consists of the following parts: 1) S-wave transducer moulded inside the steel actuator for axial pressure axis, 2) PEEK top and bottom plates for best noise cancellation of wave propagation, 3) core-plunge, 4) strain gauges attached on the surface of the sample, 5) Hook's cell for applying hydrostatic pressure (the membrane inside the cell enables the access through of the high-pressure-resistant wires attached to strain gauges on the surface of the sample).

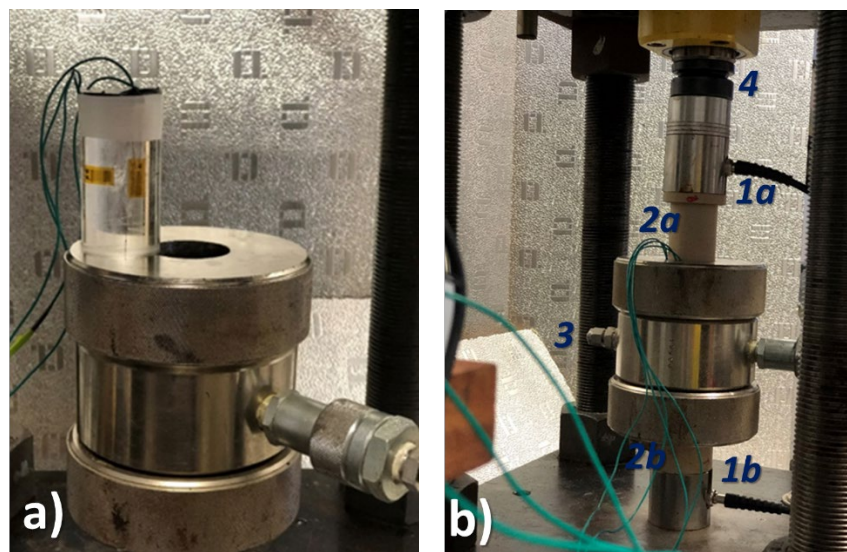


Figure 2-7 (a) Sample before putting into the Hook's cell, (b) Set-up during the experiment. Hook's cell parts consists of: 1) S-wave moulded transducer inside the steel actuators, 2) PEEK plates and parts for the top and bottom of the sample, and 3) Hook's pressure cell to apply hydrostatic stress by pressurized oil on the back of the membrane.

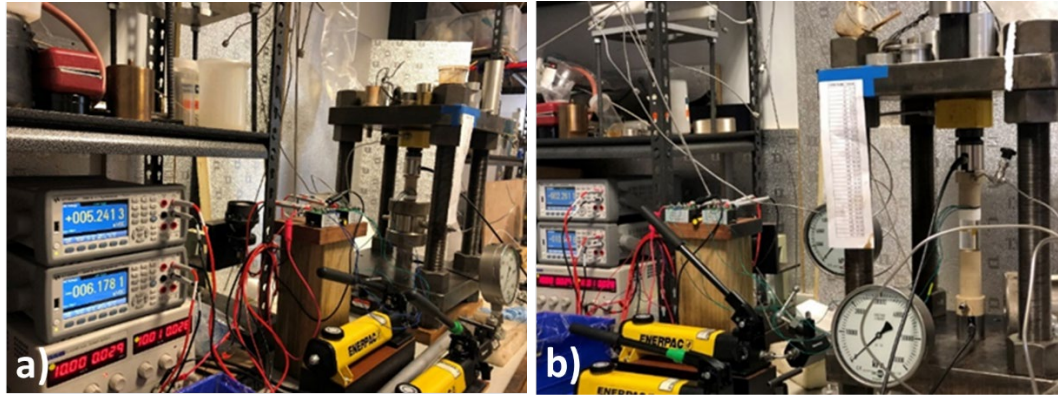


Figure 2-8 Hydrostatic and uniaxial experimental set-ups: (a) Hook's cell set-up for hydrostatic experiment and (b) set-up for uniaxial experiment with pressure applied on the Z-axis (all other elements of the set-up are described in Figures 6 and 7).

2.6 Method and data

The experiment was performed by using the method proposed by the ISRM to obtain the elastic Young's modulus. However, as mentioned earlier our rate of applying stress was chosen as 1 MPa/min. Diametric and axial strain values were recorded for each loading set to the maximum value of 50% of the sample's ultimate strength. Unconfined Compressive Strength (UCS) values were obtained from the mine site and are summarised in *Table 1-1*. These UCS values have been confirmed in some of our experiments when a sample experienced failure. Samples went through a process of preparation that included smoothing their top and bottom faces and drying them in the vacuum oven at 70 C (before conducting the experiment) at least 24 hrs. Initial velocities of P- and S-waves were measured and S-wave polarisation of the transducer was marked on the sample as a reference direction. Strain gauges were attached on a thin layer of epoxy on the sample's centre line at the vertical and horizontal axes. Wires were then attached to each strain gauge. All the samples were tested inside the stress cell and simultaneous measurement of the stress-strain and stress-velocities (full wavelets) relations were recorded and plotted for further processing.

2.6.1 Dynamic and static approaches to determining of the elastic moduli

The dynamic modulus can be determined if the bulk density and the velocities of P-waves and S-waves are known (Eq. 1 and 4). Bulk density can easily be measured; however, the problem arises in accurately detecting the first break of the S-waves,

especially at low pressure. The first breaks of both P- and S-waves become clearer by applying pressure, and once we reach the highest pressure sequence both breaks have enough accuracy to name that wavelet a reference wave. As we mentioned, at low pressure the wavelets are usually weak and the detection of the first break becomes challenging. To overcome such uncertainty, we used the technique of picking peaks to restore the first arrivals. We registered each wavelet at each stress sequence of the loading–unloading cycle (*Figure 2-9*) and then took the waveform at the highest applied stress as the reference wave. It should be noted here that for each cycle of loading–unloading one reference wave has been selected, and for two cycles of loading–unloading – which are presented in *Figure 2-9* – we have two reference wavelets. The reference wavelet was analysed for not only its first breaks but for a minimum of two positive and negative peaks with the shortest distance to the first breaks. For the reference wavelet the first arrivals for P and S-waves marked and the selected peaks should also be marked as reference times for highest stress. The selected peaks should have enough energy in all wavelets to be distinguished even at lowest stress. The time difference between first arrival and each of the peaks was then calculated and remained as our reference time, and then for the rest of the wavelets we only relied on the time of the peaks and doing the corrections for first arrivals according to the reference wavelet. This technique is illustrated in *Figure 2-10*, where the major feature of the reference wavelet will be used in detecting the first breaks at lower pressures.

For our dynamic measurement the PEEK top and bottom plates are quite important; however, to eliminate their effect on first arrivals (time delay) and investigate their elastic behaviour once subjected to stress, the first round of calibration tests was carried out on testing PEEKs solely. The deadtime of the S-wave transducers was measured and then PEEKs' parts installed in the uniaxial set up (*Figure 2-11*). Initial measurements of stress-strain were then plotted. The equation of the line for both P- and S-wave first arrivals at varying stress was measured and this equation was used for the correction of first arrivals once the sample was inserted in between the PEEK plates. The PEEK solo experiment results and equation of the line are presented in *Figure 2-12* and *Figure 2-13*.

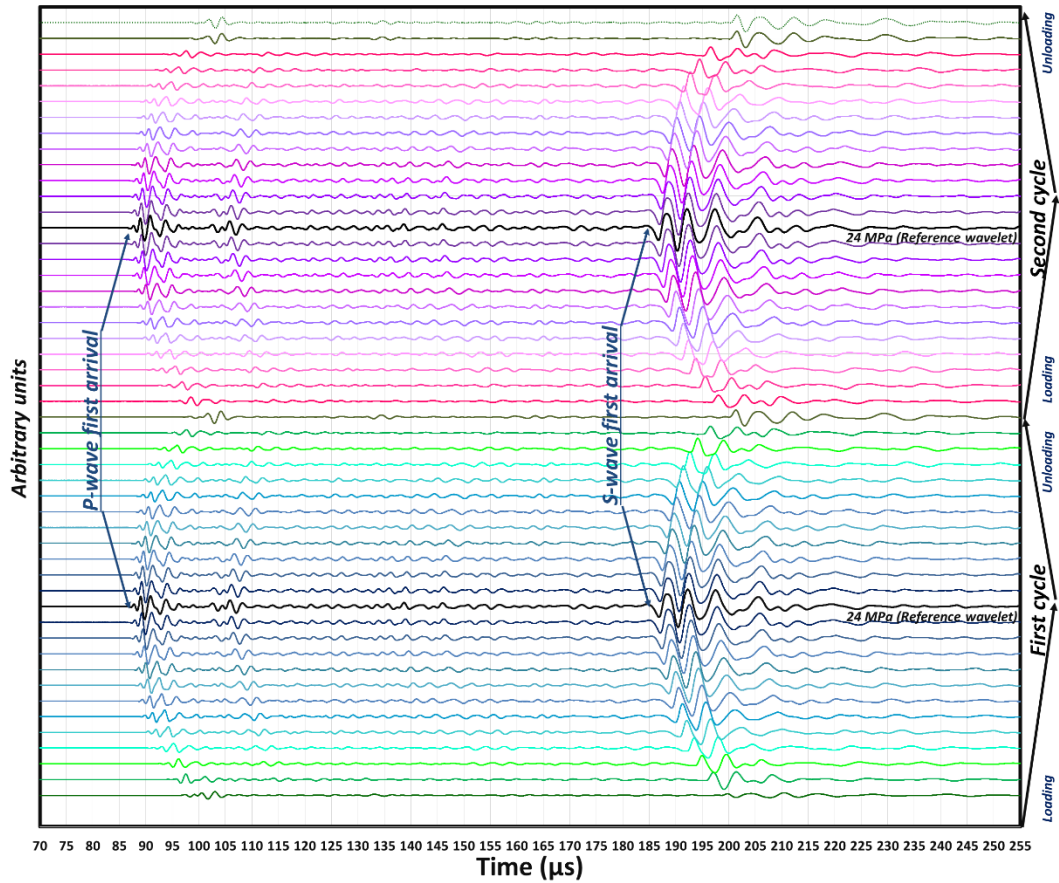


Figure 2-9 Wavelets of sample 31 (Upper gray) showing two cycles of a hydrostatic experiment (up to 24 MPa loading–unloading). The black wavelet in the middle of each cycle represents the reference wavelet at the highest applied stress. The first arrivals of P- and S-waves are marked on the graphs for the reference wavelets.

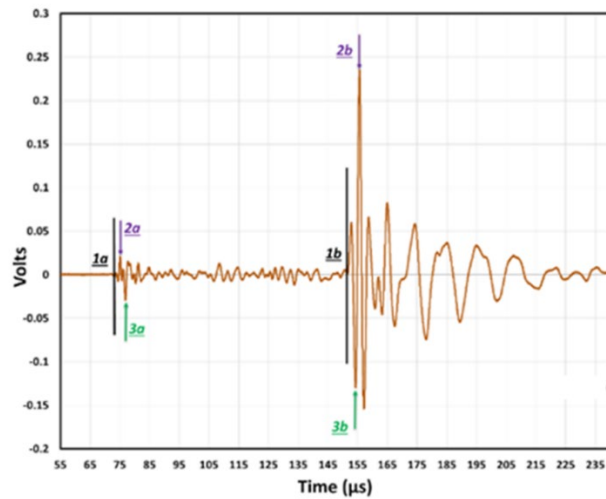


Figure 2-10 (Reference wave) first arrivals picking technique used for all the experiments in this chapter. 1a and 1b are the registered first arrivals for the best sharp wavelet (usually at the highest load cycle), 2a and 2b are the best peak that is obvious and sharp enough to be detected on all wavelets at all pressures, and 3a and 3b are the second-best observable features for confirmation of first feature.

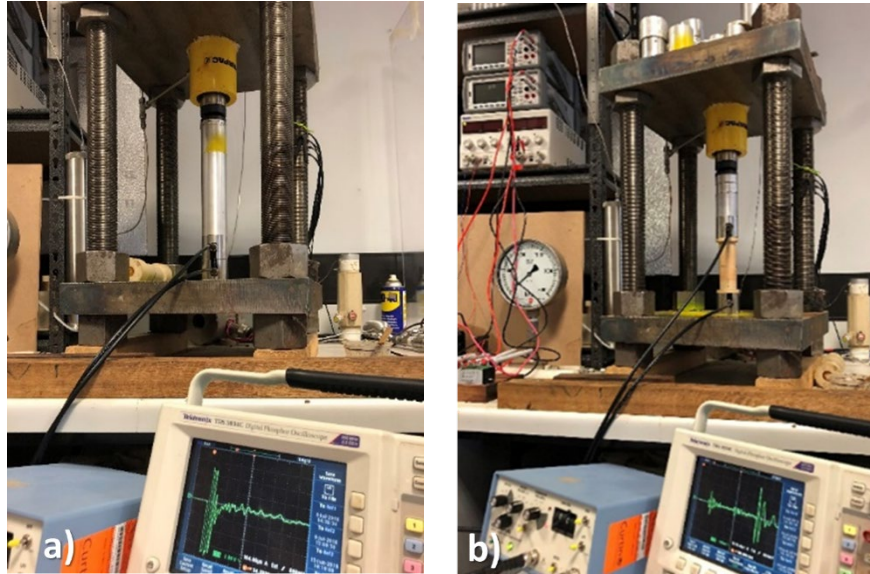


Figure 2-11 Calibration experiment (a) deadtime measurement for S-wave transducers in direct contact with one another, and (2) PEEK plates and S-wave transducers in the stress frame to get the PEEK equation of the line for the correction of first arrivals once the samples are inserted in between the PEEK parts (total length of the PEEK is 200.04 mm).

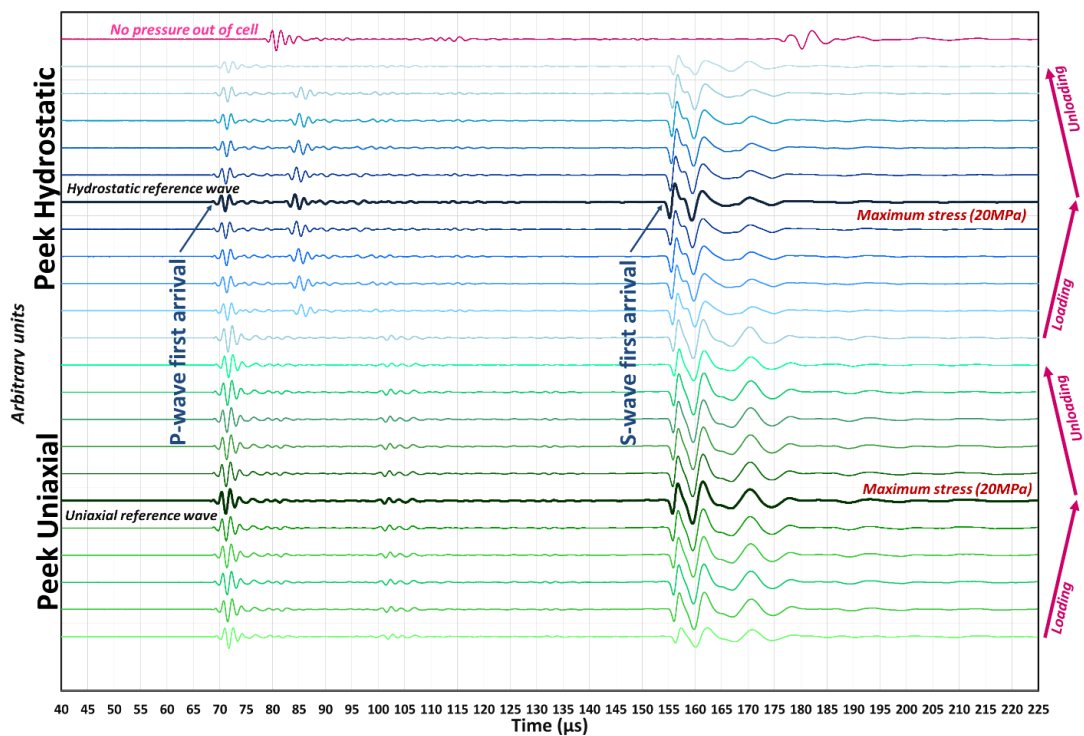


Figure 2-12 Waveforms of the calibration test of the PEEK for both uniaxial and hydrostatic dynamic test for a full cycle of loading and unloading. The black wavelet in the middle of each cycle represents the reference wavelet at the highest applied stress. The first arrivals of P- and S-waves are marked on the graphs for the reference wavelets.

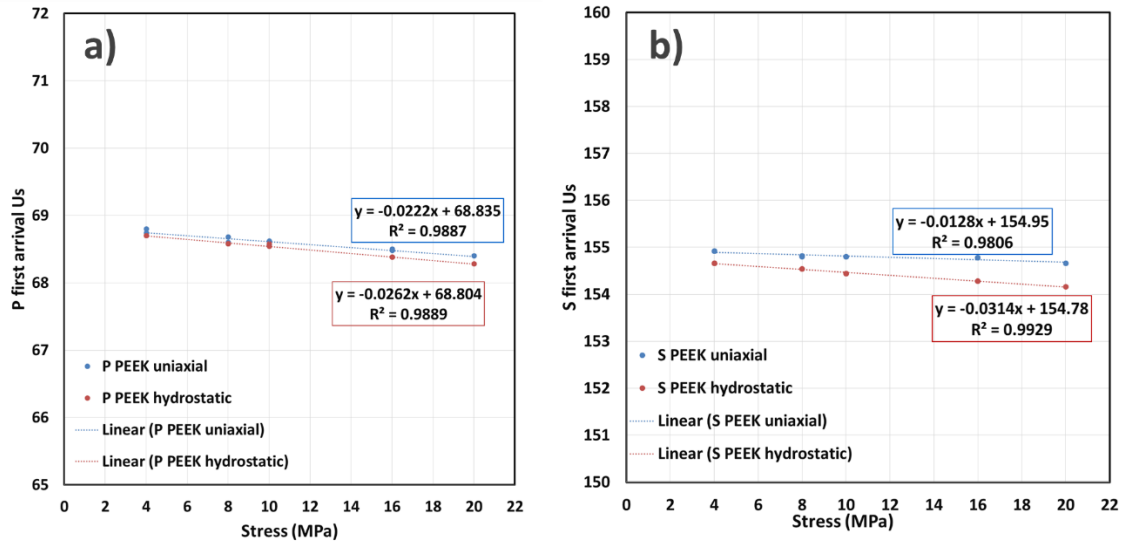


Figure 2-13 PEEK calibration results (PEEK length is 200.04 mm) and the equation of the line at varying stresses for uniaxial and hydrostatic test on correction of P- first arrivals (a) and S-first arrivals (b) in µsecs.

2.6.2 Static set-up

As mentioned above, the static Young's modulus and Poisson's ratio were determined based on the ISRM 2007 standard by analysis of stress-strain graphs. Axial and diametric deformations and the slope of the plotted data determine the static elastic Young's modulus. For the Bulk modulus the volumetric deformation was measured at each applied stress point and the corresponding Bulk modulus was calculated. The static graph for the diametric and axial deformations is plotted in *Figure 2-14* for Bentheimer sandstone under uniaxial stress. The static and dynamic results on the Bentheimer sandstone in the uniaxial experiment show an increase of 54% for dynamic Young's modulus by comparison to static Young's modulus for the same sequences of stress; however, the results show a 50% decrease of dynamic Poisson's ratio with regards to static Poisson's ratio for the sample (*Figure 2-15*).

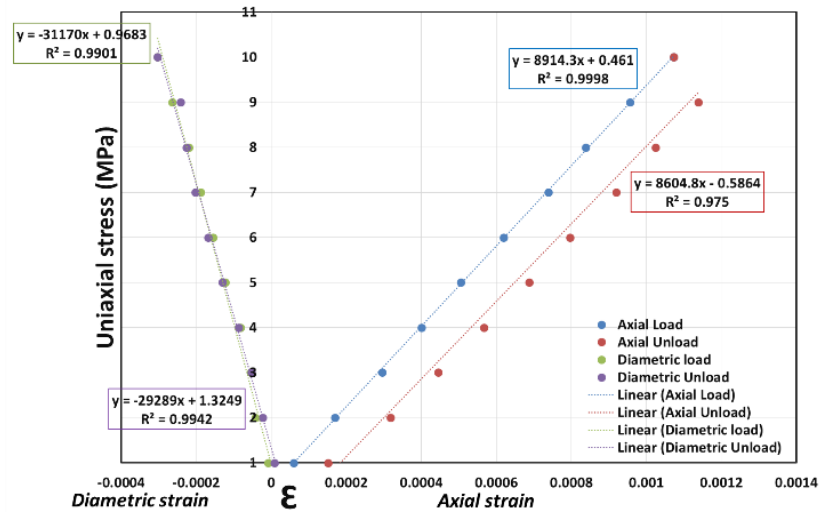


Figure 2-14 Stress-strain graph of Bentheimer sandstone in one cycle of loading and unloading.

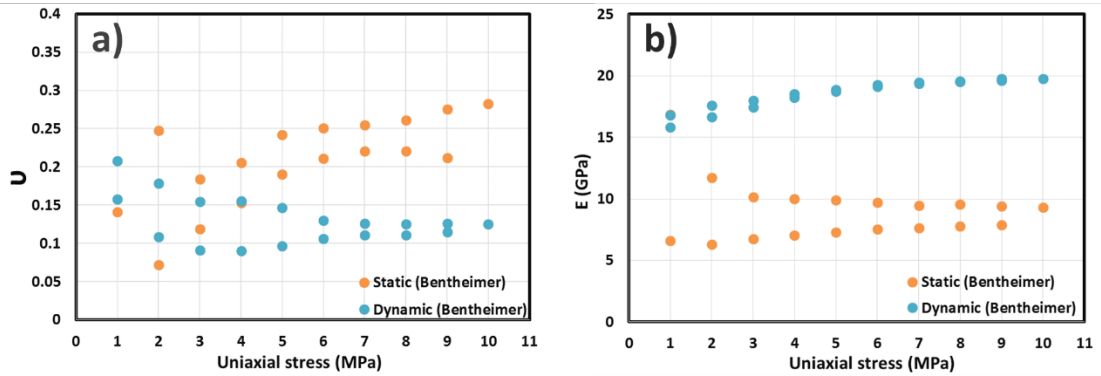


Figure 2-15 Poisson's ratio (a) and Young's modulus (b) of Bentheimer sandstone measured by dynamic and static set-ups simultaneously.

For Upper gray sandstones The V_p/V_s ratio showed 6% to 7% difference for loading–unloading of the two cycles in the case of the hydrostatic stress experiment, and that may be due to the fact that by applying hydrostatic stress no secondary micro fractures were created to increase the anisotropy axis in the matrix of the rock. Therefore, we cannot see a noticeable or significant difference in the loading–unloading V_p/V_s ratio for both cycles (Figure 2-16). The simultaneous static measurement of sample 31 is plotted in Figure 2-17.

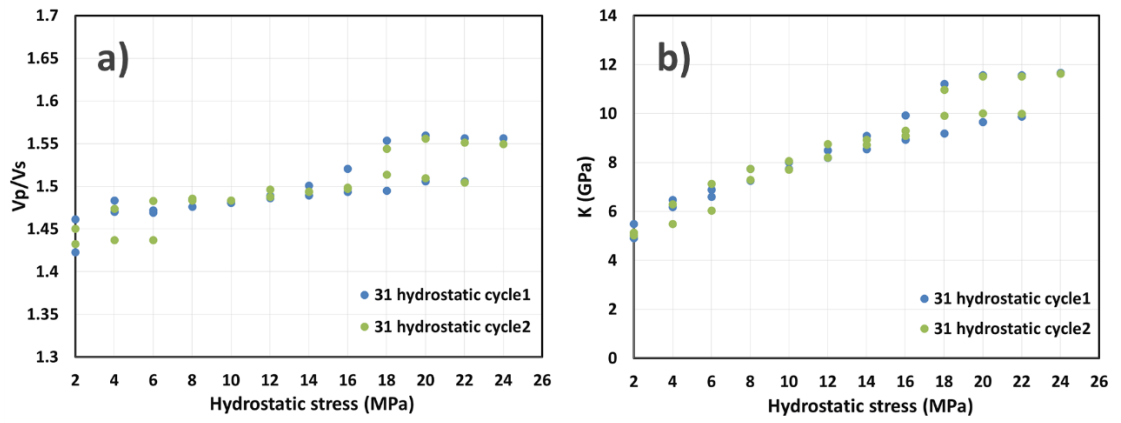


Figure 2-16 Dynamic results of Upper gray sample 31 experiment on the V_p/V_s ratio (a) and dynamic Bulk modulus (b).

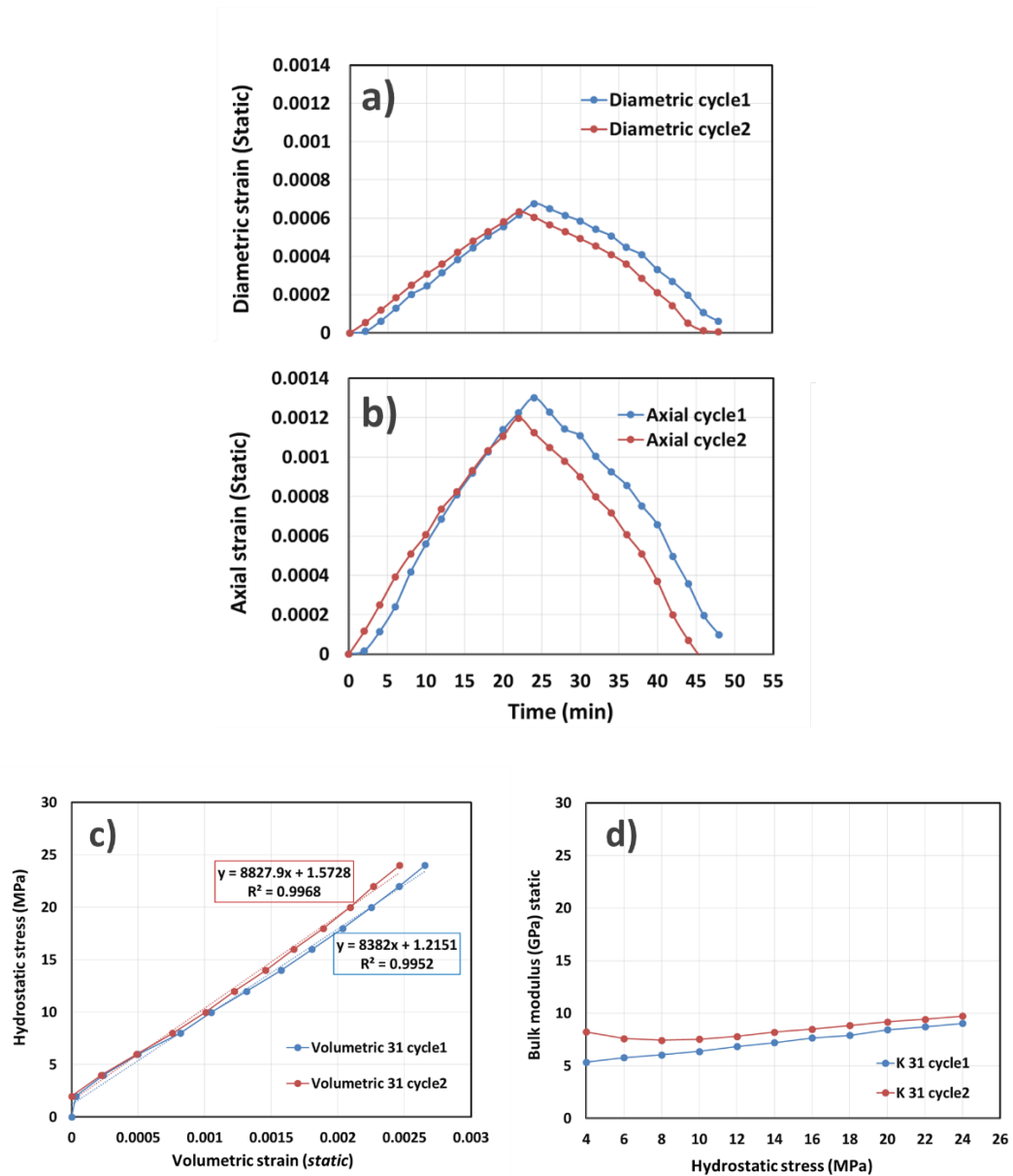


Figure 2-17 Static Bulk modulus for sample 31 calculated on volumetric changes recorded by strain gauges: a) diametric strain, b) axial strain, c) volumetric strain, and d) calculated static Bulk modulus.

Figure 2-18 illustrates the comparison between the Bulk moduli achieved simultaneously by dynamic and static measures on sample 31 by hydrostatic experiment. In this case it is observable that the dynamic values for this sample are higher than those of the same sequence for static measurement; however, unlike other sandstones this difference is less than 40%, which has been recorded in this study. This

sample shows the difference in static and dynamic Bulk modulus by an average of 17% and 10% for first and second loading/unloading cycles respectively.

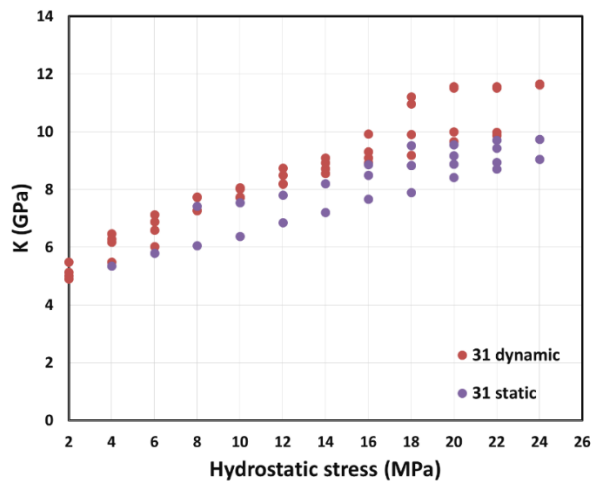


Figure 2-18 Comparison between Bulk modulus for sample 31 by dynamic and static measured simultaneously by hydrostatic experiment.

2.7 Results and discussion

2.7.1 Young's modulus results in comparison with the empirical equations to predict E static

The static and dynamic elastic moduli relationship in different rock formations have been studied in the scientific literature for many years. It has been reported in multiple studies that dynamic Young's modulus has an approximately 40% higher value than static value. Our results show this value as: 1) 41 Berea 56%, 2) Bentheimer sandstone 60%, 3) 12 Bandera gray 57%, 4) 13 Bandera gray 13% 5) Donny brook 88% and, 6) PMMA 8%. Most of the samples show a higher value than 40%, yet from one group (Bandera gray), the two different responses are much more similar which indicates how varied the properties of one formation can be. As expected for PMMA this value was less than 10%, which indicates that although we had only one axis of stress and by higher pressure we created VTI anisotropy, the dynamic formula can still be used for to estimate the dynamic properties of this material. The function that best describes such a relationship cannot be expected to be linear or to depend on a single parameter. This should be noted that both static and dynamic values calculated simultaneously while the samples were subjected to uniaxial stress.

In this study we investigated the relationships proposed in the literature for soft rock formations. We investigated the classic models of linear and nonlinear relationships in

the literature, which are proposed to have the value of R^2 equals 0.97 and 0.99 for linear and nonlinear relations respectively. The power correlation of compressional wave velocity and static modulus has also been proposed in the classic studies, which give R^2 of 0.99. Since in our study we have simultaneously measured the static and dynamic Young's modulus, we could put the proposed empirical equations into the test and see which one was best matched our study to achieve static Young's modulus from dynamic values. Based on our sample types (porous sandstones) we were limited to using the equations listed in *Table 2-2*.

<i>Eq</i>	<i>Referenc</i>	<i>Relationship</i>	<i>R²</i>	<i>E_{dyn}</i> <i>(GPa)</i>	<i>Rock</i> <i>formation</i>
10	Vanheerden (1987)	$E_{st}=0.097E_{dyn}^{1.485}$	-	20-135	Sandstone-granite
11	Eissa and Kazi (1988)	$E_{st}=0.74E_{dyn}-0.82$.7	5-130	All types
12	Eissa and Kazi (1988)	$\text{Log}10E_{st}=0.77\text{log}10(\rho_{bulk}E_{dyn})+0.02$.92	5-130	All types
13	Christaras et.al (1994)	$E_{st}=1.05E_{dyn}-3.16$.99	25-110	All types
14	Lucy (1997)	$E_{st}=0.018E_{dyn}^2+0.422E_{dyn}$	-	-	Sedimentary
15	Nur and Wang (1999)	$E_{st}=1.153E_{dyn}-15.2$	-	-	Est>15 GPa
16	Gueguen and Palciauskas (1994)	$E_{st}=0.932E_{dyn}-3.421$.97	25	All types
17	Heap et.al(2014)	$E_{st}=0.679V_p^{2.664}$.99	20	All types

Table 2-2 The proposed linear and nonlinear empirical equations for sandstone to estimate the static Young's modulus.

By plotting all the eligible equations based on the recorded dynamic Young's modulus Figure 2-19 was extracted. It can be seen that Equations 10 and 15 best represent most of the tested samples. More specifically, for Berea sandstone Eqs 15 and 16 provide the best representation; for Bentheimer sandstone see Eqs 15 and 10; for Bandera gray 12, Eqs 15 and 10; for Bandera gray 13, Eqs 12 and 13; and for Donny brook Eq. 10 was the best representative of the estimated static E.

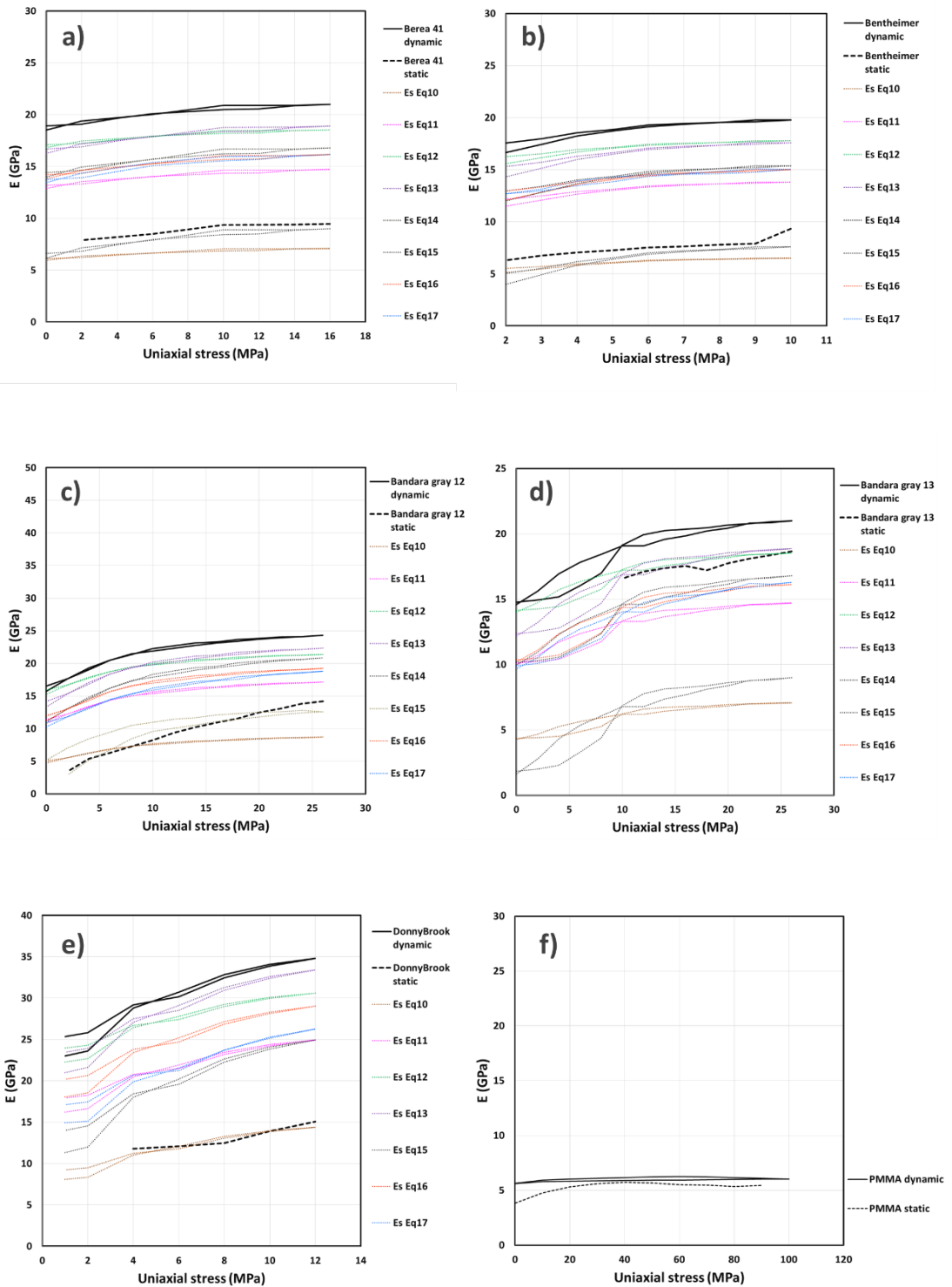


Figure 2-19 Measured static and dynamic Young's modulus vs the static estimated Young's modulus by empirical equations at Table 1-2 for Berea (a), Bentheimer (b), Bandara gray (c, d), and Donny brook (e) sandstones and PMMA (f).

Figure 2-20 illustrates Poisson's ratio, measured by simultaneous static and dynamic experiment for all six samples that had been tested in uniaxial format. For Berea,

Bandara gray 13 and PMMA the measured values are in good agreement in both static and dynamic measurement. Poisson's ratio measured by two approaches shows a bigger difference for Bandara gray 12 and Donny brooks sandstones.

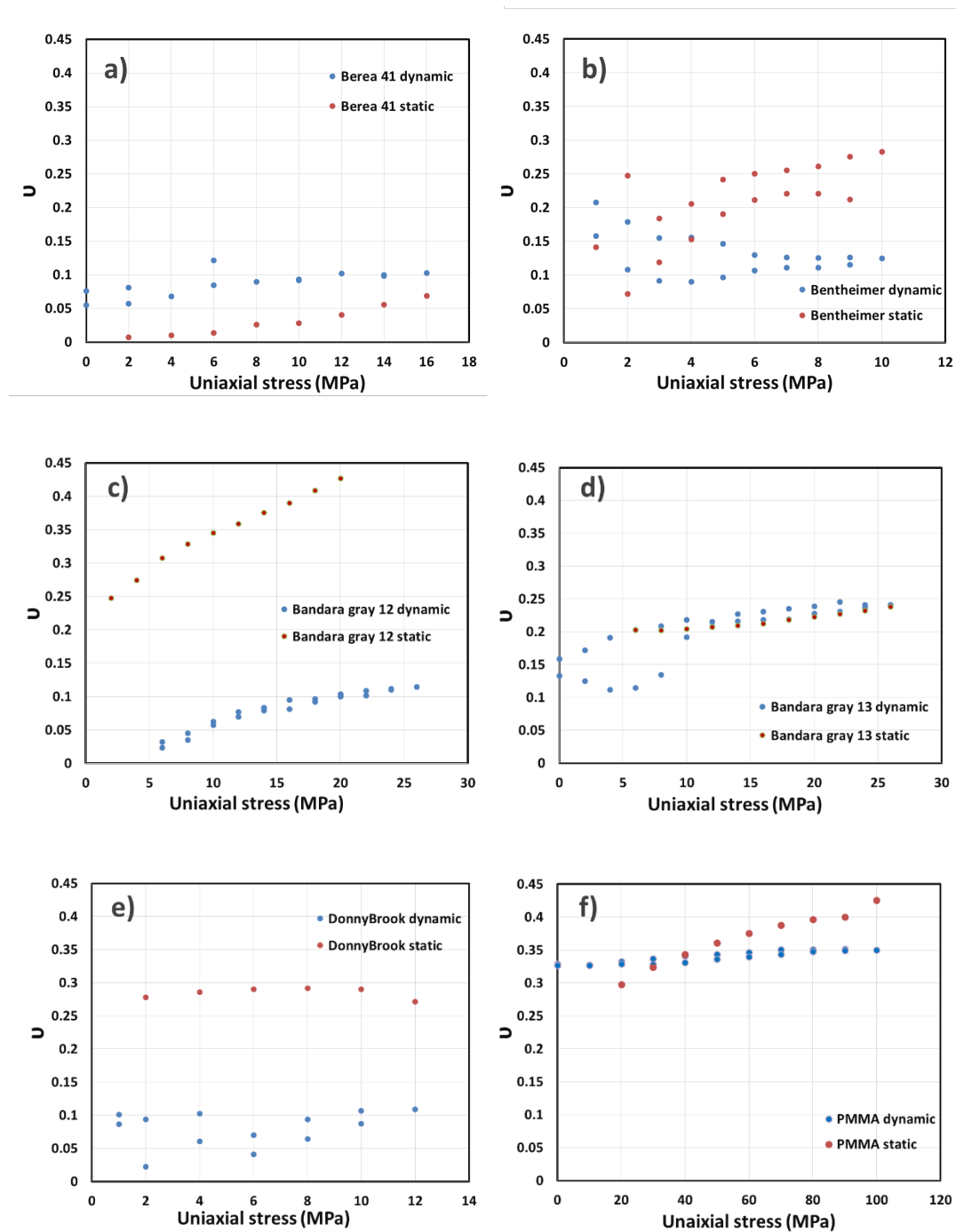


Figure 2-20 Poisson's ratio measured by uniaxial experiment for both static and dynamic approaches for Berea (a), Bentheimer (b), Bandara gray (c, d), Donny brook (e), and PMMA (f) samples.

2.7.2 Bulk's modulus results from static and dynamic measurements

Six samples were tested using a hydrostatic approach in this study. Such a stress format enables the sample to behave within the isotropic region; therefore, in an ideal case no secondary axis of symmetry should be expected to form. However, due to the nature of our natural material and the unknown distribution of features (i.e., pores and micro-cracks) inside the rock matrix we need to compare our observations with these models regarding how predictable the static and dynamic measurements actually are. The test results showed that, by comparison to uniaxial experiments, hydrostatic measurements show ranges of static to dynamic values of 5% to 40% difference. For Bandera gray both tested samples show 44%, Castle gate 16%, Sister gray 5% and PMMA 5% higher value of dynamic Bulk modulus for the full cycle of loading and unloading (*Figure 2-21*).

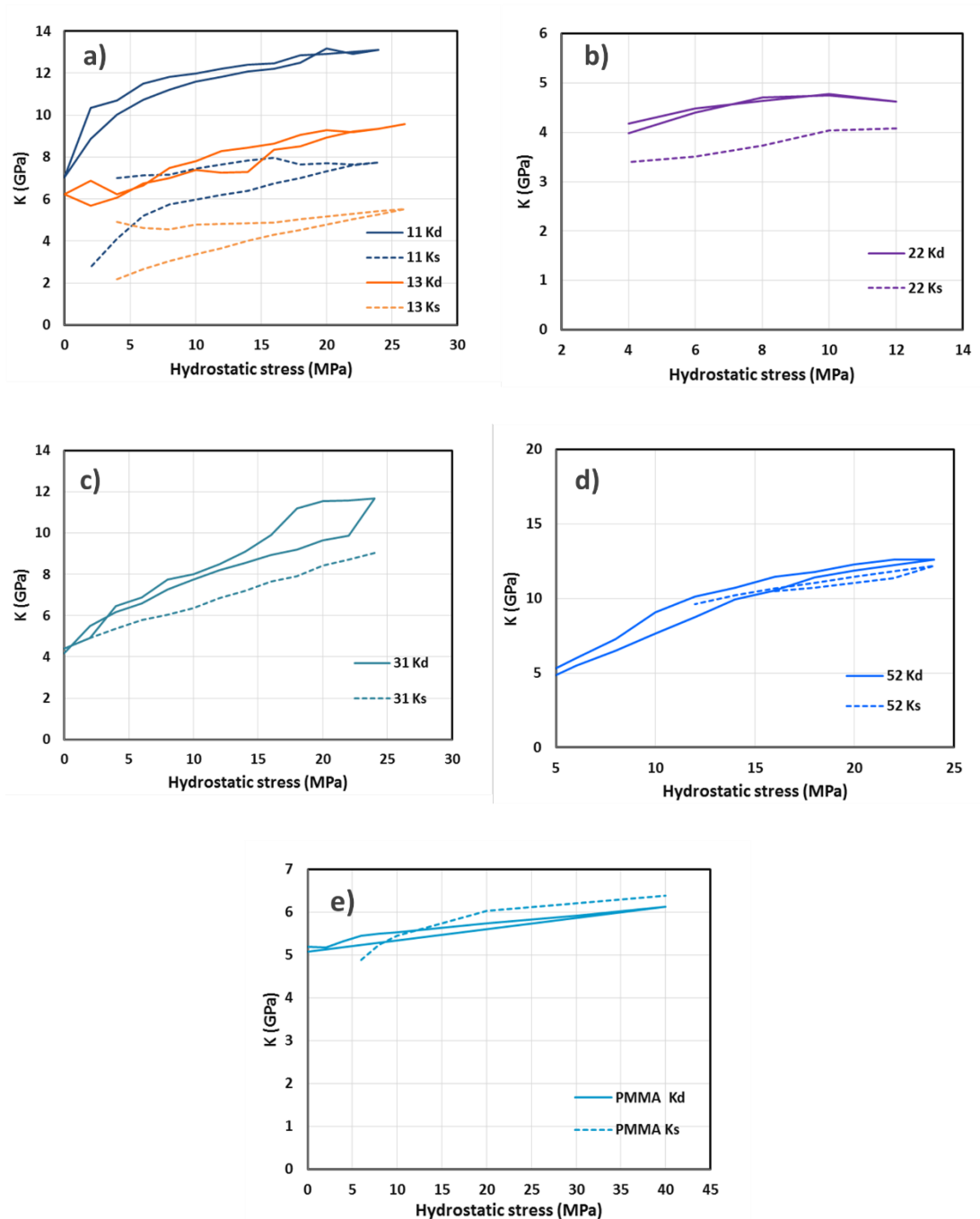


Figure 2-21 Static and dynamic Bulk moduli measured by hydrostatic experiment for Bandara gray (a), Castle gate (b), Upper gray (c), Sister gray (d), and PMMA (f) samples.

2.7.3 Comparison of static and dynamic Bulk moduli for half of the stress cycle (loading)

The laboratory results for Bulk modulus are in agreement with the literature, which indicates that the dynamic Bulk modulus is higher than static Bulk modulus. If we

consider only one cycle of loading and eliminate the unloading part then, the Bulk modulus for PMMA remains within 5% of difference for static and dynamic records (in both increasing and decreasing mode) while for porous natural material – Castle gate, Sister gray and Upper gray sandstones – this difference becomes on average 17%, 6% and 22% respectively. For Bandara gray sandstones number 11 and 13 this difference has been almost identical, with 36% decrease. It should be noted that for a full cycle of loading–unloading the Bulk moduli slightly increases as shown in *Figure 1-21*. By only one cycle of loading the ratio between $K_{static}/K_{dynamic}$ tends to stay below 1 as expected for porous material and almost 1 for PMMA (*Figure 2-22*).

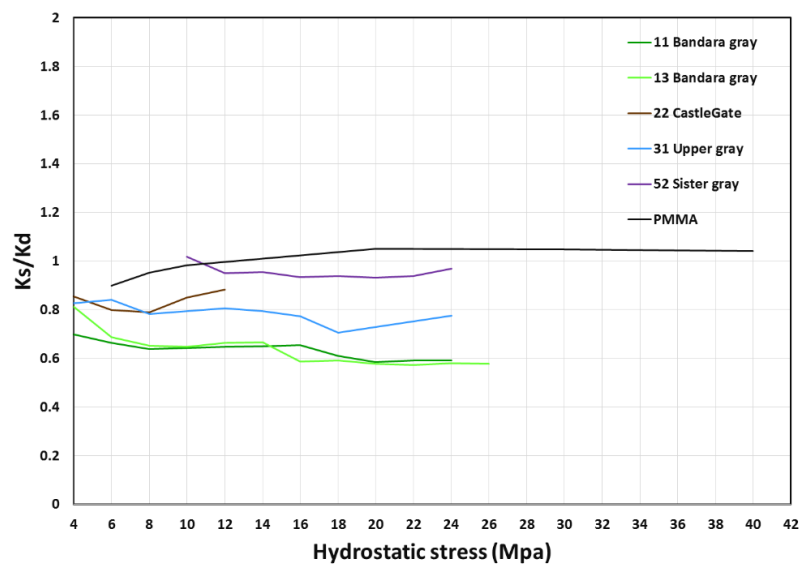


Figure 2-22 Bulk moduli of static and dynamic ratio for Bandara gray, Castlegate, Upper gray, Sister gray sandstones and PMMA.

Simmons and Brace’s 1965 study determined that the main reason for the difference between the static and dynamic modulus is the closure of cracks and cavities inside the rock matrix, which effects the static stress-strain curve. In the experimental study by King (1983) the results showed that once Young’s modulus exceeds 100 GPa then the 1:1 ratio of static and dynamic values can be expected. This observation is useful for igneous and metamorphic rocks; however, for sandstones, reaching that state is practically impossible. Myung and Helander (1972) demonstrated that if we mimic the true stress combination values of the borehole sonic log in the field where the sample has been extracted then the ratio of 1:1 can be observed. Eissa and Kazi’s 1988 study

shows that for soft rocks, the static value of Young's modulus is far lower than the corresponding dynamic value. Due to pore collapse as the result of compaction, for soft rocks irreversible deformation would cause huge differences between loading–unloading cycles and perhaps play a bigger role on the calculated dynamic moduli of the sample.

2.7.4 Pre- and Post-stress measurement on the samples (accumulated residual stress)

By comparing P- and S-wave velocities before and after the stress loading and unloading cycles, the value of relaxation and possible elastic recovery can be studied. All the samples were tested before being inserted into the stress cell by both P- and S-wave transducers. The initial measurement was carried out on fresh samples. The elastic modulus, Poisson's ratio and V_p/V_s ratio were then calculated using the dynamic formulas. Immediately after the application of the stress the samples were tested to monitor the residual stress. Because of the rate of strain for these tests, the relaxation time for each formation varied and therefore we planned to check the velocities systematically for all the samples at three time points: Immediately following the unloading, 20 days after and 60 days after the last test so that this time dependency could be calculated.

The velocities of each sample at four different times during the experiment were plotted into *Figure 2-23*. It can be observed that the highest velocities for both P- and S-waves for all the samples was recorded right after the encounter with stress. The lowest velocity was registered for 2 months after the experiment as a result of the relaxation. In some cases, due to disturbing the inner matrix of the pores and the creation of new cracks, the last sequence of the measurements (after 2 months) recorded a slower velocity than the time before applying any stress. On average, the velocity of P and S waves for all the sandstone samples increased by 7% and 6% respectively right after the stress was released. This velocity then decreased by 8% and 10% for P and S waves after 20 days of stress being released. This decrease continued and was recorded as 9.5% and 10% for P and S waves two months after the tests. Although none of the maximum applying stresses reach the ultimate strength of the samples (50%) it can be clearly observed that the non-reversible effect of plasticity causes such change in velocity, in particular for compressional waves.

The PMMA sample was also checked for residual stress, and the pure elastic behaviour of the sample indicates that we did not reach the plastic region of the graph. Further, after two months no residual stress was observed for this particular sample. The PMMA pressure study for P waves showed a 1.4% increase, and less than a 0.5% increase for S wave velocity right after the stress was released. It should be taken into account that the pure elastic behaviour of PMMA enables this material to return to its initial matrix much faster than sandstones, as indicated by the change of the last sequences of stress (10 to 2 MPa unloading), which presented fast changes in velocity until it reaches full release of the stress cell.

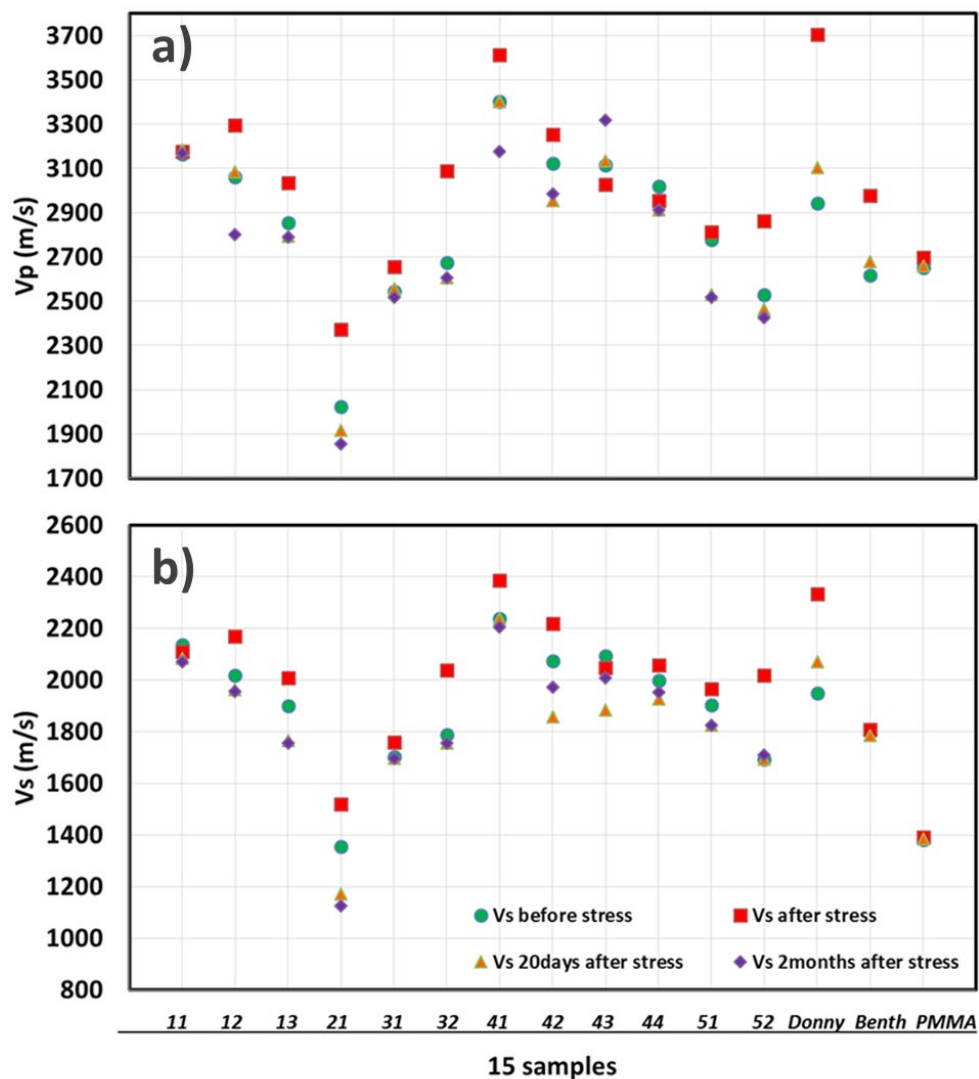


Figure 2-23 Fifteen tested samples: P-and S-wave velocities (a and b respectively) measured before, immediately after unloading, 20 days and 60 days after the experiment to study the effect of the relaxation of stress on velocities.

2.7.4.1 Vp/Vs ratio comparison for pre- and post-stressed samples outside of the stress cell

Experimental dynamic studies rarely take Vp/Vs change into account during the full course of a stress experiment. This time-dependent value is also a good indicator of changes in pores and the creation of new micro-cracks over a long time of recovery after removing the stress. *Figure 2-24* plots these changes at four time points during the stress recovery time for all tested samples. There is no general pattern for all the tested samples because of the different elastic properties of the porous rocks. The general trend for Bandera gray sandstones below 26 MPa hydrostatic and axial loading (35 MPa UCS) shows an increase of Vp/Vs ratio over the relaxation time. The only exception is for Sample 12, which shows the opposite trend after 20 days of relaxation.

This change may be related to the nature of the experiment that was carried out on each sample in this group. Samples 11 and 13 were tested hydrostatically while Sample 12 was tested uniaxially. By applying stress in only one axis we create new symmetry of isotropy and, in other words, we create sample anisotropy by changing the orientation of pores in one specific direction. For that reason, once the stress is released the relaxation behaviour of all three axes can vary. This is in comparison to hydrostatic stress, which compacts the sample in all three principal directions. For the porous Castle gate sandstone, the Vp/Vs ratio increased over time as a result of new pores and cracks opening as a result of stress elimination. Upper gray, Sister gray, Donny Brook, Bentheimer and PMMA showed the opposite trend. For these samples, the Vp/Vs value decreased after stress. On average they showed an increase right after the stress and a gradual decrease over time. PMMA, Donny Brook and Upper gray returned almost exactly to the Vp/Vs ratio that was present before applying the pressure. The rest of the mentioned group decreased even more with regards to the beginning of the test and fresh versions. All the groups that showed a lower value of Vp/Vs ratio after applying pressure possess higher UCS value compared with the group of increasing Vp/Vs value.

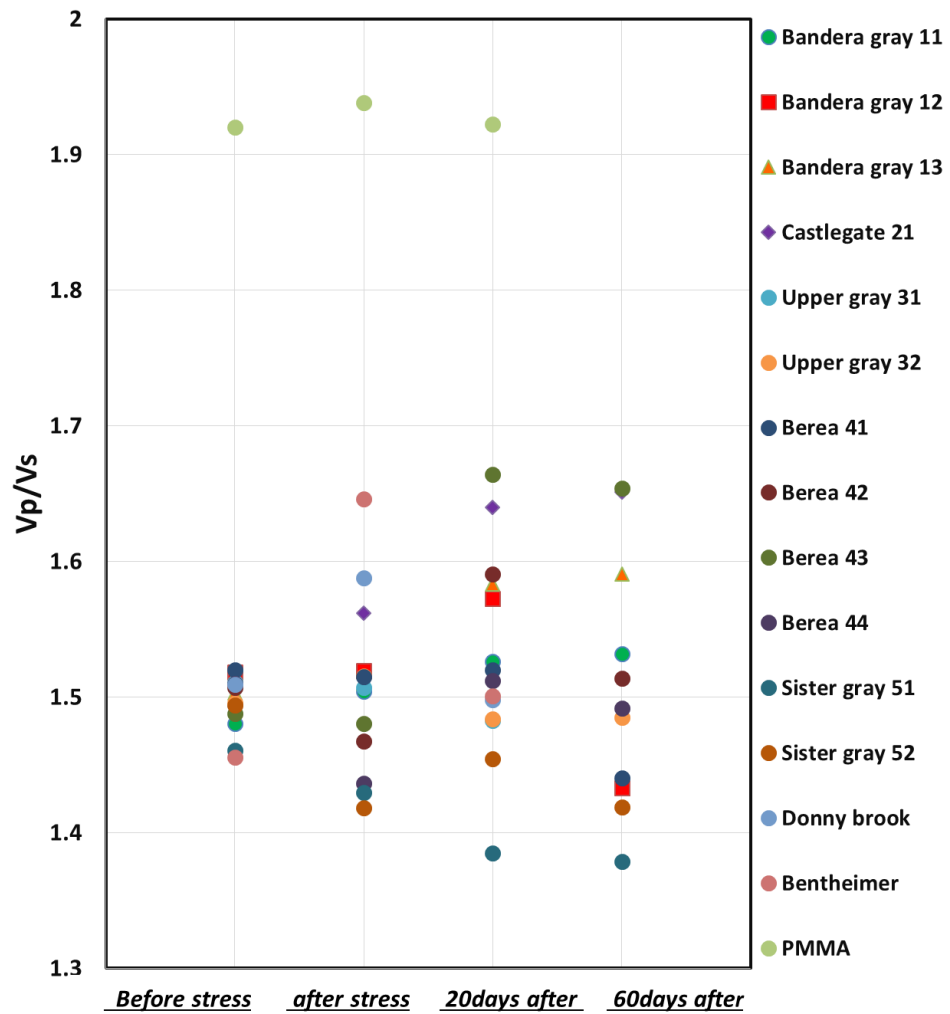


Figure 2-24 The plot of Vp/Vs ratio in pre- and post-stressed conditions for all the tested samples outside the stress cell.

2.7.4.2 Dynamic elastic Young's modulus comparison for pre- and post-stressed samples outside of the stress cell

The dynamic elastic Young's modulus is calculated from Eq. 1. While we do not expect different values for the same group of isotropic material, it should be taken into account that porous geo-material is affected by pores and micro-structures that govern its elastic properties and mean that these can vary even for the same formation of rocks. While we can calculate these values using density and velocities of seismic waves they can vary slightly from sample to sample. Moreover, the dynamic modulus is sensitive

to small anisotropy. Even in static laboratory measurement we rarely see the same results for identical samples of the same group.

The results of the dynamic elastic Young's modulus pre- and post-stress are plotted in *Figure 2-25*. For Bandera gray sandstone samples we observed dynamic elastic modulus from the range of 15–22 GPa; this modulus was within their initial limits for before and rested after the stress as expected. Porous Castle gate sandstone decreased by 2 GPa of elastic moduli over the course of stress cycles, perhaps because of forming new micro-fractures due to the releasing of the pressure. The Upper gray group presents more stable elastic behaviour as less than 1 GPa difference has been calculated over the course of full stress cycle.

The Bentheimer and Donny Brook sandstones presented a different trend to the other groups. Following the compaction and after the stress cycle was completed their dynamic elastic Young's moduli increased slightly: by 0.5 and 3 GPa respectively. This can be interpreted as the residual stress needs more relaxation time to return to its original state. The PMMA returned to its original state after the course of 20 days, where we expected relaxation would have had happened.

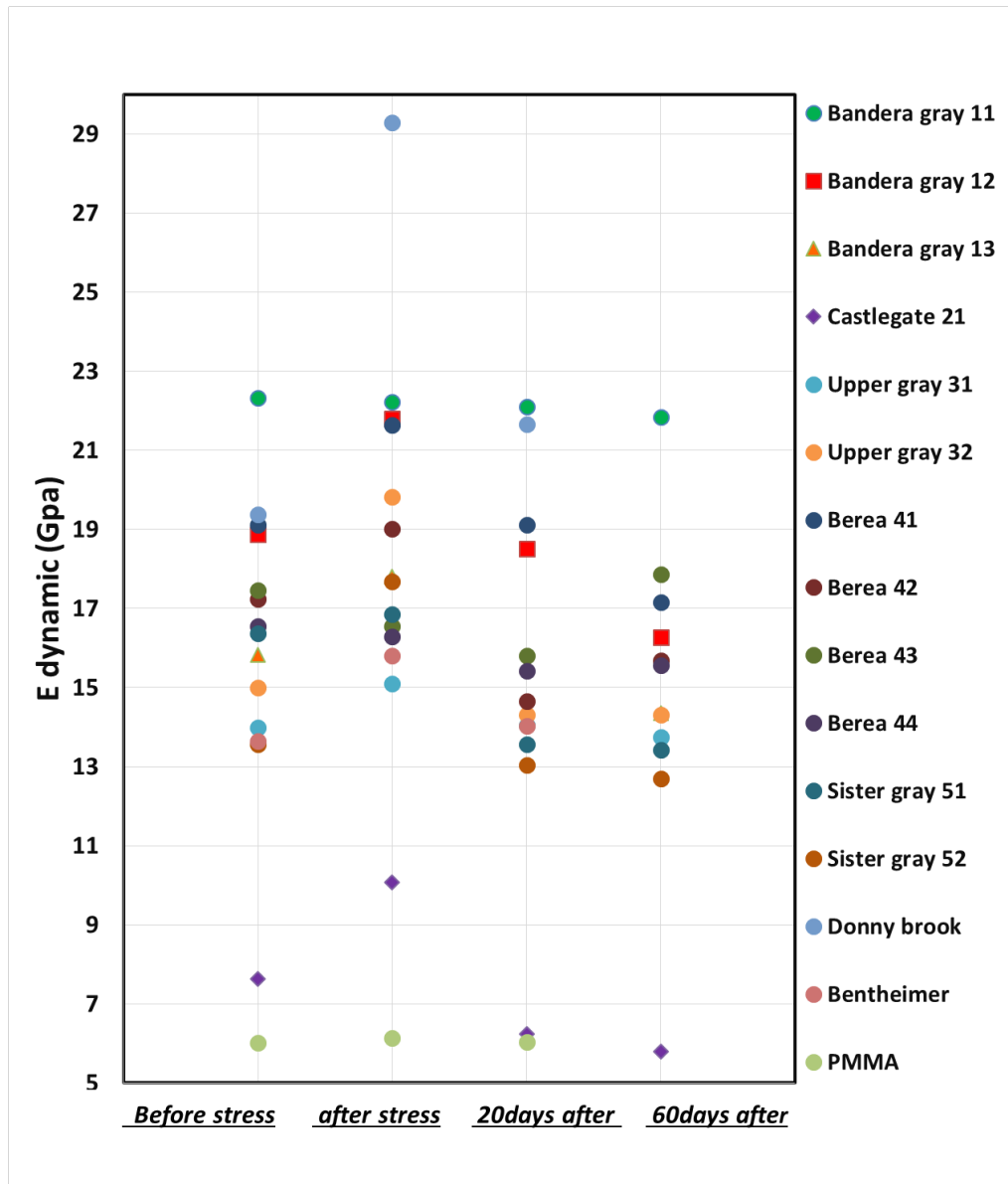


Figure 2-25 Dynamic elastic Young's modulus comparison for pre- and post-stressed samples outside of the stress cell.

2.7.4.3 Dynamic Poisson's ratio comparison for pre- and post-stressed samples outside of the stress cell

Dynamic Poisson's ratio is calculated at room condition from the seismic velocities by equation 2.2 in the previous section of this chapter. In an isotropic sample Poisson's ratio is directly related to the V_p/V_s ratio.

Because of the relationship between the V_p/V_s ratio and Poisson's ratio in isotropic samples, the Poisson's ratio graphs in Figure 2-26 for all the samples resemble the previous figure of V_p/V_s with one exception – Sample 51, Sister gray. The negative

value of Poisson's ratio may be interpreted as the anisotropy parameter, which reached a point where such an equation is no longer valid to estimate the Poisson's ratio after relaxation time of the sample.

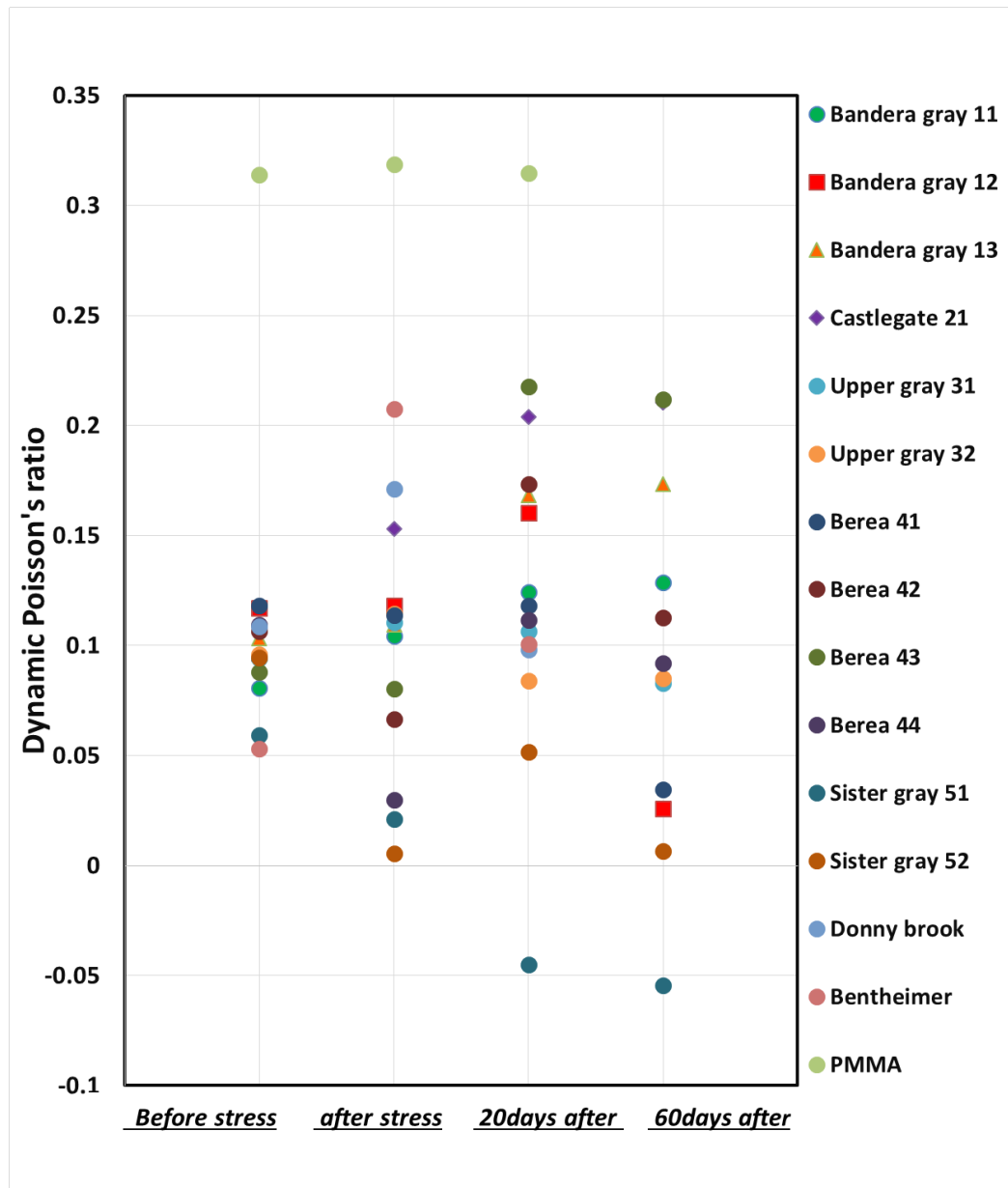


Figure 2-26 Dynamic Poisson's ratio for pre- and post-stressed samples outside of the stress cell

2.8 Dynamic elastic modulus experiment versus classic static elastic modulus experiment

By conducting two sets of experiments simultaneously we had the opportunity to compare the nature of both tests. All the sequences of stress combination for all the

samples in this experiment remained the same, ensuring the accuracy of this statement. While static experiments have been great indicators for many years, they suffer from potential drawbacks. Static laboratory results rely on the accuracy of strain gauges and/or LVDT to register the axial and lateral deformation on the surface of the sample. While this method works well for non-porous engineered materials – such as steels, cast irons and polymers – having pores and micro-fractures in the matrix of the rocks makes such evaluation challenging when using this technique. Strain gauges in particular are highly sensitive to the smallest surface chipping on the edges of the sample even though we have not reached the failure zone. Also to measure axial and lateral changes inside the Hook's cell the strain gauges have to be attached to wires that can easily get damaged or introduce noise at higher pressures while under stress. The most important drawback, however, goes to the localisation of the attached sensors, which is potentially not a good indicator of the whole average body behaviour. Strain gauges cover a small portion of the sample surface, whereas the distribution of pores and the inner structure govern the elastic behaviour of the rocks. Therefore to have a valid average it is best to cover a larger space inside the tested samples. Wave propagation covers such a lack of information for the full body by getting the average of full-volume behaviour.

While static experiments measure mainly from the values of peak events, dynamic experiments can achieve deeper and more consistent data. As a small indication of this, all 15 of the tested samples have no gap of information in all loading and unloading cycles of stress, whereas the static measurement introduces a gap in the data due to measurement errors, damaged wires or sensors at high pressures. In one particular case where the static test showed failure due to the minor edge chipping on the surface of the sample near one of the strain gauges, the dynamic method could still recover a full set of data for the elastic behaviour of the sample in the full cycle (the mentioned sample failed a third cycle later) (*Figure 2-27*). In other words, the static method in this case showed the sample failed, while the dynamic method was still able to record data in precise detail. All the events such as creation and elimination of micro cracks as a result of the stress direction can be achieved by analysis of the recorded full waveform in a consistent pattern of applying pressure. The only drawback of the dynamic method is that it can create anisotropy by having a combination of stresses. Dynamic equations

to calculate the elastic modulus are formulated on the assumption that the sample is isotropic; however, having non-equal stress combinations violates this limitation and, once we reach the point where a sample transits to anisotropy status, this equation is no longer valid. Therefore, the main limitation for dynamic experiments is that it remain in an isotropic status, and this usually possible at low pressure in uniaxial and high pressure (and low pressure) in hydrostatic stresses.

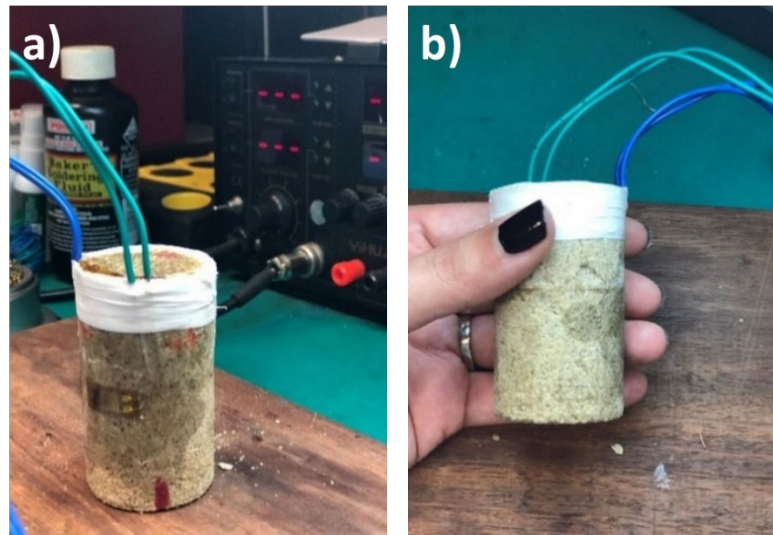


Figure 2-27 Sample 44 Berea failed on the static experiment while the dynamic results showed it did not reach failure point; a) intact top view of the sample, and b) the minor surface chipping led to a failed static experiment.

2.9 Strength Analogues – Uniaxial compressive stress (UCS)

One of the strengths of P-wave velocity based analysis is to characterise the strength of a medium. Uniaxial compressive strength (UCS) is a standard strength analogue in rock mechanics. UCS indicates the material's strength while subjected to compressive stress. The UCS relates to the density and stiffness of a sample. For this reason, P-wave velocity can provide an approximation to estimate UCS value in a non-destructive way, because V_p also depends on density and stiffness. Many past studies have tried to define the relationship between V_p and UCS. They focus on different rock types, but the majority covered the full range of rocks. *Table 2-3* shows empirical equations used in this study to estimate the UCS value for tested samples based on the velocity of P-wave measured at ambient state. A couple of the listed equations established a broad relationship across multiple types of rocks with the aim of creating a general relationship, which we included to check their liability. *Figure 2-28* plots the

estimation of UCS by six empirical equations and comparison to the UCS value provided by the mine site. A couple of the samples were put under UCS test in the lab to check the accuracy of the provided data, and they were in agreement with the used values. The results showed that Equations 18 (Kahraman 2001) and 19 (Kilic and Teymen 2008) estimate UCS very close to the real UCS value in general for porous sandstones. The mentioned equations estimate almost the same value for Bandara gray sandstones 12 and 13 and Donny brook within ± 2 MPa difference. The PMMA UCS was best estimated by Equations 20 (Sharma and Singh 2008) and 23 (Khandelwal 2013). It can be concluded that Equations 20 and 23 largely overestimate the UCS for porous sandstone and are better not to be used for weak rocks.

<i>Eq.</i>	<i>Reference</i>	<i>Relationship</i>	<i>R²</i>	<i>Rock formation</i>
18	Kahraman (2001)	$UCS=9.95V_p^{1.21}$.83	Sandstone and limestone
19	Kilic and Teymen (2008)	$UCS=2.304V_p^{2.4315}$.94	All types
20	Sharma and Singh (2008)	$UCS=0.0642V_p-117.99$	0.9	All types
21	Mishra and Basu (2013)	$UCS=0.05V_p-126.4$.82	Sandstone
22	Minaeian and Ahangari (2013)	$UCS=0.005V_p$.94	Weak rocks
23	Khandelwal (2013)	$UCS=0.033V_p-34.83$.87	All types

Table 2-3 Empirical equations used in this study to estimate the UCS value for tested samples based on the velocity of P-wave measured at ambient.

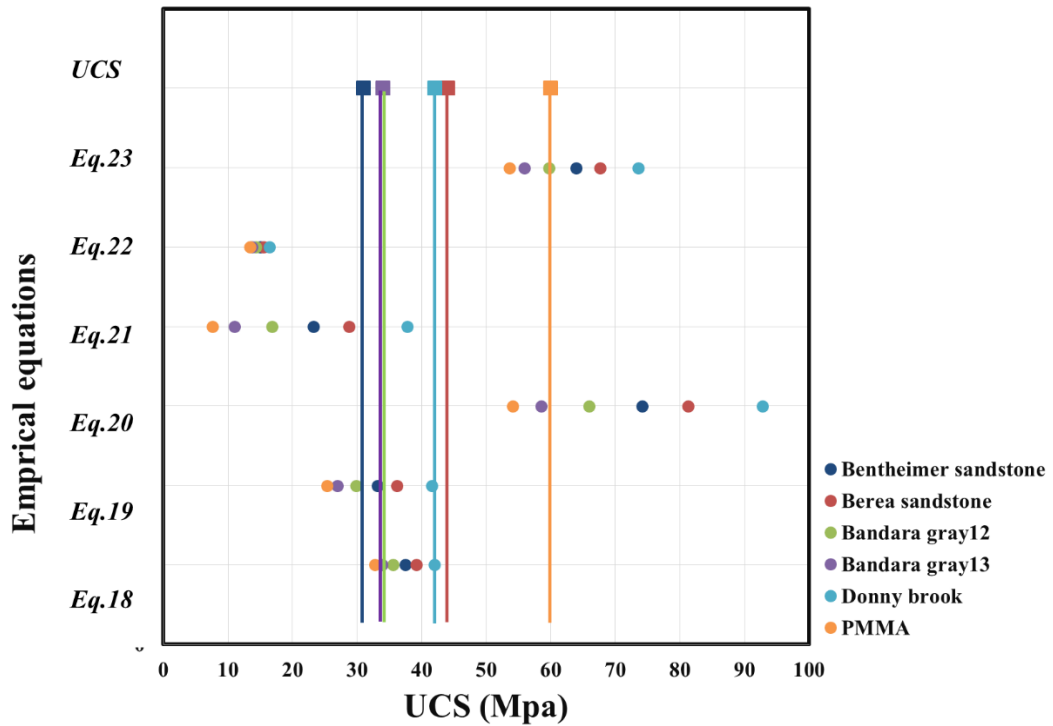


Figure 2-28 UCS estimated values by empirical equations in Table 2-3 compared with UCS value of the samples (base lines marked in same colour solid lines).

2.10 Conclusion and recommendations

The experimental results of this study demonstrated that the dynamic Young's modulus and dynamic Bulk modulus are reasonable estimations for the static Young's and Bulk moduli but should be laboratory calibrated. This study showed that dynamic experiment consistently provides accountable values for the properties of material. Due to the nature of each experiment, the accuracy of the static and dynamic results varies based on the anisotropy induced parameter. It should be noted that the main assumption in using dynamic equations to calculate Young's modulus and Poisson's ratio is that of isotropic conditions. In other words, by applying uniaxial stress we are creating VTI (Vertical Transverse Isotropy), which violates the isotropy assumption; however, by maintaining low pressure, this reduces the degree of uniaxial-induced anisotropy. Dynamic Bulk modulus calculations remain in a better constrained parameter; we did not violate the assumption of isotropy because the hydrostatic nature of the test creates isotropic conditions, and values achieved by dynamic experimentation for Bulk modulus possess higher accuracy than dynamic Young's modulus.

The most important parameter in the correct calculation of dynamic elastic modulus is the correct detection of the S-wave first arrival. In many past studies this important value was estimated by empirical equations such as Christensen's equation. Such an approach introduces significant errors, resulting in corresponding errors in calculation of dynamic elastic modulus because there is no single formula to be used to identify the complex S-wave first arrival, especially for sandstones at low pressure. The current study picked the S-first arrivals by the S-wave transducer via a technique of multiple peaks picking to get the most accurate value. One possible reason for the close value of static and dynamic Young's and Bulk moduli in this study could be the picking S-waves individually for all the stress sequences. Any change in the waveform in that manner can be detected, and corresponding analysis can take place. Among all the possible reasons behind the difference between static and dynamic elastic moduli the one that has not been studied in detail is the effect of strain amplitude on the first arrivals and, as a result, on the registered velocities. This study will be the focus of the next chapter to evaluate such an effect in more detail.

The recommendations of this chapter to perform successful static and dynamic experiments are: 1) Apply uniaxial stress below full compaction of pores (less than 50% of UCS) to avoid any anisotropy induced parameter; 2) for higher stresses use a hydrostatic approach and calculate the Bulk modulus of the material; 3) as a main engineering reference of the material, a dynamic experiment should be accompanied by a minimum of one cycle of simultaneous static round to compare static data to dynamic calculated data for each sample individually, so as not to rely solely on literature. Simultaneous experiments can be achieved by one set of both tests, and correlations to dynamic measured data. The rest of the test can then be carried out dynamically, as this method is less sensitive to edge failure and can be more resilient throughout the full cycle of the loading and unloading of the experiment; and 4) the most important parameter in dynamic calculations is the correct detection of the S-wave first arrival, which should be measured and not estimated by empirical equations.

2.11 References to Chapter Two

Anon 1981. Code of Practice for Site Investigation: BS 5930. British Standards Institution.

Atkinson, J. H., Richardson, D. & Stallebrass, S. E. 1990. Effect of stress history on the stiffness of over consolidated soil. *Geotechnique* 40, No. 4, 531 – 540.

Brotons, V., Tomás R., Ivorra S. & Grediaga A. 2014. Relationship between static and dynamic elastic modulus of a calcarenite heated at different temperatures: the San Julián's stone *Bulletin of Engineering Geology and the Environment* 73:791-799 doi: 10.1007/s10064-014-0583-y.

Burland, J. B. & Lord, J. A. 1970. The load deformation behaviour of Middle Chalk at Mundford, Norfolk: a comparison between full-scale performance and in situ and laboratory measurements. *Proceedings Conference on In Situ Investigations in Soils and Rocks*. British Geotechnical Society, London, 3-15.

Castagna, J. P., Batzle, M. L. & Eastwood, R. L. 1985. Relationship between Compressional Wave and Shear-Wave Velocities in Elastic Silicate Rocks. *Geophysics*, 50, 571 581.

Christaras, B., Auger, F. & Mosse, E. 1994. Determination of the moduli of elasticity of rocks. Comparison of the ultrasonic velocity and mechanical resonance frequency methods with direct static methods *Materials and Structures* 27:222-228 doi:10.1007/bf02473036.

Christensen, N. I. 1985. Measurement of dynamic properties of rock at elevated temperatures and pressures, *ASTM Spec. Tech. Publ.*, 869, 93–107.

Eissa, E. A. & Kazi, A. 1988. Relation between Static and Dynamic Young's Moduli of Rocks. *International Journal of Rock Mechanics, Mining Science and Geomechanical Abstracts*. 25, 479-482.

Entwisle, D. C. & McCann, D. M. 1990. An assessment of the use of Christensen's equation for the prediction of shear wave velocity and engineering parameters.

Goodman, R. E. 1980. *Introduction to Rock Mechanics*. Wiley, New York.

- Gue'guen, Y. & Palciauskas, V .1994. Introduction to the physics of rocks. In: Press PU (ed). Princeton, New Jersey (EE.UU), p 294.
- Heap, M.J., Xu, T. & Chen, C.F. 2014. The influence of porosity and vesicle size on the brittle strength of volcanic rocks and magma. *Bull Volcanol.* doi:10.1007/s00445-014-0856-0.
- Hobbs, N. E. 1973. Effects of non-linearity on the prediction of settlements of foundations on rock. *Quarterly Journal of Engineering Geology*, 6, 153- 158.
- Horsrud, P. 2001. Estimating Mechanical Properties of Shale From Empirical Correlations Society of Petroleum Engineers, SPE doi:10.2118/56017-pa.
- Ide, J. M. 1936. Comparison of statically and dynamically determined Young's modulus of rocks. *Proceedings of the National Academy of Science*, A. 22, 2,81-92.
- ISRM (International Society of Rock Mechanics) 1979. Suggested Method for Determining the Uniaxial Compressive Strength and Deformability of Rock Materials *ISRM Suggested Methods 2*:137-140.
- ISRM (International Society of Rock Mechanics) 1981. *Rock Characterisation, Testing and Monitoring: ISRM Suggested Methods'*. BROWN, E. T. (ed.) Pergamon, Oxford.
- ISRM 2015. *Suggested Methods for Rock Characterization, Testing and Monitoring: 2007-2014* / edited by R. Ulusay. Cham: Springer International Publishing: Imprint: Springer 2015.
- Kahraman, S. 2001. Evaluation of simple methods for assessing the uniaxial compressive strength of rock. *International Journal of Rock Mechanics and Mining Sciences*. 38;7, 981-994.
- Khandelwal, M .2013. Correlating P-wave velocity with the physico-mechanical properties of different rocks. *Pure Appl Geophys*. 170, Issue 4, pp 507–514.
- Kılıc, A. & Teymen, E.A. 2008. Determination of mechanical properties of rocks using simple methods. *Bull Eng Geol Environ*. 67:237–244 DOI 10.1007/s10064-008-0128-3.

King, M. S. 1983. Static and Dynamic Elastic Properties of Rocks from the Canadian Shield. *International Journal of Rock Mechanics, Mining Science and Geomechanical Abstracts*, 20, 237-241.

Lacy, L. 1997. Dynamic Rock Mechanics Testing for Optimized Fracture Designs. Paper SPE 38716 presented at the SPE Annual Technical Conference and Exhibition, San Antonio, Texas, USA, 5–8 October.

Lama, R. D. & Vutukuri, V. S. 1978. *Handbook on Mechanical Properties of Rocks*. Trans. Tech. Publications, 196-220.

Lane, R. G. T. 1964. Rock foundations: Diagnosis of mechanical properties and treatment. *Transactions of the International Conference on Large Dams*. 1, 141-146.

Marsland, A. 1971. Large in situ tests to measure the properties of stiff fissured clays. In: *Proceedings of the 1st Australian New Zealand Conference on Geomechanics*, Melbourne. Vol. 1, 180-189.

Martinez-Martinez, J., Benavente, D. & Garcia-del-Cura, M.A. 2012. Comparison of the static and dynamic elastic modulus in carbonate rocks *Bulletin of Engineering Geology and the Environment* 71:263-268 doi: 10.1007/s10064-011-0399-y.

Mavko, G., Mukerji, T. & Dvorkin, J. 2009. *The rock physics handbook*: Cambridge University Press.

McCann, D. M. & Entwisle, D. C. 1992. Determination of Young's modulus of the rock mass from geophysical well logs, *Geological Applications of Wireline Logs H*. Geological Society, London, Special Publications, 65, 317-325, 1 January 1992, <https://doi.org/10.1144/GSL.SP.1992.065.01.24>.

Minaeian, B. & Ahangari, K. 2013. Estimation of uniaxial compressive strength based on P-wave and Schmidt hammer rebound using statistical method. *Arabian Journal of Geosciences* 6(6):1925-1931 DOI: 10.1007/s12517-011-0460-y.

Mishra, D. A. & Basu, A. 2013. Estimation of uniaxial compressive strength of rock materials by index tests using regression analysis and fuzzy inference system. *Engineering Geology* 160 DOI: 10.1016/j.enggeo.2013.04.004.

- Myung, J.I. & Helander, D. P. 1972. Correlation of elastic moduli dynamically measured by in situ and laboratory techniques. Transactions of SPWLA 13th Annual Logging Symposium, Paper H.
- Najibi, A.R., Ghafoori, M. & Lashkaripour, G.R. 2015. Empirical relations between strength and static and dynamic elastic properties of Asmari and Sarvak limestones, two main oil reservoirs in Iran Journal of Petroleum Science and Engineering 126.
- Nur, A. & Wang, Z. 1999. Seismic and Acoustic Velocities in Reservoir Rocks: Recent Developments Society of Exploration Geophysicists 10.
- O'Brien, P. N. S. 1953. Velocity dispersion of seismic waves. Geophysical Prospecting, 19, 1-12.
- Sharma, P.K. & Singh, T.N.2008. A correlation between P-wave velocities, impact strength index, slake durability index and uniaxial compressive strength. Bull Eng Geol Environ67:17–22.
- Simmons, G. & Brace, W. F. 1965. Comparison of static and dynamic measurements of compressibility of rocks. Journal of Geophysical Research 70, 22, 5649-5656.
- Sutherland, R. B. 1962. Some dynamic and static properties of rocks. Proceedings of the 5th Symposium on Rock Mechanics, Minnesota, Pergamon, New York, 473-490.
- Vanheerden, W. L. 1987. General Relations between Static and Dynamic Moduli of Rocks. International Journal of Rock Mechanics, Mining Science and Geomechanical Abstracts, 24, 381-385.
- Winkler, K. W. 1986. Estimates of Velocity Dispersion between Seismic and Ultrasonic Frequencies. Geophysics, 51, 183-189.

Chapter 3 The effect of wave amplitude on ultrasonic wave velocities in porous media

3.1 Foreword

The previous chapter illustrates that one possible reason for the difference between static and dynamic elastic moduli relates to the strain amplitude of the elastic waves. This particular phenomenon has not been experimentally studied previously with a focus on the dependence of velocity on the strain inside the wave. Considering the importance of correct velocity measurement, this chapter looks deeply into one important parameter affecting first arrivals in both P- and S- ultrasonic waves. The complete text of this chapter has been published in *Geophysical Prospecting* for P-wave strain amplitude, and the study of S-wave strain amplitude has been published in *Exploration Geophysics*.

3.2 Abstract

Rock physics models are widely used for reservoir characterisation in seismic studies. By improving the models, especially for reservoir rocks, more realistic characterisations and inversion of geophysical data, such as 3D reflection seismic or VSP can be achieved. To calibrate such models, the elastic properties of reservoir porous rocks have been measured by ultrasonic techniques for many years. In conventional ultrasonic methods used in laboratories, the local strain inside the wave is much higher than that in field experiments. The knowledge of how the velocity of the ultrasonic wave depends on the strain is important for interpretation of the results of the experiments. Ultrasonic waves can produce relatively large strains inside the sample, and thus change the properties of the sample. To investigate the effect of strain amplitude on the P-wave and S-wave velocities, a series of ultrasonic wave propagation experiments were carried out on natural and engineered samples.

3.3 The effect of strain amplitude produced by ultrasonic waves on its velocity¹

3.3.1 Introduction

Ultrasonic methods are widely used in investigation of the elastic properties of materials including rocks. Laboratory experiments using transducers date back to Kaufman and Roever (1951) who were probably the first to implement electromechanical transducers for the generation and recording of waves in the laboratory. Piezoelectric transducers are simpler in design than electromagnetic ones and, thus, nowadays are widely used in lab measurement, mimicking the large scale of field experiments in the labs (Riznichenko, 1966; O'Brien and Symes, 1971). The precise laboratory measurements of wave velocities are important because they are not only used for the calibration of log and seismic data; laboratory experiments are also used to calibrate and validate theoretical models that explain and quantify various effects of dependency of velocities with frequency and/or pore fluid; for example, a “squirt” effect (Mavko et al. 2009).

To obtain the elastic moduli of a tested sample, a source transducer is attached to a sample. After applying a short electrical pulse to the source, the source transducer produces a mechanical disturbance on the sample's boundary, thus small elements inside the sample are moving out of the position of equilibrium, forming an elastic wave. This wave propagates through the sample. The maximum displacement of the element from the position of equilibrium is called the wave amplitude. The time of an arrival (“arrival time”) of the wave on a known distance (“travel path”) can be measured by a receiver transducer. This receiver converts the mechanical displacement of the sample's surface into an electrical signal, which is recorded by an acquisition system, for example, an oscilloscope. The amplitudes of a wave should be small, so that the elasticity theory can be applied to recover the elastic moduli of the samples. However, the amplitudes of ultrasonic waves are not taken into account in experimental studies. Moreover, the experimental conditions – especially the type of

¹ This subchapter 3.3 is an extended version of the paper “Research note: The effect of strain amplitude produced by ultrasonic waves on its velocity”

piezoelectric source and applied voltages – often are not described in detail. Thus it is difficult to compare the results produced by different authors.

Another approach to obtaining the elastic properties of samples is to use a resonance bar technique (Winkler and Nur, 1982; Nakagawa et al., 2013), in which frequency characteristics of self-resonance on a long sample is measured in detail. Winkler and Nur (1982) show that the wave velocity in dry sandstone calculated from a resonance bar technique decreases with the strain induced by vibrations. The linear theory of elasticity assumes that the strain inside an elastic medium is directly proportional to applied stress, and vice versa. However, materials and especially granular media are not elastic. A granular medium has many contacts between the grains, and these contacts are not purely elastic. Thus we may expect some violations of linear elasticity theory. In such a case, the stress–strain relationship or Hooke’s law can be expressed as:

$$\sigma = M (\varepsilon + \beta\varepsilon^2 + \delta\varepsilon^3 + \dots) \quad (\text{Eq 3.1})$$

Where, σ is stress, M is elastic modulus, and ε is strain. β and δ are the nonlinear parameters (Landau and Lifshitz, 1986). To recover such non-linear parameters β and δ , it is necessary to measure ε directly (Gallot et al., 2014).

Thus if the amplitude of the wave inside the media is increasing we may presume that the stress induced by such a wave will increase nonlinearly, moduli will increase with the applied stress, and thus the velocity of the propagating wave may increase with the wave amplitude. The effect of the strain amplitude generated inside the sample from outside stress on wave propagation and especially on wave attenuation has been previously studied (Johnson et al., 1996; Ten Cate et al., 1996; Zinszner et al., 1997; Ostrovsky et al., 2001). However fewer experiments (Winkler and Nur 1982; Zaitsev et al. 1999; Mashinskii 2004 and 2005) were carried out to investigate the dependency of the velocity of a wave on the strain produced within the wave.

Mashinskii (2004 and 2005) found that the velocity of ultrasonic wave in sandstones increases with increasing applied voltage to the sources transducer; however, the strain inside waves was not directly measured, but only estimated from the properties of piezoelectric materials. Thus, it is difficult to quantify such an effect using proxy

relationships. We conclude that the results of different authors are not consistent with each other, thus it is necessary to experimentally investigate more rigorously the phenomenon of velocity dependency on the strain inside a wave. Moreover, to quantify the possible effects, the direct and simultaneous measurements of both the elastic wave velocity and the strain inside the wave are required. To fill this gap, in this chapter we directly measured the strain in the compressional ultrasonic wave with a Laser Doppler interferometer (LDI). We also measured the ultrasonic wave velocity using a common experimental set-up and commercially available piezoelectric transducers; then, we analysed the velocity and the strain data together.

3.3.2 Experiment

Cubic samples have made from the Gosford sandstone, Aluminium and Polymethylmethacrylate (PMMA) are the subjects of experiment in this study. The thicknesses of these samples are 20 mm, 50 mm, and 40 mm respectively. By choosing such thicknesses we will have approximately the same numbers of wavelength of ultrasonic wave propagating inside the Gosford and Aluminium samples. Gosford sandstone consists of fine grain quartz in a clay matrix with a measured porosity of about 8%. This sandstone can be assumed to be a homogenous material for this test.

The ultrasonic system includes a pair of V102 P-wave transducers (Olympus, Ltd). Such transducers are 23 mm in outer diameter, housing a piezoceramic disk of 19 mm in diameter inside. The central frequency of these Videoscan-type transducers is 1 MHz. A pulser/receiver 5077PR (Olympus, Ltd) electronic block, and a digital, 200 MHz, 2-channel oscilloscope TDS2022C (Tektronix, Ltd.), were used to apply and record electrical signals. To achieve the best coupling between the transducer and the sample, the source transducer was glued using superglue coupled to the center of the sample surface. We applied a square wave electrical pulse of 1 μ s in duration, with amplitude voltages ranging between 43 to 400 V, to this source transducer. The source transducer generates a mechanical pulse at the sample's boundary, thus an ultrasonic wave propagates inside the sample. Upon wave arrival at the opposite surface of the sample, the rate of the displacement of the free surface (i.e. the particle velocity) is measured by a Laser Doppler Interferometry (LDI) sensor system. The LDI consists of a Vibrometer Controller OFV-5000, and Vibrometer Sensor Head OFV-503 (both units are from Polytec Ltd.). Electrical signals were acquired at a sampling rate of 50

MHz. Figure 1a shows the setup, illustrating the right-angled position of the laser beam on the top surface of the sample. All the equipment was set on a noise-cancelling platform to avoid any environmental vibration. After LDI measurements, the receiver transducer was glued on the middle of the free surface (the same focus area as the LDI laser beam) and the wave velocity was measured by a pair of ultrasonic transducers using a standard setup. The large diameter of the transducers and samples allow us to measure the group velocity, which equals to a phase velocity in this case.

These experiments required very precise measurements of the elastic wave travel times. Thus we were very careful in the calibration of the system, especially to all possible time delays in the electronics, which are often called “dead time”. Before conducting the experiment on the samples, we glued transducers together face-to-face to determine dead time in a two-transducer ultrasonic set-up. Dead times were measured for all possible settings of applied voltages and acquisitions of pulser/receiver; including variable Gain levels, low and high frequency pass filters settings, and pulse duration. The transducers were carefully unglued afterwards (by immersing into an acetone solution for 24 h). The LDI was focused on a source transducer, and dead times for the LDI set-up were measured at all possible settings. The ultrasonic “dead time” ranged from 0.328 μs to 0.331 μs , and LDI “dead time” ranged from 3.90 μs to 3.91 μs for applied voltages of 100 to 400 respectively.

Proper coupling is another important aspect of such precise measurements. A layer of coupling gel between the transducer and sample is essential for all rock physics lab experiments to ensure efficient energy transfer between the sampling end surface and the measuring device. A large variety of couplant options – including grease, glycerin, putty, vaseline, honey and oil (Aydin, 2014) – has been used widely in previous studies; however, authors of this paper found that the best couplant for detailed measurements is superglue instead of any other couplant gel to eliminate different phases of material and slipping, which have effects on efficient wave propagation.

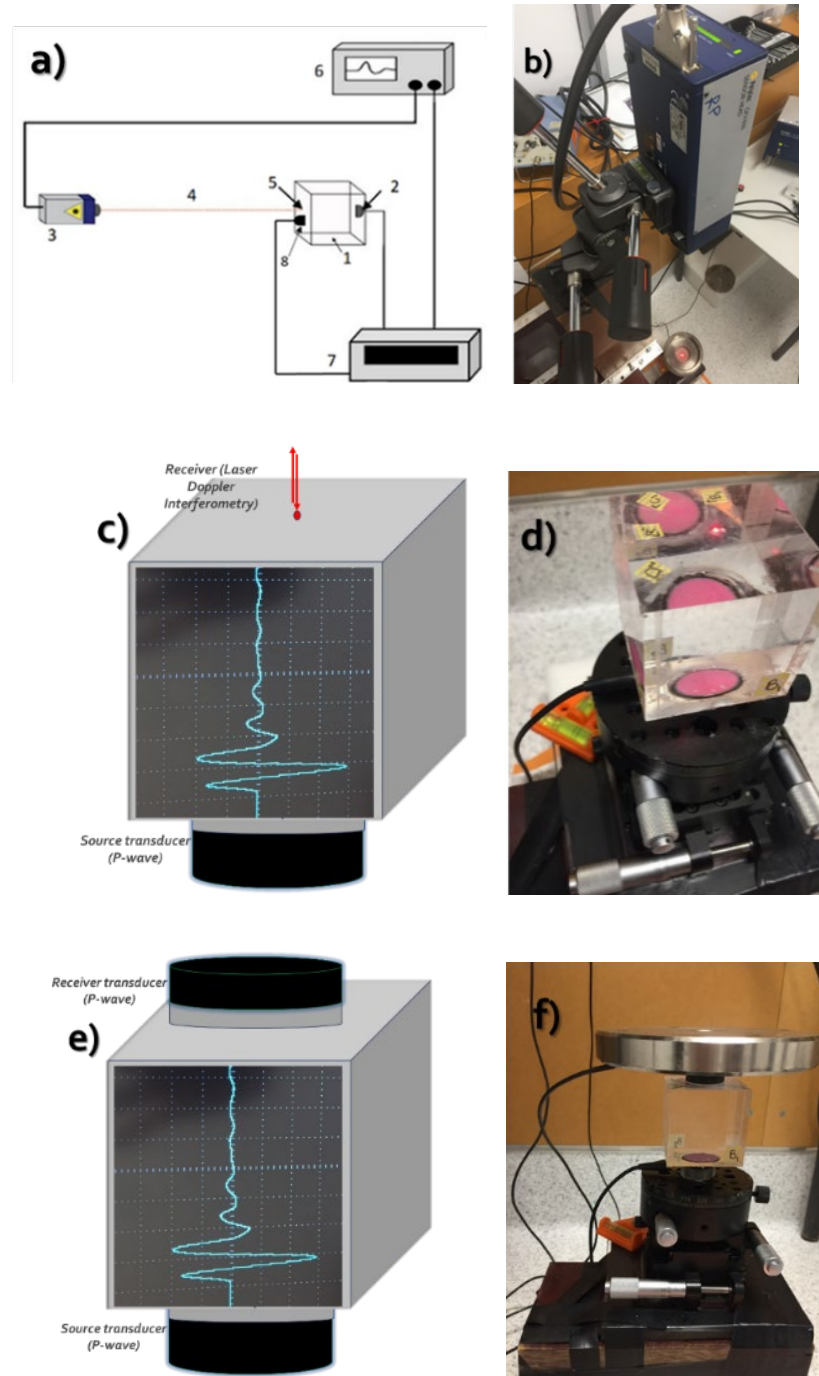


Figure 3-1 (a). Experimental setup. 1: Cubic sample, 2: Source of ultrasonic waves (piezoelectric transducer), 3: Laser Doppler interferometer (LDI), 4: laser beams (emitted and backscattered), 5: Oscilloscope, 6: Pulse generator, (b). Laser beam incident angle of 90 degree on the top of the sample, (c). Schematic position of transducer as source of ultrasonic wave and Laser beam as receiver focused on the on the sample surface, (d). PMMA sample during measurement using Transducer - LDI experiment platform set up, (e). Schematic conventional setup; transducer as a source and transducer as a receiver, and (f). Measurement of PMMA sample using “conventional” ultrasonic platform set up.

3.3.2.1 Strain measurements

A source frequency of 1 MHz generated waves, with wavelengths of 2.7, 6.2, and 3.1 mm was used for the PMMA, Aluminium and Gosford sandstone samples. *Figure 3-1b* shows the setup of the sample for strain measurement using LDI. To make a sample stable during measurements, a 3.5 kg weight was placed on top of the sample with a centre hole to allow the laser beam to pass through (*Figure 3-1a*). The laser beam was focused at a 90 degree incident angle of transmission on the centre of the upper surface of the sample. The LDI measures the rate of displacement of the surface (*Figure 3-2*); thus, to obtain the displacement and to calculate the strain in the wave the signal was integrated as a function of time (Lebedev et al., 2011).

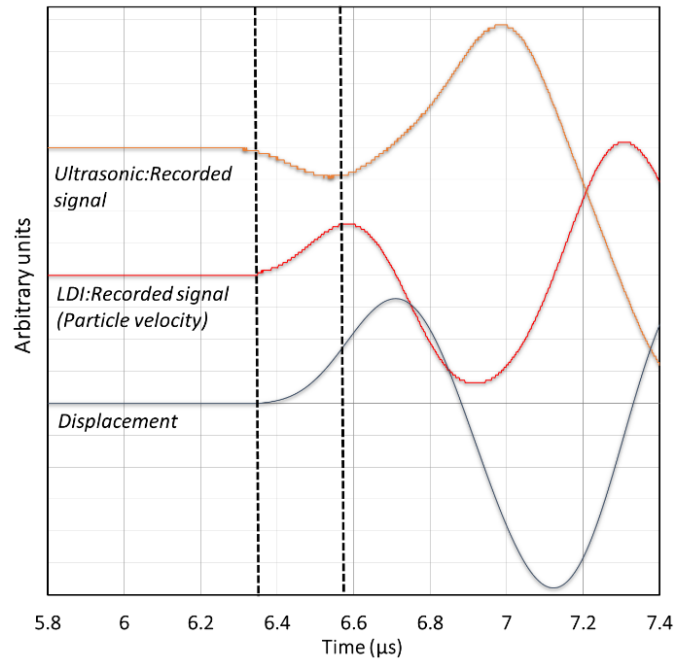


Figure 3-2 Recorded signals: Top - Ultrasonic transducer; Middle –LDI (LDI measures particle velocity) Bottom: Displacement obtained from integration of the LDI signal. Sample Aluminium, 40 mm length, applied voltage to ultrasonic source is 400 V.

We define the strain (ϵ) inside a wave as:

$$\epsilon = d/\lambda, \quad (\text{Eq 3.2})$$

Where d is the maximum particle displacement from the position of equilibrium and λ is the wavelength.

3.3.2.2 *Velocity measurement using an LDI and pair of ultrasonic transducers*

Wave velocities obtained from the LDI system have significant uncertainties, especially for granular media. Thus, the standard time-of-flight method with a pair of transducers was used to measure the velocity. The influence of the coupling conditions between the piezoelectric transducer and the sample surface is another important parameter that impacts our experimental approach, and must be carefully addressed. We solved the coupling problem by, instead of using viscous liquids as a couplant, to use a permanent couplant superglue, for both for the sample-receiver and sample-source transducer interfaces (*Figure 3-1c*). A small weight (3.5 kg) was also placed on the top of the receiving transducer for better coupling. From the first arrival pickings and dimension measurements, the systematic errors for the calculated P-wave velocities were estimated to be less than 0.3%. The velocities were computed from ultrasonic transducers using two approaches: 1) Detecting the time of the first arrival (with uncertainty of 10 ns), and 2) by time correlation of the recorded signals with the previously recorded referenced signal.

3.3.3 **Results and discussion**

Figure 3-2 shows the ultrasonic waveforms for the Aluminium reference samples obtained by the LDI and piezoelectric transducer as receivers of the wave. We can see that after correction for instrumentation “dead time”, the time of arrival for the P-wave measured by the LDI and transducer equalled with each other. From comparison of signals recorded by the transducer and LDI, which are in phase with each other (only having different polarities), it can be inferred that the ultrasonic transducer measures not a displacement but the rate of the displacement (particle velocity) in the wave.

Figure 3-3 shows ultrasonic waves recorded for the aluminium sample obtained at different voltages and recorded by the LDI (*Figure 3-3a*) and ultrasonic transducer (*Figure 3-3b*). We can see that the particle displacement increased with the applied voltage. At the same time, no change in wave arrival times was recorded in this case.

Figure 3-4 presents the displacement in ultrasonic wave for the PMMA sample recorded by the LDI at four different applied voltages to the source transducer. The amplitude of the displacement increased linearly with the increasing of the voltage, and a slight decrease in arrival times with the increasing of the voltage was observed.

This effect of decreasing arrival time with applied voltage increase was more prominent for the Gosford sandstone sample, presented in *Figure 3-5*.

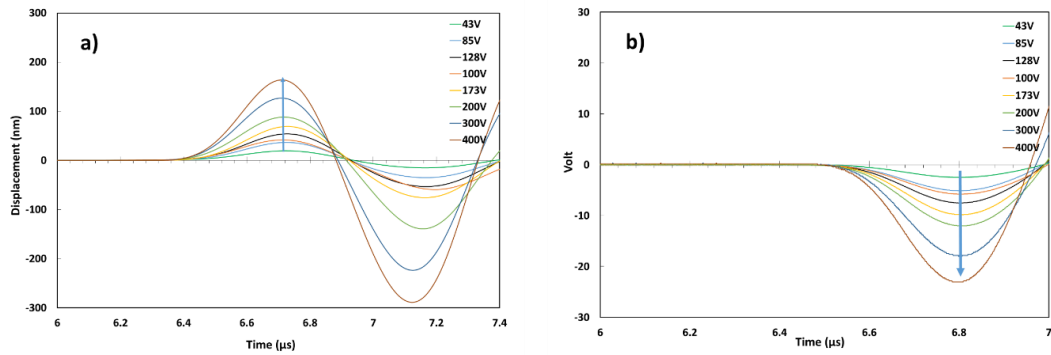


Figure 3-3 (a) Amplitude of displacement in the Aluminium cube measured by LDI and, (b). Signal recorded by ultrasonic transducer, at different voltages applied to the source transducer. No shift in wave arrival is observed.

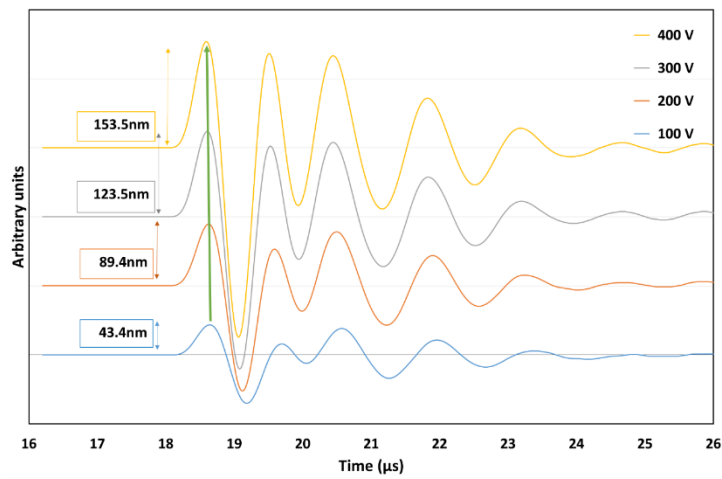


Figure 3-4 Measured displacement of the free surface of PMMA (50 mm thickness) upon arrival of ultrasonic P-wave measured by LDI, at different voltages applied to the source transducer between 100 to 400 V.

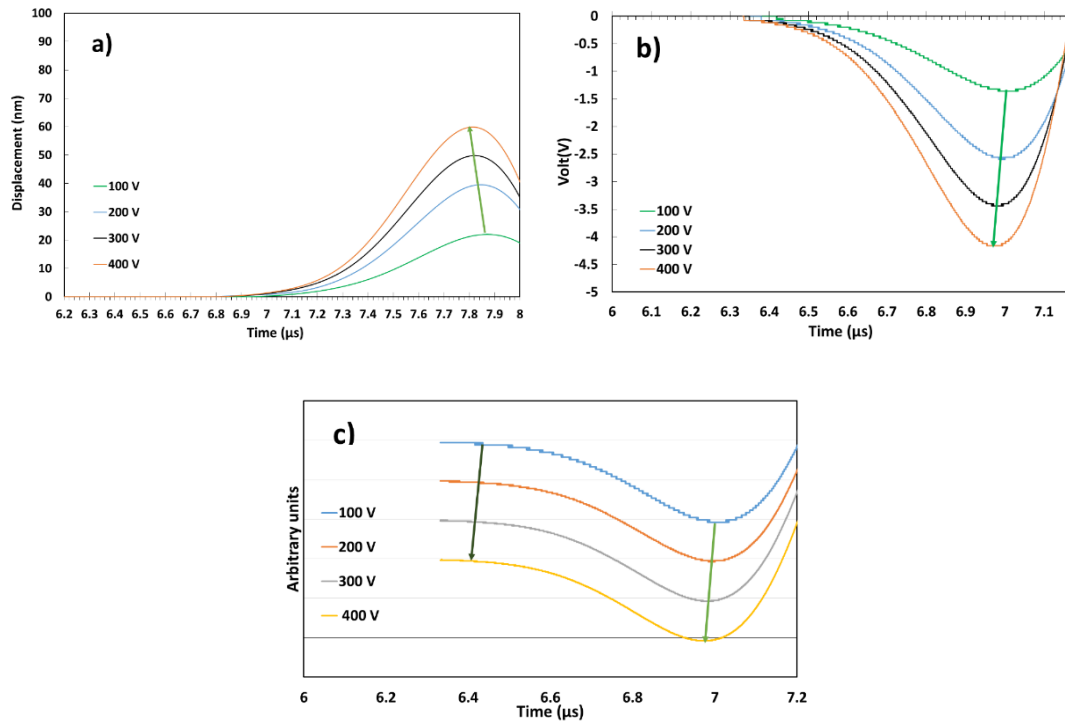


Figure 3-5 Recorded waveforms for the Gosford sandstone for a set of voltages applied to the source transducer: (a). Displacement of the surface upon P wave arrival measured by LDI. (b) Ultrasonic signal recording. Arrows indicate the decrease in travel time with increasing of applied voltage. (c) First arrival signals and the shifts according to input voltages, (signals were modified to have same amplitude for illustration purpose) dark green arrow presents the shift in first arrivals.

After estimations of the strains within ultrasonic waves, the dependence of ultrasonic wave velocity on the strain for all three samples is shown in *Figure 3-6*. No increase in velocity was observed for Aluminium in a wide range of strains (from $3.1 \cdot 10^{-6}$ to $2.6 \cdot 10^{-5}$) inside the wave. For the Gosford sandstone, the P-wave velocity increases by an average of 0.8% with the increasing of the strain inside the wave from $7.0 \cdot 10^{-6}$ to $2.0 \cdot 10^{-5}$. A trend of increasing P-wave velocity of 0.3% is observed for the PMMA sample for a range of strain from $1.6 \cdot 10^{-5}$ to $6.0 \cdot 10^{-5}$. The accuracy of these results was confirmed by triplicating each sequence of measurements and eliminating all possible errors.

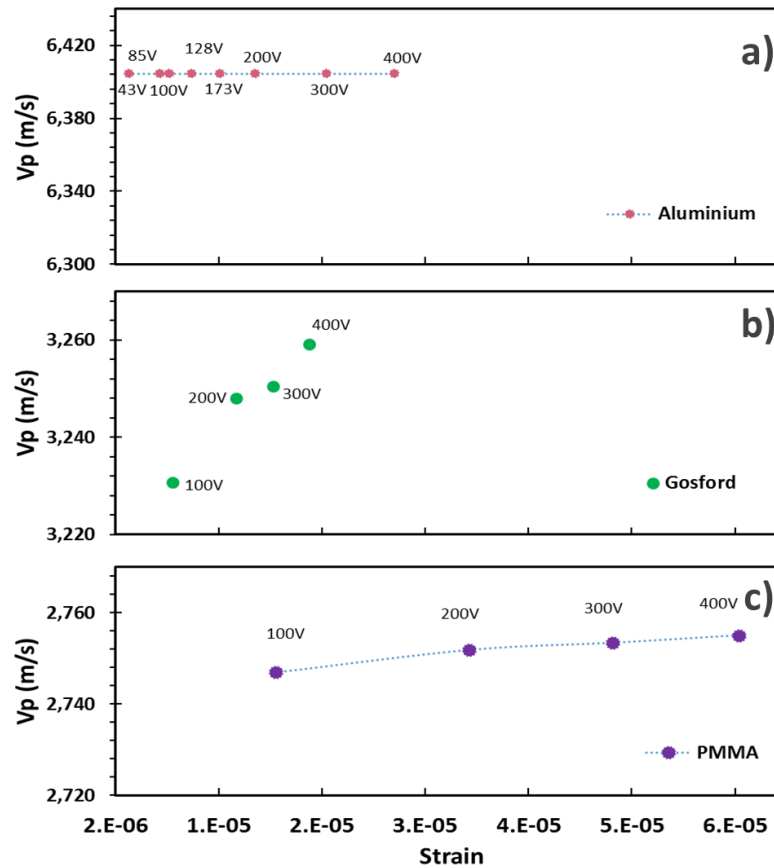


Figure 3-6 P wave velocity dependence on the strain inside ultrasonic wave for Aluminium (a), Gosford sandstone (b) and PMMA (c). Labels inside graphs show the applied voltage to the source transducer.

The experimental results of this study contradict the classic study by Winkler and Nur (1982) describing the amplitude influence on the velocity. One of the reasons for this displacement may be a different experimental procedure and mechanism of transmitting the source pulse as well as the frequency range used. It is also possible that in the earlier experiments the medium experienced a long-term dynamic effect caused by the vibration in a longitudinal resonant experiment. The vibration alters the mechanical behaviour of the material, which leads to the softening of rocks. In next subchapter we will compare the results of Winkler and Nur (1982) with ours.

The results of the current paper are in agreement with the qualitative work by Mashinskii (2005); however in Mashinskii's experiment the strain was not measured directly but was estimated from the transmission coefficient of a piezoelectric transducer and the source voltage. The positive influence of the strain amplitude on P-wave velocity is explained by Mashinskii (2004) as the effect of the contribution of

elasto-plasticity on total deformation. The observations in velocity behaviour as a consequence of strain amplitude can be interpreted as evidence of microplasticity, as microplasticity is amplitude-dependent and can take place even at small strains in elastic regions (Mashinskii, 2005). We should note that no confining pressure was involved in our tests except for a 3.5 kg weight for better coupling. According to Mashinskii (2004), the velocity change due to different amplitudes was more prominent when samples were tested under low confining pressure.

Results of this study confirm the assumption that the elasticity of grain contacts increases with the amplitude of the wave; however, there is a possibility that due to the frictional effect of the grains (Mavko, 1979; Winkler and Nur, 1979; Gordon and Davis, 1968) the attenuation of the P-wave increases as well, which may lead to a decrease in P-wave velocity. These two competitive mechanisms will be investigated in detail in our future works.

The effect of strain amplitude on velocity must be taken into account in all experiments on investigation of the acoustic response of rocks. To be able to compare and quantify results of experimental work it is necessary to provide details of the experimental set-up as much as possible. In particular, the type of equipment and equipment settings, applied voltages, sample size, and the procedure of coupling the transducers with the sample must be documented.

3.4 The effect of wave amplitude on S-wave velocity in porous media: An experimental study by Laser Doppler Interferometry²

3.4.1 Introduction

The relevant data in the literature on amplitude dependence on wave velocities mainly focused on attenuation and wave velocity estimates based on attenuation. Measurement of wave amplitude in dynamic experiments should give increased certainty to experimental studies and may lead to better interpretation of relevant datasets. Thus, to evaluate the effect of velocity dependency on wave amplitude (or strain inside the wave) we designed a special experimental set-up and link the velocity of wave propagation with the strain inside the wave.

3.4.2 Materials and Methods

3.4.2.1 Experimental set up

The ultrasonic equipment for the experiment includes a pair of 1 MHz, videoscanner-type S-wave transducers V153 (Olympus Ltd). Using an internal 15 mm piezoceramic disk housed inside. A pulser/receiver 5077PR (Olympus Ltd) electronic block and a digital, 300 MHz 2.5 GS/s, 4-channel oscilloscope TDS3034C (Tektronix Ltd) are used to apply and record electrical signals. For the coupling between the transducer and the sample surface, we used superglue to attach the transducers to the smooth face of the sample (Nourifard and Lebedev 2018). A square wave electrical pulse of 1 μ s in duration, with the variation of amplitude voltages (43 to 400 V) is applied to the source transducer. This creates a mechanical pulse at the sample's boundary and generates an ultrasonic wave that propagates inside the sample. Then the wave that propagates through the sample reaches the opposite surface of the sample the rate of the displacement of the free surface (i.e. the particle velocity) is measured by a Laser Doppler Interferometry (LDI). The LDI set up consists of a Vibrometer Controller OFV-5000 and Vibrometer Sensor Head OFV-503 (both units are from Polytec Ltd). The LDI measures the rate of displacement of a very small area of the surface (laser

² This subchapter 3.4 is an extended version of the paper "The effect of wave amplitude on S-wave velocity in porous media: An experimental study by Laser Doppler Interferometry"

beam diameter is less than 0.05 mm) and can be considered as a point receiver as this area is much less than the wavelength.

The Laser Interferometry technique has been implemented previously as a receiver for elastic waves in many studies (Dainty 1975; Ennos 1978; Jean Pierre Monchalin 1986; J. P. Monchalin et al. 1989; Scruby and Drain 1990; Jacouot and Fournier 2000; Lebedev et al. 2011; Nourifard and Lebedev 2018; Nourifard et al. 2019). This technique is used to investigate the polarisation of shear waves (Rasolofosaon 1990; Martin and Haupt 1994, Fukushima et al. 2003). Nishizawa et al. (1997) proposed a laboratory method to detect shear wave by Laser Doppler Interferometry (LDI). This method simply measures the surface particle displacement due to the induced wave created by a source transducer. Bayon and Rasolofosaon (1996) tested and demonstrated the credibility of the measurement of particle displacement using this method. Detection of S-wave polarisation was studied by Fukushima et al. (2003). In our study we implemented method of measurement of 3 Components (3C) of waves by LDI described in details in Lebedev et.al. (2011).

Figure 3-7 shows the setup for the current experiment, illustrating the orthogonal and 3C settings of the laser beam. All the LDI parts, the sample and the attached transducer are placed and fixed on a noise-cancelling platform in a special laser room to avoid any environmental vibration. The laser beam angle with a horizontal plane was fixed at 37 degrees for each sampling point. The minimum of three independent measurement for each point is required to reconstruct the 3C therefore by rotation of the sample with precise 120 degrees between each recording 3 wavelets (X_1, X_2 and X_3) registered for the matrix transformation. The displacement vectors then converted to the orthogonal coordinate system (x,y and z).

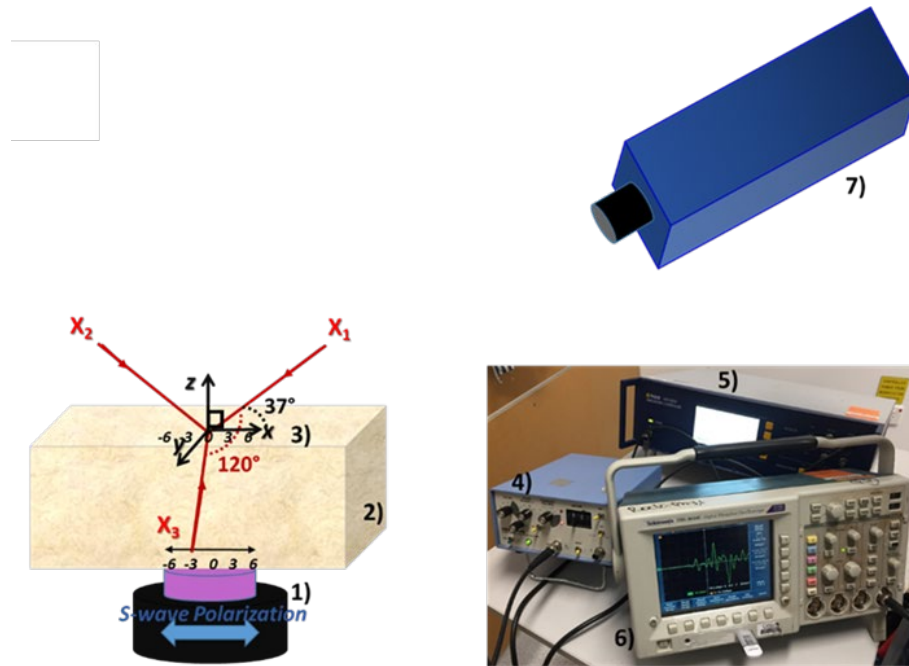


Figure 3-7. (a) Experimental setup. 1: S-wave transducer (source of ultrasonic waves), 2: Sample, 3: Survey line on the top of the sample where the laser beam is emitted and scattered back, 4: Pulse generator, 5: Vibrometer Controller OFV-5000, 6: Oscilloscope, 7: Laser Doppler interferometer (LDI).

3.4.2.2 Sample preparation and experimental procedure

The Bentheimer outcrop sandstone with 24% porosity and less than 1% of elastic anisotropy (i.e. difference in ultrasonic wave velocities measured in different directions) has been used for this study. Both faces of the medium must be parallel and smooth for the LDI and acoustic tests. For granular material it is important to make surface smooth thus the surface pores on the sampling points should be locally filled for the best coupling and to create a smooth plane surface for the laser beam. To make the sandstone surface smooth a thin layer of superglue was added to the sampling line and repeated to create the desirable smoothness. The survey line has been marked for divisions of 3 mm on both samples and the transmitted transducer. The source transducer was attached on the bottom of the sample using superglue. The polarisation of the S-wave transducer is aligned with the sampling line on the top surface of the sample.

The experimental procedure is as follows: (1) Sample preparation, locating the precise sampling points the same length as the diameter of the piezoelectric disk inside the bottom transducer. The points are marked on the top face of the samples and free surface of the transducer to an accuracy of 0.5 mm; (2) Measurement of the time delay

(deadtime) in the electronics by direct contact of the pair of S-wave transducers using standard acoustic equipment; (3) Gluing the sample at the located centre point at the bottom of the sample with aligned polarisation with superglue for the best possible coupling; (4) Fixing the sample and bottom source transducer on the rotational platform placed on the noise cancelling desk. The laser beam incident angle remains the same for all the measurements in all directions. Using the rotational bottom platform allows us to record three individual directions of displacement for each sampling point; (5) Recording waveforms at different input voltages (43 V to 400 V) inserting from the bottom S-transducer on each survey point. Each point measured in three independent directions (each 120 degrees apart) to extract three components. The displacement will then be calculated for each point; (6) The second pair of the S-transducer is attached to the top face by superglue on the same sampling points as its diameter. The polarisation direction of the second S-wave transducer is the same as the source bottom S-wave transducer and locates on the same centre point where the laser has already measured the displacement on the survey line (the large diameter of the transducers and chosen dimensions of the samples allow us to measure the group velocity, which is equal to a phase velocity in this study); (7) The same voltages are applied once again to record the velocities and wave forms from 43 V to 400 V; (8) the transducers are removed from the sample by immersing into acetone for 24 h. The same transducers were used for all the measurements on all samples.

3.4.3 Results and Discussion

3.4.3.1 The displacement

To simultaneously measure displacement along 3 orthogonal axes (x, y and z), LDI equipment was used. The generated S-waves at frequency of 1 MHz have wavelengths of 4.53 mm, and 7.2 mm for Aluminium and Bentheimer sandstone respectively. A wave generated by piezoelectric transducer attenuates during propagation through the sample. Thus the amplitude (strain) inside the wave is not the same, however dry sandstone samples have a low attenuation (i.e. high quality factor Q) and aluminium has a negligible attenuation. For our experimental conditions in a worst case scenario, the amplitude of an ultrasonic wave may attenuate no more than 50%. On the other hand, we measure the displacement on the surface. Because of the wave reflection from the free boundary such displacement is approximately double of that very close

to the surface. In this paper our focus is on illustrating the dependency of velocity to the strain inside the wave thus we may take a strain measured on the surface as a reference strain.

LDI measures the rate of displacement of the surface; thus, to obtain the displacement and to calculate the strain in the wave the recorded signal has to be integrated as a function of time (Lebedev et al. 2011). The strain (ϵ) inside the wave is defined as Eq 3.2.

It should be mentioned that since the direction of S-wave polarisation is along the x direction, the displacement along this axis is considered for the calculations of the strain.

The displacement of the S-wave transducer was measured directly in three independent directions – X_1 , X_2 and X_3 – then transformed to the Cartesian coordinate system x , y and z (Figure 3-7 and Figure 3-8). Particle displacement due to shear wave occurs in horizontal direction (x axis) and displacement due to P wave occurs in vertical direction (z axis). The recordings of 3C on the free surface of the S-wave transducer were measured on the sampling line that each point aligned with S-wave polarisation. After characterisation of the S-wave transducer the transducer was attached to the bottom of the sample using the same polarisation orientation and the same sampling set-up was used for the 3C measurement source on the media.

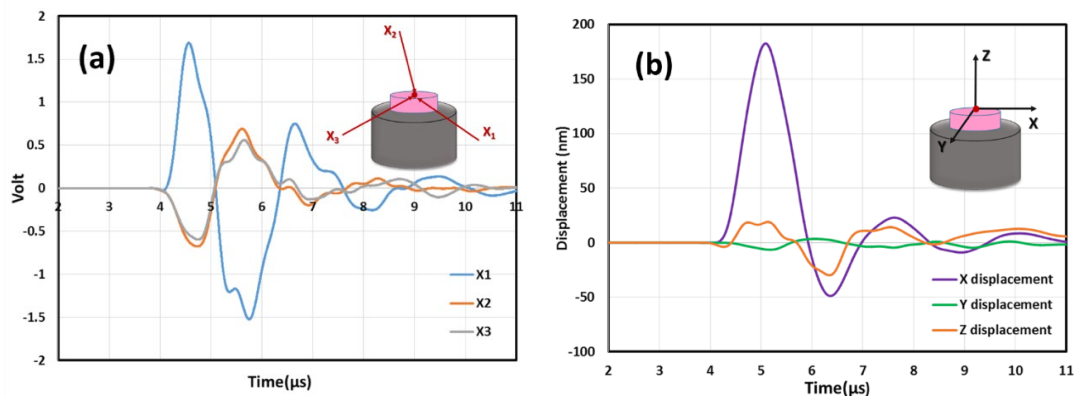


Figure 3-8 (a) Raw waveform of S-transducer on centre point in three directions before matrix transformation by LDI on 400V, (b) Displacement after matrix transformation in x , y and z directions of S-transducer on centre point by LDI on 400V.

The displacement of the particles on the surface of the samples were measured using the same procedure as the free surface of the transducer at three different directions on the rotational platform. Displacement was then calculated in x and z directions. *Figure 3-9* illustrates the displacement on the survey line on the Bentheimer sandstone and the transducer in the X direction at 400V applied voltage.

The wave propagating through the sample loses energy and is affected by possible non-homogenous areas inside the rock; thus, the displacement measured at different points on the surface is not constant. However, we can see that the particle displacement on the surface follows the same pattern as the particle displacement on the transducer. The waveforms of particle displacement of the Bentheimer sandstone measured at different applied voltages are plotted in *Figure 3-10*. Displacement is proportional to the voltage applied to the transducer.

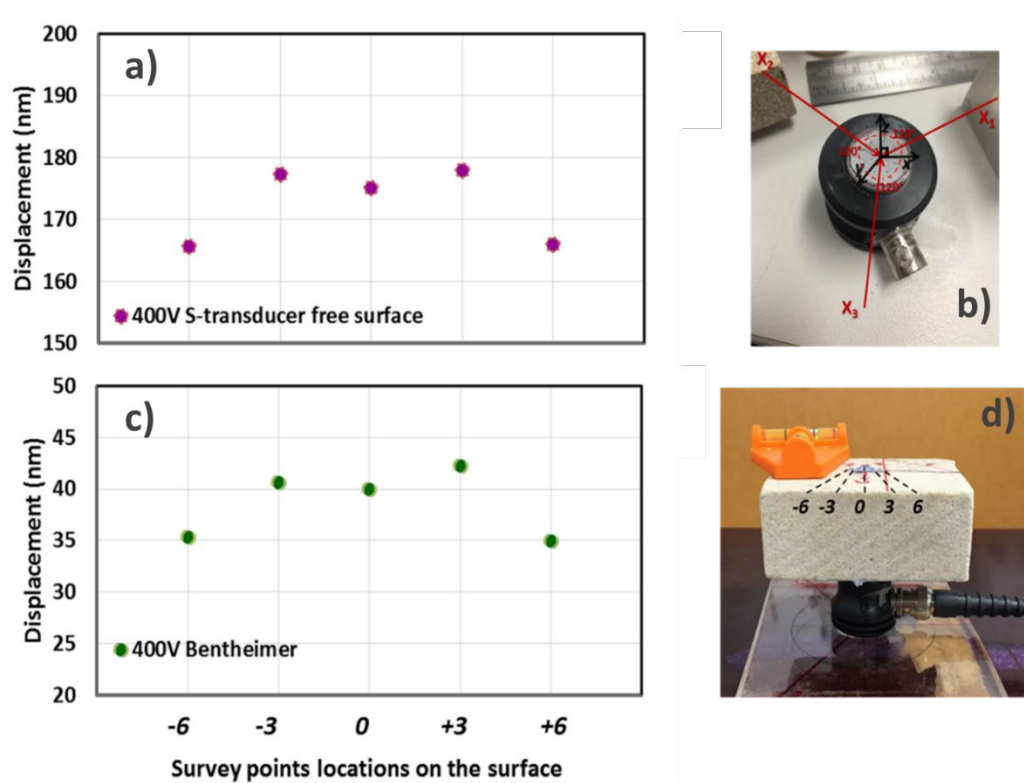


Figure 3-9 (a) Horizontal (x-axis) displacement of particles on the surface of the S-wave transducer (b) , (c) Horizontal displacement on the surface particle of the sample (d) Bentheimer sandstone (32 mm thickness) on the walk-away line (3 mm divisions).

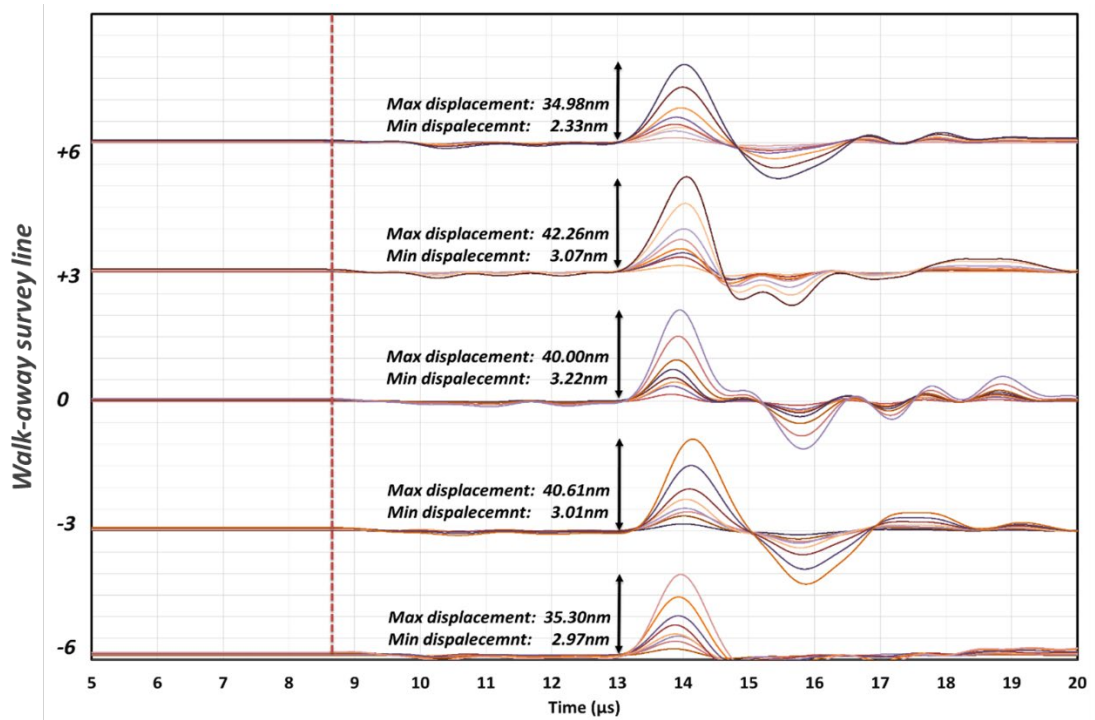


Figure 3-10 Horizontal displacement of the particles on the surface of Bentheimer sandstone in horizontal direction (x-axis) in the walk-away experiment and at the range of applied voltages from 43 V to 400 V. Numbers show the maximum particle displacement for 400 V and minimum particle displacement for 43 V respectively.

Figure 3-11 shows the displacement on the centre point of the aluminium surface on the horizontal X-axis obtained at different voltages recorded by the LDI. As we can see from this figure the recording signals are well aligned and no shift in time is observed.

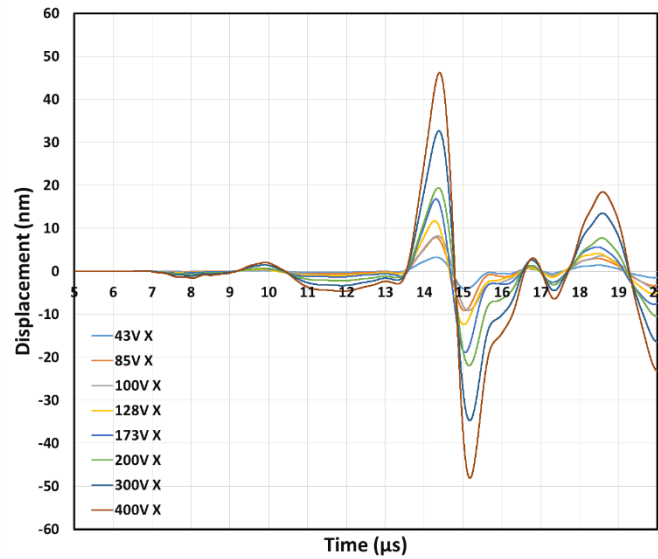


Figure 3-11 Displacement of aluminium surface particles in horizontal x direction measured by LDI 3C in all applied voltages

3.4.3.2 The velocity

Velocities measured by LDI are very close to that measured by a pair of ultrasonic transducers, however in this paper we are comparing the results using “standard” ultrasonic set-up. P-wave velocity was measured by a pair of P-wave transducers (1 MHz) and S-wave velocity was measured by a pair of S-wave transducers (1 MHz) (transmitter and receiver time of flight technique). The first arrivals for P- and S-waves were detected by correlation of the first peak-amplitude on original and normalised amplitude wavelets to pick the first arrivals. *Figure 3-12* and *Figure 3-13* show the recorded and normalised waveforms for Bentheimer sandstone and *Figure 3-14* shows the waveforms in a case of aluminium sample. All waveforms were corrected by a time delays in the measurement system. The amplitude effect on wave velocity was measured at variation voltages from 43 V to 400 V. It was observed that P-wave first arrival has a tendency to decrease by applying higher voltages resulting in increased P-wave velocities. This effect is even observable by P reflection peaks (*Figure 3-12*). P-wave velocity measured by P transducer confirms previous study on different samples (Nourifard and Lebedev 2018; Mashinskii E.I. 1999; E. I. Mashinskii 2004) and shows increase of P-wave velocity by 0.63% in Bentheimer sandstone. P-wave dependency to strain amplitude results for Bentheimer sandstone are qualitatively

similar to the results for Gosford sandstone (Nourifard & Lebedev 2018) where compressional velocity is slightly increased by up to 1% by increasing the applied voltage. However, S-wave velocities decreased by ~5% with an increase in applied voltage (Figure 3-15). In the aluminium sample S-wave velocities remained constant at all applied voltages (Figure 3-14).

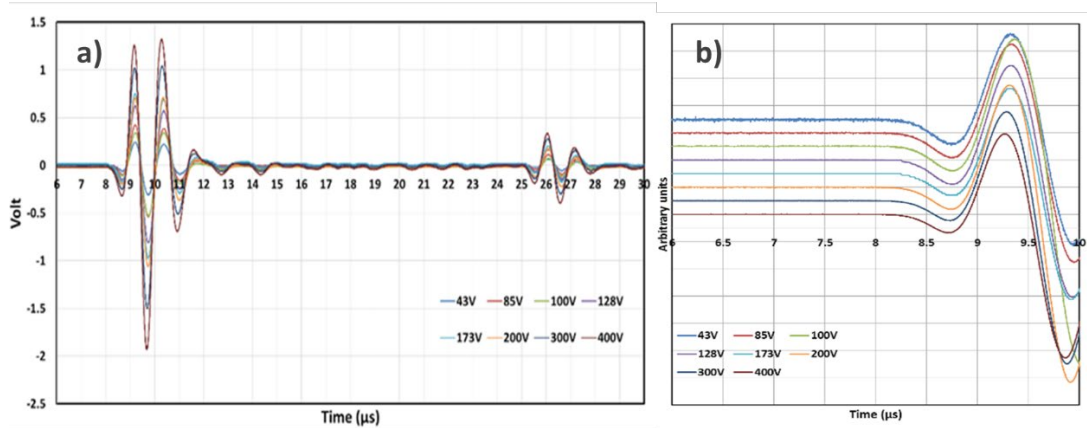


Figure 3-12 P-wave full wavelets measured by P-transducers of Bentheimer sandstone original (a) and normalised amplitude on P first break and first peak (b) at all applied voltages.

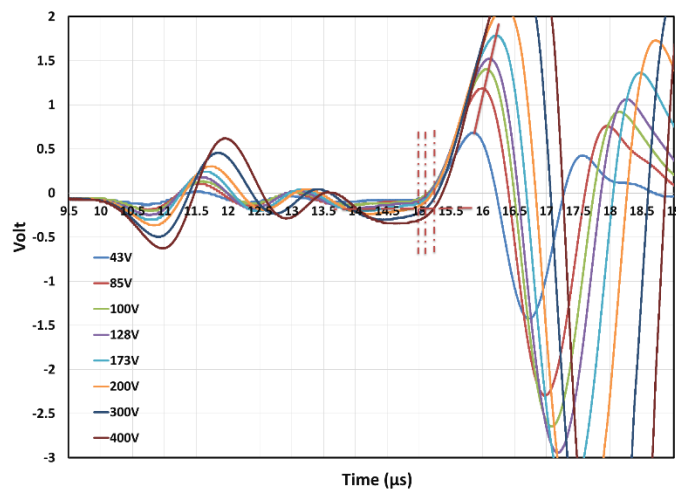


Figure 3-13 S-wave full wavelets measured by S-transducers of Bentheimer sandstone original, (the full wavelet saturation effect at peaks corresponding to 300 and 400 Volts graphs is due to measurement settings chosen to have the same accuracy).

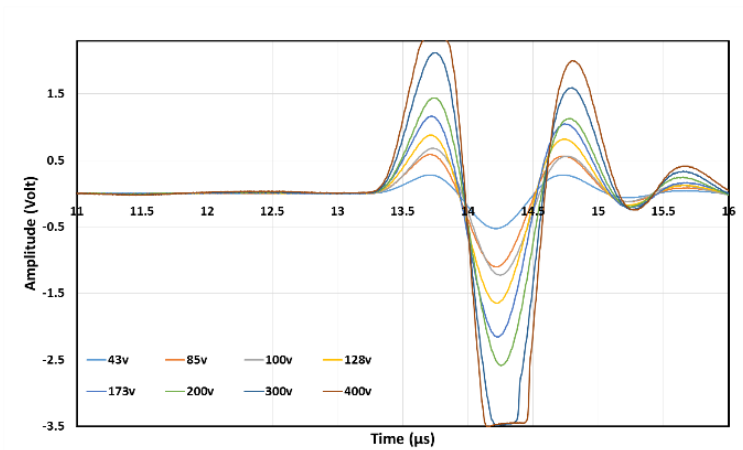


Figure 3-14 S first arrival measured by S-wave transducer for Aluminium sample at all applied voltages (the full wavelet saturation effect at peaks corresponding to 300 and 400 graphs is due to measurement settings chosen to have the same accuracy).

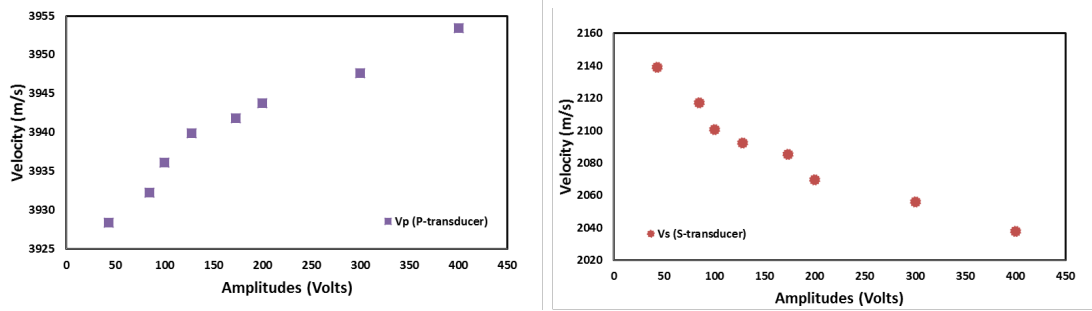


Figure 3-15 Velocities of Bentheimer sandstone on the first peaks measured by P- and S-wave transducers at different applied voltages to the transducers shows 0.63% increase for P velocity and 4.75% decrease for S wave velocity

By measuring the strain inside the waves using Eq. 2.1, the dependency of the ultrasonic S-wave velocity on the strain for Bentheimer sandstone and aluminium is shown in *Figure 3-16* for the sample's centre point. No increase in P- and S-wave velocities was observed for aluminium in the range of strains (from $(9.74) \cdot 10^{-7}$ to $(2.1) \cdot 10^{-5}$) inside the wave. For Bentheimer sandstone, S-wave velocity decreases by an average of 4.75% with the increasing of the strain inside the wave from $(3.6) \cdot 10^{-7}$ to $(5.7) \cdot 10^{-6}$. No confining pressure was applied to the samples in this test; according to Mashinskii (2004), the velocity change due to different amplitudes was more prominent when a sample is tested under low confining pressure and we observed that the S-wave is more sensitive than the P-wave.

The results of this study confirm the assumption that the attenuation of the S-wave increases with an increase in the amplitude of wave, which may lead to a decrease in

S-wave velocity. Results of this and previous studies (Mashinskii 2004, Nourifard & Lebedev 2018) show that the P-wave velocity increases with increasing amplitude; however, such sensitivity is much smaller than for S-waves. Dynamic Young's modulus can be obtained from P- and S-wave velocities (Mavko *et al.* 2009). As:

$$E = \rho V_s^2 (3V_p^2 - 4V_s^2) / (V_p^2 - V_s^2) \quad (\text{Eq. 3.3})$$

Where V_p and V_s are the velocities of P and S ultrasonic waves respectively, and ρ is the density of the sample.

The difference between the rate of change of P and S wave velocities impacts on the dynamic Young's modulus. In this experiment, the P-wave velocity increases by 0.6% but the S-wave velocity decreases by about 5%; thus, the contribution of the S wave is dominant. The calculated dynamic Young's modulus as a function of strain in the S wave measured in the centre point is shown in *Figure 3-17*. This result is in agreement with studies by Winkler and Nur (1979, 1982) in which extensional wave velocity ($V_E = \sqrt{E/\rho}$) decreases with the increasing of the amplitude: i.e., with an increasing of the strain.

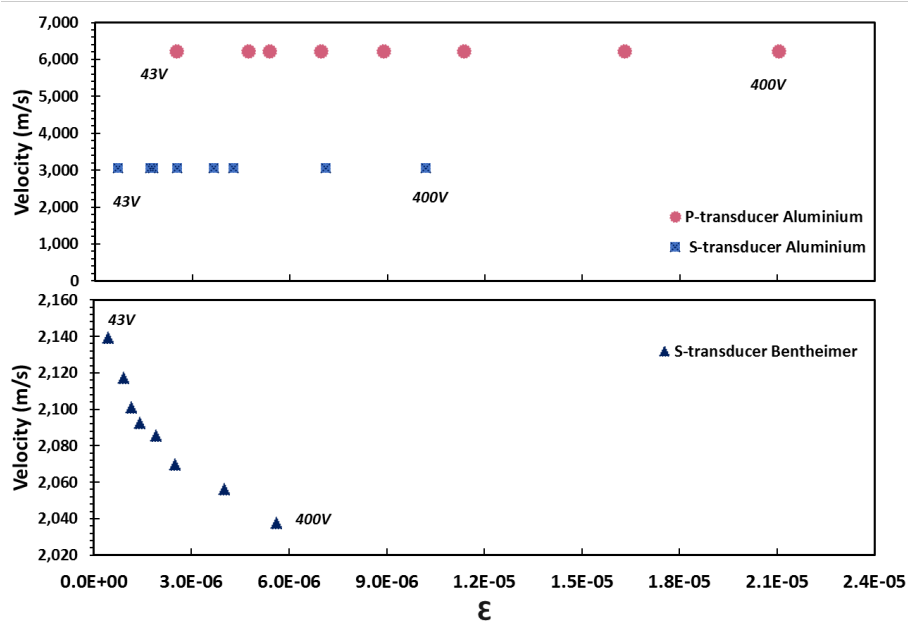


Figure 3-16 (top) The dependency of P and S- waves velocities on strain amplitude measured by P and S transducers and LDI in x direction in aluminium; (bottom) in Bentheimer sandstone.

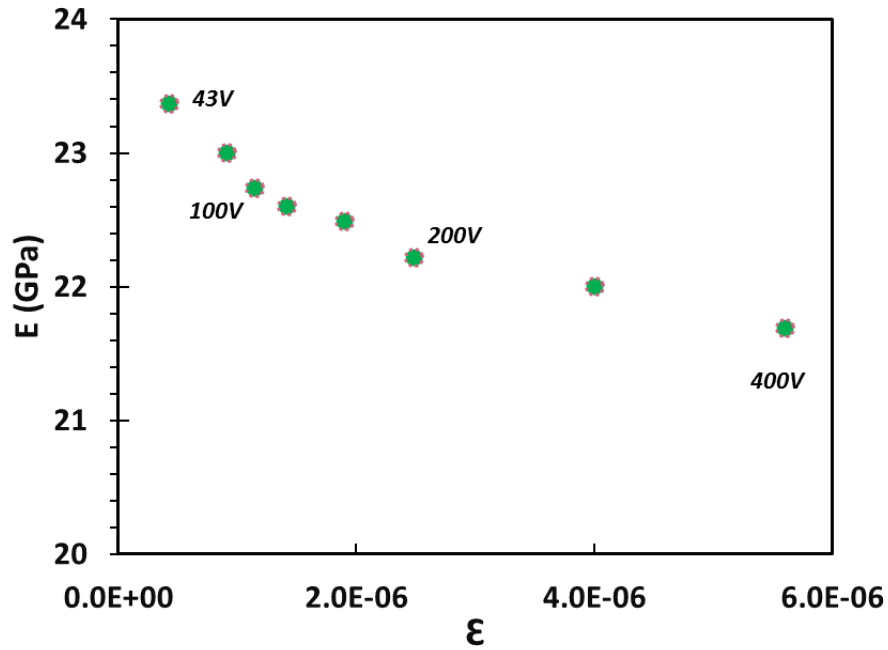


Figure 3-17 The dynamic Young's modulus dependence on strain amplitude measured by P and S transducers and LDI for Bentheimer sandstone

3.5 Conclusion

To quantify the effects of amplitude on the longitudinal and transverse velocities in porous media a series of experiments implementing Laser Doppler Interferometry (LDI) and Ultrasonic time of flight method were conducted. Direct and simultaneous measurements of both P- and S-wave velocities as well as the strain inside the wave were performed. The main results of this study are: 1) Based on the experiments with a typical rock sample used in laboratories, the strain in ultrasonic waves ranged from $3.6 \cdot 10^{-7}$ to $6 \cdot 10^{-5}$; 2) for unconfined Bentheimer sandstone we observed the effect of the strain amplitude on the wave velocities for both P- and S-waves; namely, up to a 5% decrease for S-wave velocity and less than a 1% increase for P-wave velocity with increasing strain; for Gosford sandstone the effect of strain amplitude was recorded as a 0.8% increase for P-wave velocity; 3) the dependency of S-wave velocity on strain amplitude is more prominent than the dependency of P-wave velocity and, as a result, the dynamic elastic modulus decreases as the strain increases. The effects of the amplitude of ultrasonic waves on wave velocities must be taken into account in interpretations of experimental rock physics results.

3.6 References to Chapter Three

- Abeele, K.V. D., Johnson, P. A., Guyer, R. A. & McCall, K. R. 1997. On the Quasi-Analytic Treatment of Hysteretic Nonlinear Response in Elastic Wave Propagation. *The Journal of the Acoustical Society of America* 101 (4): 1885–98. <https://doi.org/10.1121/1.418198>.
- Aydin, A. 2014. Upgraded ISRM suggested method for determining sound velocity by ultrasonic pulse transmission technique. *Rock Mechanics and Rock Engineering* 47, 255–259.
- Bayo, A., Rasolofosaon, P. N. J. 1996. Three-Component Recording of Ultrasonic Transient Vibration by Optical Heterodyne Interferometry. Multicomponent Recording, and B Y Speckle. 99 (2): 954–61. <https://doi.org/10.1121/1.414623>.
- Cate, J. A. T., & Shankland, T.J. 1996. Slow Dynamics in the Nonlinear Elastic Response of Berea Sandstone. *Geophysical Research Letters* 23 (21): 3019. <https://doi.org/10.1029/96GL02884>.
- Cook, N. G. W. & Hodgson, K. 1965. Some Detailed Stress-Strain Curves for Rock. *Journal of Geophysical Research* 70 (12): 2883. <https://doi.org/10.1029/JZ070i012p02883>.
- Dainty, J.C. 1975. Laser Speckle and Related Phenomena. Vol. 9. Topics in Applied Physics. Berlin, Heidelberg: Springer Berlin Heidelberg. <https://doi.org/10.1007/BFb0111434>.
- Ennos, A.E. 1978. IV Speckle Interferometry. *Progress in Optics* 16 (January): 233–88. [https://doi.org/10.1016/S0079-6638\(08\)70073-8](https://doi.org/10.1016/S0079-6638(08)70073-8).
- Fukushima, Y., Nishizawa, O., Sato, H. & Ohtake, M. 2003. Laboratory Study on Scattering Characteristics of Shear Waves in Rock Samples. *Bull Seismol Soc Am* 93 (1): 253–63.
- Jacouot, P. & Fournier, J. M. 2000. Interferometry in Speckl Light - Theory and Applications.
- Johnson, P. A., Zinszner, B. & Rasolofosoan, P. N. J. 1996. Resonance and Elastic Nonlinear Phenomena in Rock. 101 (96).

- Johnston, D. H. & Toksov, M. N. 1980. Thermal Cracking and Amplitude Dependent Attenuation. *Journal of Geophysical Research* 85 (B2): 937–42. <https://doi.org/10.1029/JB085iB02p00937>.
- Lebedev, M., Bóna, A., Pevzner, R. & Gurevich, B. 2011. Elastic Anisotropy Estimation from Laboratory Measurements of Velocity and Polarization of Quasi-P-Waves Using Laser Interferometry. *Geophysics* 76 (3): WA83-WA89. <https://doi.org/10.1190/1.3569110>.
- Martin, R.J. & Haupt, R. W. 1994. Static and Dynamic Elastic Moduli in Granite: The Effect of Strain Amplitude, in *Rock Mechanics: Models and Measurements Challenges from Industry*. *Rock Mechanics, Nelson & Laubach (Eds)*, 473–80.
- Mashinskii, E. I. 2004. Variants of the Strain-Amplitude Dependence of Elastic Wave Velocities in Rocks under Pressure. *Journal of Geophysics and Engineering* 1 (4): 295–306. <https://doi.org/10.1088/1742-2132/1/4/008>.
- Mashinskii, E. I. 2008. Amplitude-Frequency Dependencies of Wave Attenuation in Single-Crystal Quartz: Experimental Study. *Journal of Geophysical Research: Solid Earth* 113 (11): 1–11. <https://doi.org/10.1029/2008JB005719>.
- Mashinskii, E. I. & D'yakov, G.N. 1999. Amplitude-Dependent Attenuation of Acoustic Signals in Rocks. *RAN. Ser. Fizika Zemli* 11: 63–67.
- Mashinskii, E. I. 2001. Nonlinearity of a Quasi-Static Stress-Strain Relation: The Dependence on the Level of Mechanical Energy. *Geofizika* 2: 37–41.
- Mashinsky, E. I. 2003. Differences between Static and Dynamic Elastic Moduli of Rocks: Physical Causes. *Russian Geology and Geophysics* 44 (9): 953–59.
- Mashinsky, E. I. 1994. Quasi-Micro-Plasticity Processes and Nonlinear Seismicity. *Phys. Solid Earth* 30: 97–102.
- Mavko, G., Mukerji, T. & Dvorkin, J. 2009. *The Rock Physics Handbook*. Cambridge: Cambridge University Press. <https://doi.org/10.1017/CBO9780511626753>.
- Mavko, G. 1979. Friction Attenuation: An Inherent Amplitude Dependence. *Geophysical Research Letters* 84: 4769–75.

<https://doi.org/10.1029/JB084iB09p04769>.

McCall, K. R. & Guyer, R. A. 1994. Equation of State and Wave Propagation in Hysteretic Nonlinear Elastic Materials. *Geophysical Research Letters* 12 (4).

Monchalín, J. P., Aussel, J. D., Héon, R., Jen, C. K., Boudreault, A. & Bernier, R. 1989. Measurement of In-Plane and out-of-Plane Ultrasonic Displacements by Optical Heterodyne Interferometry. *Journal of Nondestructive Evaluation* 8 (2): 121–33. <https://doi.org/10.1007/BF00565636>.

Monchalín, J. P. 1986. Optical Detection of Ultrasound. *IEEE Transactions on Ultrasonics, Ferroelectrics, and Frequency Control* 33 (5): 485–99. <https://doi.org/10.1109/T-UFFC.1986.26860>.

Nishizawa, O., Satoh, T., Lei, X. & Kuwahara, Y. 1997. Laboratory Studies of Seismic Wave Propagation in Inhomogeneous Media Using a Laser Doppler Vibrometer. *Bulletin of the Seismological Society of America* 87 (4): 809–23. <http://www.bssaonline.org/content/87/4/809.short>.

Nourifard, N. & Lebedev, M. 2018. Research Note: The Effect of Strain Amplitude Produced by Ultrasonic Waves on Its Velocity. *Geophysical Prospecting*, 1–8. <https://doi.org/10.1111/1365-2478.12674>.

Nourifard, N., Mashinskii, E., Lebedev, M. 2019. The effect of wave amplitude on S-wave velocity in porous media: An experimental study by Laser Doppler Interferometry: Exploration Geophysics. DOI: 10.1080/08123985.2019.1667228.

Pouet, B. & Rasolofosaon, P. N. J. 1990. Seismic Physical Modeling Using Laser Ultrasonics. *60th Ann. Internat. Mtg*, no. January: 841–44. <https://doi.org/10.1190/1.1890357>.

Scruby, C. B. & Drain, L. E. 1990. Laser Ultrasonics : Techniques and Applications. A. Hilger. <https://www.crcpress.com/Laser-Ultrasonics-Techniques-and-Applications/Scruby-Drain/p/book/9780750300506>.

Stewart, R. S., Toksoz, M. N. & Timur, A. 1983. Strain Dependent Attenuation: Observations and a Proposed Mechanism. *Journal of Geophysical Research* 88 (B1): 546–54. <https://doi.org/10.1029/JB088iB01p00546>.

Tutuncu, A. N., Augusto, L. P., Alvin, R. G. & Sharma, M.M. 1998. Nonlinear Viscoelastic Behavior of Sedimentary Rocks, Part I: Effect of Frequency and Strain Amplitude. *Geophysics* 63 (1): 184–94. <https://doi.org/10.1190/1.1444311>.

Winkler, K. W. & Nur, A. 1982. Seismic Attenuation: Effects of Pore Fluids and Frictional Sliding. *Geophysics* 47 (1): 1–15. <http://link.aip.org/link/?GPY/47/1/1>.

Winkler, K. & Nur, A. 1979. Pore Fluids and Seismic Attenuation in Rocks. *Geophysical Research Letters* 6 (1): 1–4. <https://doi.org/10.1029/GL006i001p00001>.

Zinszner, B., Johnson, P. A. & Rasolofosaon, P. N. J. 1997. Influence of Change in Physical State on Elastic Nonlinear Response in Rock: Significance of Effective Pressure and Water Saturation. *Geophysical Research Letters* 102 (96): 8105–20.

Chapter 4 The effects of stress and fluid on the anisotropy of reservoir rock: case study of a sandstone from a Harvey-3 CCS site

4.1 Foreword

In this chapter we overview the effect of stress and saturation on the anisotropy parameters for a typical reservoir sandstone: Harvey-3. The results of this chapter has been accepted for publication in *Exploration Geophysics*.

4.2 Abstract

In rock physics studies the main objective of the determination of P- and S-wave velocities are to obtain the elastic constants and anisotropy parameters. This method is standardised in American Society for Testing and Materials (ASTM) standard D2845-95. The most challenging and important part of these experiments is picking the first arrivals correctly and consistently. A sharp, clean first arrival is not always possible, especially when testing dry, porous sandstones at low pressures. The signal transmitted through such samples is weak due to a high damping effect, and picking the first break introduces uncertainties. The Harvey sandstone is a sample type with high porosity and, therefore, some degree of anisotropy is expected. In order to study the anisotropy parameters of Harvey-3 sandstones, three core sub plugs collected in directions of horizontal, vertical and diagonal, were experimentally investigated. Applying high hydrostatic stress ensures sufficient compaction to record the elastic waves of the matrix of the rock, with the elimination of pores and gaps inside the sample. The laboratory measurements on three different samples at three different directions with regards to the base deposition system enabled us to calculate the anisotropy parameters using standard acoustic equipment while applying stress. We concluded that Harvey-3 poses a more complex symmetry axis of anisotropy, and no sign of low-grade anisotropy was observed through the experimental data. To study the anisotropy degree of the Harvey-3 sandstone, a pressure cell, pore fluid injection pump, and ultrasonic system (consisting of P- and S-wave transducers, oscilloscope and pulser) were used to record the elastic waves passing through the samples. Specimens were gathered from the mine site in three directions. The specimens were fully saturated inside the pressure cell using vacuum injection for best possible comparison of dry and

saturated status. The results confirmed that the sample is far from weak anisotropy and possesses more axes of symmetries than simple layering anisotropy due to the pore orientation and distribution in the matrix of the background rock. The study also confirms that the anisotropy degree decreases under full compaction and full saturation, and Harvey-3 anisotropy becomes elliptical when it's fully saturated. Large, stress-dependent changes in the ultrasonic velocities for porous media were observed in this experimental study, which confirms the usefulness of such studies in examining the inner structure change process.

4.3 Introduction

The velocities of compressional and shear waves are related to the elastic properties and internal structure of the media. Hicks and Berry (1956) summarised the factors affecting the velocities of the rocks into four categories: 1) The inner structure, including porosity, density of grains, elastic constant of grains, cementation; 2) the fluid inside the pores with regards to the density, pressure and compressibility; 3) the temperature condition of the sample; and 4) the in-situ stress condition and overburden pressure. In the field, the velocity increases logarithmically with increasing of the depth (Brandt 1955) and, while the pressure increases the velocity, the corresponding higher temperature due to the depth reduces the velocity (Kassab and Weller 2015).

Pore spaces decrease the bulk density and these gaps between the grains lead to less rigidity and produce compliant framework structure sensitive to effective pressure variation. This decreases the velocity of compressional and shear waves. The structure of the pores governs the Shear and Bulk moduli (Gregory 1976). P-wave velocity in saturated porous media is generally higher than dry media; however, this statement does not apply for media possessing low bulk compressibility. The S-wave velocity of saturated porous media is always less than dry media due to the assumption that in full saturation the micro cracks are filled and gaps can be considered as negligible (Biot 1956). Experimental studies involving full saturation of porous material registered faster P-wave velocity compared to dry mode (Boulanouar et al. 2013). Kassab and Weller (2015) reported that S-wave velocity reduces with increasing water saturation; however, once it reaches 70–75% of water saturation the increasing of this value begins.

Vernik and Nur (1992) summarised the major factors responsible for seismic anisotropy into three categories as: a) Micro lamination or interlayering of the rock with the layers at dimensions much smaller than the wavelengths of the propagating wave (Riznichenko 1949; Postma 1955; Backus 1962); b) the alignment of the mineral orientation composing the rock framework (Jones and Nur 1982; Vernik et al. 1984); and c) stress-induced micro-cracks and micro-fractures with preferred alignment (Nur and Simmons 1969; Hudson 1981; Crampin 1984).

There is a lack of detailed experimental study in the literature on the effect of saturation and stress on the physical properties of medium-grained reservoir sandstones. In particular, experimental studies where anisotropy is calculated by direct measurement of P- and S-waves at dry and saturated conditions on their original orientations have not been reported in detail. Our experimental results illustrate two major features of anisotropy for the Harvey-3 sandstone based on induced stress and the effect of pore density on the degree of anisotropy. We observed that the pores and micro-cracks play a major role in anisotropy grade and, as we expected, by filling or closing those gaps the rock matrix becomes more isotropic.

This chapter studies the effect of stress and saturation on the grade of anisotropy in the Harvey-3 sandstone samples. Further, it will investigate whether the media possess weak anisotropy via the experimental measurement of velocities of the sample in three directions at dry and saturated status.

4.3.1 Literature review

The realistic wave propagation model is crucial for inversion and 3D seismic imaging. Such models are used for CO₂ sequestration, groundwater investigations and to explore hydrocarbon reservoirs (Bording and Lines 1997; Gao et al. 2005; Li et al. 2006). Most rock physics models are based on an assumption of isotropy for geo-materials. This assumption was later challenged by numerous seismic anisotropy observations that indicate the measured rock elastic properties at a given point vary with azimuth (Nur and Simmons 1969; Thomsen 1999; Hornby et al. 2003). The misuse of the isotropy assumption for geo-material often compromises the accuracy of the seismic imaging velocity models, geophysical inversions, microseismic event locations and leads to incorrect interpretations (Tsvankin et al. 2010; Shragge and Lumley 2012). To validate

rock physical models, it is necessary to have sufficient laboratory data on the behaviour of the material under appropriate pressure and fluid saturation conditions to accurately examine the assumptions accordingly.

Laboratory measurements produce the data needed to formulate a model where the most controlled stress application can be performed. Anisotropy is usually estimated by the measurement of compressional and shear velocities.

For the analysis of anisotropy of a compressional wave a sufficient number of angles need to be measured to recover an azimuth dependent anisotropy signature (Grechka and Tsvankin 1999), precise travel times are needed (Li 1999; Wang and Li 2006), and the amplitudes need to be considered (Rudger 1998; Vavrycuk and Psencik 1998). Different combinations of applied stress have been studied in the literature. Uniaxial stress was performed in Nur and Simmons (1969) experimental study to evaluate anisotropy. Their study shows that anisotropy increases as a consequence of non-uniform application of principal stress. Bonner (1974) studied stress-related anisotropy in the lab on Westerley Granite where a variation of velocities was observed via the change of orientation due to surrounding stresses. Yin (1992) studied Granite, Shale, Berea, Massillon Sandstone and Siltstone at variety of stress conditions. The results of this study illustrate that hard rocks display transverse isotropy by nature while soft rocks show stress-induced anisotropy to higher grades once subjected to increasing stress. This happens because of the closure of the cracks and pore spaces in the direction of compressive stress. Stress-induced anisotropy has motivated many theoretical studies to formulate and model such dependency over several decades (Nur 1971; Gibson and Toksz 1989; Sayers et al. 1990; Gurevich et al. 2011). The majority of the models in the literature have the following assumptions: 1) Low-crack concentration, and 2) angular distribution of penny-shaped cracks in the rock matrix. In our experimental study we used generalised theoretical models for soft rocks under an intermediate stress regime.

4.4 Elastic anisotropy review

A linearly elastic material is defined as one in which each component of stress σ_{ij} is linearly dependent upon every component of strain ϵ_{kl} (Nye 1957). In other words, stress and strain tensors (σ_{ij} and ϵ_{kl}) generally related to one another by linearised

Hooke's law. Each directional index may assume values of 1, 2, 3 (representing directions x, y and z). There are nine such relations, each involving one component of stress and nine components of strain. These nine equations may be written as:

$$\sigma_{ij} = C_{ijkl} \epsilon_{kl} \quad (i, j = 1, 2, 3) \quad (\text{Eq.4.1})$$

$$\epsilon_{ij} = S_{ijkl} \sigma_{kl}; \quad (\text{Eq.4.2})$$

C_{ijkl} and S_{ijkl} are the fourth-order stiffness tensor and compliance tensor respectively. The relations between the tensor S and C is also as below:

$$S = C^{-1} \quad (\text{Eq.4.3})$$

Where $^{-1}$ illustrates the tensor inverse.

The 3*3*3*3 elastic modulus tensor C_{ijkl} completely characterises the elasticity of the medium. Because of the symmetry of stress ($\sigma_{ij} = \sigma_{ji}$) only six of these equations are independent. Because of the symmetry of strain ($\epsilon_{kl} = \epsilon_{lk}$) only six of the terms on the right side of each set of equations are independent. The elasticity can be represented more compactly with the change of indices using the Voigt notation defined below:

↓	ij or kl :	11	22	33	32=23	31=13	12=21
α	β	1	2	3	4	5	6

Therefore using this notation the 3*3*3*3 tensor C_{ijkl} may be represented by the 6*6 matrix $C_{\alpha\beta}$. Each symmetry class has its own pattern of nonzero, independent components $C_{\alpha\beta}$. For example for isotropic media the matrix assumes the simple form

$$C_{\alpha\beta} = \begin{pmatrix} C_{33} & (C_{33}-2C_{44}) & (C_{33}-2C_{44}) & 0 & 0 & 0 \\ 0 & C_{33} & (C_{33}-2C_{44}) & 0 & 0 & 0 \\ 0 & 0 & C_{33} & 0 & 0 & 0 \\ 0 & 0 & 0 & C_{44} & 0 & 0 \\ 0 & 0 & 0 & 0 & C_{44} & 0 \\ 0 & 0 & 0 & 0 & 0 & C_{44} \end{pmatrix} \dots$$

isotropy

These components are related to the Lamé parameters λ , μ and to the Bulk modulus K by:

$$C_{33} = \lambda + 2\mu = K + 4/3\mu \quad (\text{Eq.4.4})$$

$$C_{44} = \mu \quad (\text{Eq.4.5})$$

The simplest anisotropic case of broad geophysical applicability has one distinct variation axis (usually vertical) while the other two directions are equivalent to each other. This case is called transverse isotropy (TI) or hexagonal symmetry.

The elastic modulus matrix has five independent components among twelve nonzero components as below:

$$C_{\alpha\beta} = \begin{pmatrix} C_{11} & (C_{11}-2C_{66}) & C_{13} & 0 & 0 & 0 \\ 0 & C_{11} & C_{13} & 0 & 0 & 0 \\ 0 & 0 & C_{13} & 0 & 0 & 0 \\ 0 & 0 & 0 & C_{44} & 0 & 0 \\ 0 & 0 & 0 & 0 & C_{44} & 0 \\ 0 & 0 & 0 & 0 & 0 & C_{66} \end{pmatrix} \dots \text{TI}$$

(Where the third direction (z) is taken as the unique axis). It is significant that the generalisation from isotropy to anisotropy introduces three new elastic moduli. If the physical cause of anisotropy is known (for example the presence of the thin layering in the matrix of the isotropic media), these five moduli may not be independent. Knowing the exact cause for anisotropy is quite challenging; therefore, in general we treat the case using the following steps:

$$\begin{array}{l}
 C_{11}=C_{33} \\
 C_{66}=C_{44} \\
 C_{13}=C_{33}=2C_{44}
 \end{array}
 \left. \vphantom{\begin{array}{l} C_{11}=C_{33} \\ C_{66}=C_{44} \\ C_{13}=C_{33}=2C_{44} \end{array}} \right\} \dots \text{isotropy}$$

The elastic modulus matrix $C_{\alpha\beta}$ from the transverse isotropy matrix may be used to reconstruct the tensor C_{ijkl} using Voigt notation so that the constitutive relation in equation 4.1 (stress and strain relation) is known for an anisotropic medium. This relation can be used in the equation of motion (Daley and Hron 1977), yielding a wave equation.

There are three independent solutions of this equation:

$$\begin{array}{l}
 1- \text{ Quasi-longitudinal} \\
 2- \text{ Transverse} \\
 3- \text{ Quasi-transverse}
 \end{array}
 \left. \vphantom{\begin{array}{l} 1- \text{ Quasi-longitudinal} \\ 2- \text{ Transverse} \\ 3- \text{ Quasi-transverse} \end{array}} \right\} \text{ for each direction of propagation}$$

These three are polarised in mutually orthogonal directions. The exactly transverse wave has a polarisation vector with no displacement component in the 3rd direction. It is denoted by S_H ; the other vector is denoted by S_V . Daley and Hron (1977) give a clear derivation of the directional dependence of the three phase velocities:

$$\rho V_p^2(\theta) = 1/2 [C_{33} + C_{44} + (C_{11} - C_{33})\sin^2\theta + D(\theta)] \quad (\text{Eq.4.6})$$

$$\rho V_{SV}^2(\theta) = 1/2 [C_{33} + C_{44} + (C_{11} - C_{33})\sin^2\theta - D(\theta)] \quad (\text{Eq.4.7})$$

$$\rho V_{SH}^2(\theta) = C_{66}\sin^2\theta + C_{44}\cos^2\theta \quad (\text{Eq.4.8})$$

ρ is density, phase angle θ is the angle between the wavefront normal and the unique (vertical) axis.

$$D(\theta) = \left\{ (C_{33}-C_{44})^2 + 2[2(C_{13}+C_{44})^2 - (C_{33}-C_{44})(C_{11}+C_{33}-2C_{44})] \sin^2\theta + [(C_{11}+C_{33}-2C_{44})^2 - 4(C_{13}+C_{44})^2] \sin^4\theta \right\}^{1/2} \quad (\text{Eq.4.9})$$

The algebraic complexity of D is a primary obstacle to the use of anisotropic models in analysing seismic exploration data.

Some suitable combinations are suggested by Mavko (2009) as the following equations:

$$\xi = C_{11} - C_{33}/2C_{33} \quad (\text{Eq.4.10})$$

$$\gamma = C_{66} - C_{44}/2C_{44} \quad (\text{Eq.4.11})$$

$$\delta = 1/2C_{33} \left[2(C_{13}+C_{44})^2 - (C_{33}-C_{44})(C_{11}+C_{33}-2C_{44}) \right] \quad (\text{Eq.4.12})$$

The vertical propagation velocity for P and S waves are respectively:

$$\alpha_0 = \sqrt{C_{33}/\rho} \quad (\text{Eq.4.13})$$

$$\beta_0 = \sqrt{C_{44}/\rho} \quad (\text{Eq.4.14})$$

Then the equations 15 to 18 can be re-written as:

$$V_p^2(\theta) = \alpha_0^2 [1 + \xi \sin 2\theta + D(\theta)] \quad (\text{Eq.4.15})$$

$$V_{SV}^2(\theta) = \beta_0^2 [1 + \alpha_0^2/\beta_0^2 \xi \sin 2\theta - \alpha_0^2/\beta_0^2 D(\theta)] \quad (\text{Eq.4.16})$$

$$V_{SH}^2(\theta) = \beta_0^2 [1 + 2\gamma \sin^2\theta] \quad (\text{Eq.4.17})$$

$$D(\theta) = \frac{1}{2} (1 - \beta_0^2 / \alpha_0^2) \left\{ [1 + 4\delta / (1 - \beta_0^2 / \alpha_0^2)]^2 \sin^2\theta \cos^2\theta + 4(1 - \beta_0^2 / \alpha_0^2 + \xi) \xi / (1 - \beta_0^2 / \alpha_0^2)^2 * \sin^4\theta \right\}^{1/2} - 1 \quad (\text{Eq.4.18})$$

High hydrostatic stress closes the cracks inside the rock matrix; consequently, the measured properties represent solely the solid framework parts of the rocks. However, if the stress is applied only in one direction (uniaxial stress) the isotropic stress field is violated and the rock compresses in one direction and expands in other orthogonal directions. That can lead to the creation of new cracks, which will be oriented perpendicular to the stress direction. In other words, if the inner rock structure is considered as isotropic before applying the stress, by applying uniaxial stress the azimuthal anisotropic has been introduced to the rock and affects the whole elastic behaviour of the sample. Once the stiffness tensors are computed, the stress-dependent

velocities can be estimated and compared to the laboratory-measured data (Mavko et al. 1995).

To estimate anisotropic velocities the steps below were followed:

- 1) Ultrasonic measurement of P- and S-wave velocities in three orientations of the samples (horizontal, vertical and diagonal as representing 90, 0 and 45 degrees respectively) in a dry condition while applying hydrostatic stress;
- 2) Ultrasonic measurement of P- and S-wave velocities in three orientations of the samples (horizontal, vertical and diagonal as representing 90, 0 and 45 degrees respectively) in a fully saturation condition while applying hydrostatic stress along with applying constant pore pressure;
- 3) Ultrasonic measurement of P- and S-wave velocities in three orientations of the samples (horizontal, vertical and diagonal as representing 90, 0 and 45 degrees respectively) in a dry condition while applying uniaxial stress;
- 4) Calculation of C_{11} , C_{12} , C_{33} , C_{44} , C_{13} and C_{66} from the following equations;

$$C_{11} = \rho V_p^2 \text{ (horizontal)} \quad (\text{Eq.4.19})$$

$$C_{12} = C_{11} - (2\rho V_s^2) \text{ (horizontal)} \quad (\text{Eq.4.20})$$

$$C_{33} = \rho V_p^2 \text{ (vertical)} \quad (\text{Eq.4.21})$$

$$C_{44} = \rho V_s^2 \text{ (vertical)} \quad (\text{Eq.4.22})$$

$$C_{13} = -C_{44} + [4\rho^2 V_p^4 \text{ (diagonal)} - 2\rho V_p^2 \text{ (diagonal)} * (C_{11} + C_{33} + 2C_{44}) + (C_{11} + C_{44}) * (C_{33} + C_{44})]^{1/2} \quad (\text{Eq.4.23})$$

$$C_{66} = (C_{11} - C_{12})/2 \quad (\text{Eq.4.24})$$

- 5) Computation of anisotropy parameters using equations 4.10, 4.11 and 4.12;
- 6) Estimation of isotropic compliance and stiffness tensors when applying hydrostatic stress (C_{ijkl}^0 and S_{ijkl}^0).

The components of isotropic stiffness tensor from the Voigt notation from the measured P- and S- velocities can be summarised upon the wave type as:

$$C_{11} = C_{22} = C_{33} = \rho V_p^2 \quad (\text{Eq.4.25})$$

$$C_{44} = C_{55} = C_{66} = \rho V_s^2 \quad (\text{Eq.4.26})$$

$$C_{12} = C_{13} = C_{23} = C_{11} - 2C_{44} \quad (\text{Eq.4.27})$$

4.5 Closure of the pores and cracks to create isotropic background

Before being inserted into the pressure cell, the sample possesses all its open pores and micro-cracks. These govern the elastic behaviour of the rocks and can easily be observed by comparing the ultrasonic measurements for before and after applying the pressure. By inserting the sample inside the pressure cell and applying pressure these open pores and cracks start to close and diminish. Increasing the stress eliminates the effect of pores and cracks and leads to a more isotropic background. The velocities of P- and S-waves are the best indicators for such a change in the elastic properties of the sample. The change continues as the stress is increased and stops once it reaches the point where we assume all the pores and cracks have fully closed. When the sample reaches that point no more change in the velocities can be observed by increasing the pressure. The elastic properties remain almost unchanged until we pass the linear portion of the graph and enter the plastic zone.

Figure 4-1 demonstrates this behaviour on graphs for both P- and S-waves for porous and engineered material subjected to hydrostatic stress. The shutting down of the pores in sandstones happens at different stages and is not linear by applying stress; however, engineered elastic material behaves in a purely elastic way, and by stress unloading the waves return to their original arrangements. V_p and V_s increase with increasing hydrostatic stress for both samples; however, the change in porous media (Berea sandstone) is more obvious than the PMMA –this is as a result of the closure of the pores and micro-cracks. The changes become almost constant at about 15 MPa for Berea sandstone (for both P- and S- velocities). PMMA displays linear elastic behaviour and for P-wave velocity becomes almost constant from 10 MPa. For velocity of S-wave, PMMA shows constant behaviour from 40 MPa on.

The raw wavelets measured in the laboratory demonstrate this behaviour clearly for PMMA (*Figure 4-2*). In this figure, the red solid line on the first arrivals clearly indicates the return to the initial state after the unloading sequence. It should be noted here that PMMA does not possess pores and micro-fractures and the increase in velocity depends on compaction only. Therefore, following unloading the medium returns to its original state after couple of hours. For the porous media, on the other hand, the velocities increase by loading to the point where full closure of the voids

happens and no more change is observable. Following unloading this velocity decreases to near its initial state. Both statements are correct for the linear regime of the stress–strain graph while the medium is in elastic zone.

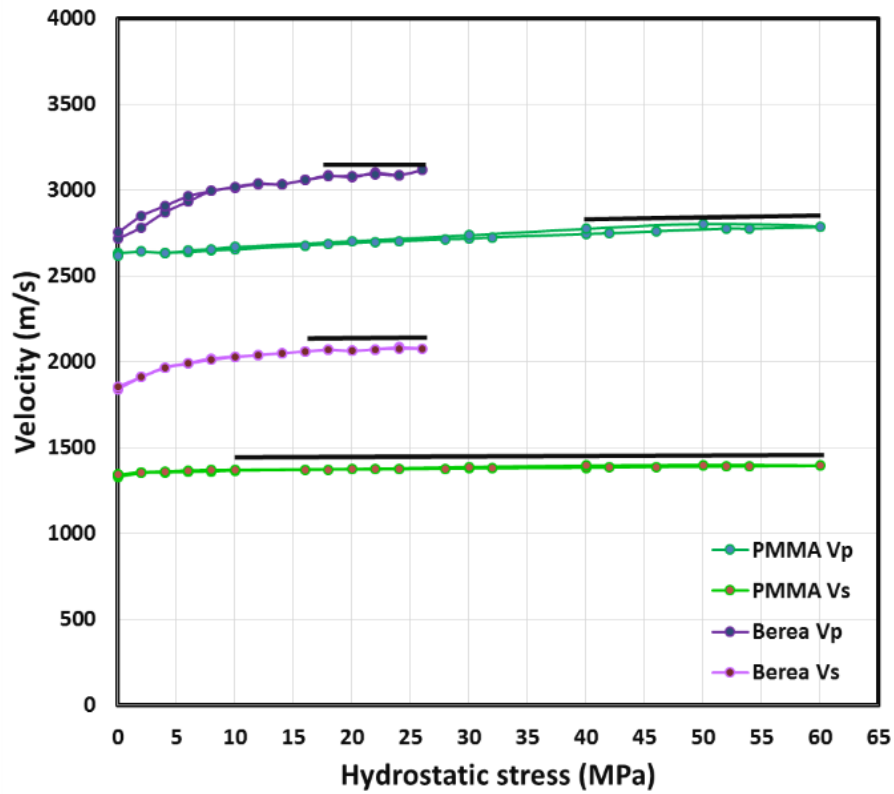


Figure 4-1 Vp and Vs subject to hydrostatic stress on dry sandstone and PMMA core samples.

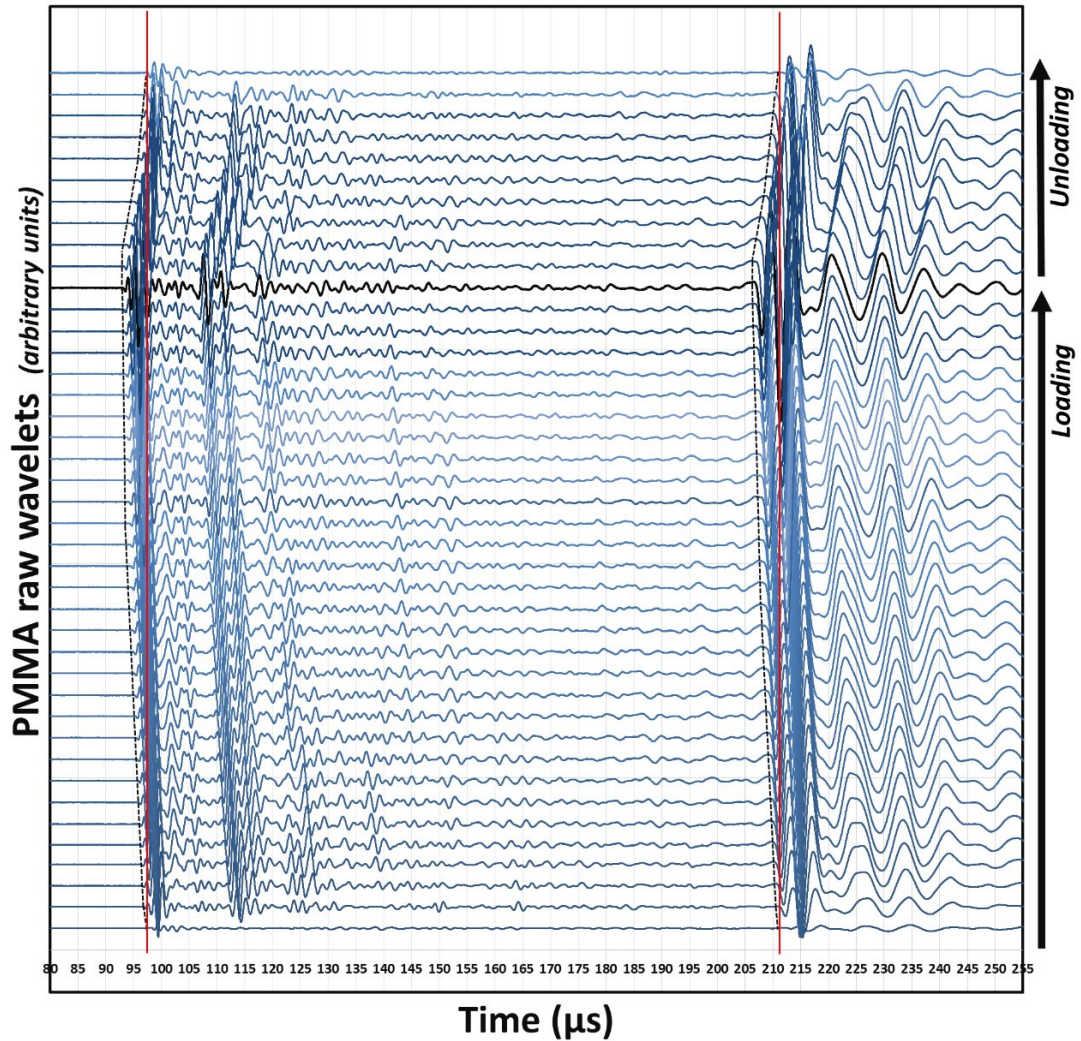


Figure 4-2 Raw wavelets of PMMA in the loading and unloading process. The sample displays linear elastic and following unloading the velocities of both P- and S-waves return to their original states (the red solid lines indicate the return of first arrival to the original state). For the loading the intervals sat for 2 MPa while for unloading the intervals were 10 MPa and the sharper change is due to this change of intervals. It should be noted that wavelets have not modified for first arrivals based on equation of the line by PEEK plates.

The most important challenge of the theoretical modelling is to formulate the crack compliances tensor ΔS_{ijkl} , which is nonlinear. Most of the proposed models in the literature focus on the geometry of the pores and cracks (angular distribution of penny-shaped cracks assumption). Such experimental measurements in the rock physics lab is quite difficult (Nur 1971; Gibson and Toksz 1989; Sayers et al. 1990). In experimental studies models such as Mavko and Sayers's are preferable because they do not require specific geometry for the cracks. In the mentioned models ΔS_{ijkl} directly computes by the velocities of P- and S-waves subjected to hydrostatic stresses and,

therefore, with experimental studies like ours it's quite easy to compute such tensors without complication. Note that it is necessary to estimate the compliance when applying a very high isotropic confining stress (S_{ijkl}^0). Experimental observations of velocity–stress curves under confining pressure are key measurements.

4.6 Materials and Methods

Laboratory measurement provides isotropic and anisotropic data of Harvey-3 sandstone based on the applied combination of the stresses. Harvey-3 sandstone is a porous, quartz-rich reservoir rock which is extracted from Western Australia. Medium-grain core samples of different lengths were drilled to be investigated in this study in three different directions: parallel, perpendicular and diagonal to the layering system (*Figure 4-3*). The cores' specifications are listed in *Table 4-1*, and velocities were measured on all three core samples at ambient. Core dimensions met the standard where the travel distance exceeds 10 times the average grain size. The lateral dimension also is greater than 10 times the wave length (ISRM 2007). Core preparation was used to avoid any stress concentration on the parallel top and bottom faces and on the circumference of the cores. Samples were then dried out in a vacuumed oven and a layer of couplant was applied at each end of the sample for better contact. The P- and S-wave velocities, porosity and density are required parameters to calculate anisotropy parameters while the sample is subjected to stress and saturation.

Harvey-3 samples	Length (mm)	Diameter (mm)	Density (g/cm ³)	V _p /V _s no stress	Porosity ϕ
<i>Horizontal</i>	41.10	38.53	2.07	1.53	0.14
<i>Vertical</i>	73.24	38.39	2.06	1.57	0.14
<i>Diagonal</i>	45.62	38.45	2.06	1.54	0.14

Table 4-1 Harvey-3 samples' properties in three directions

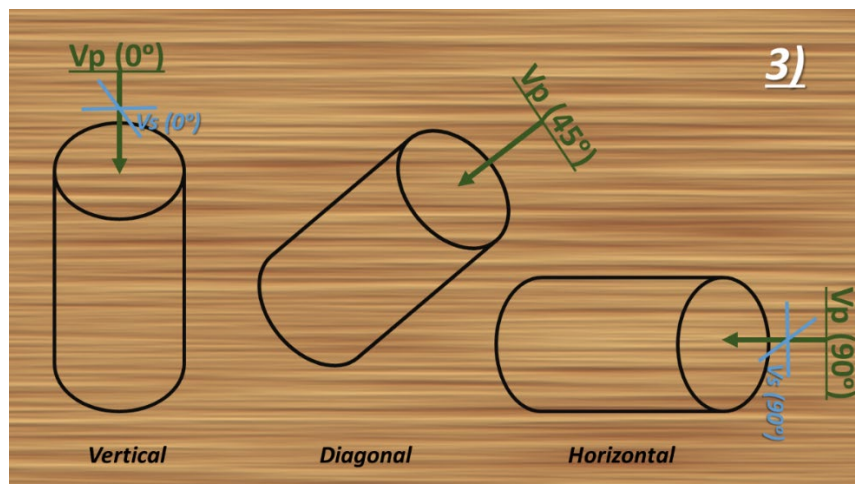
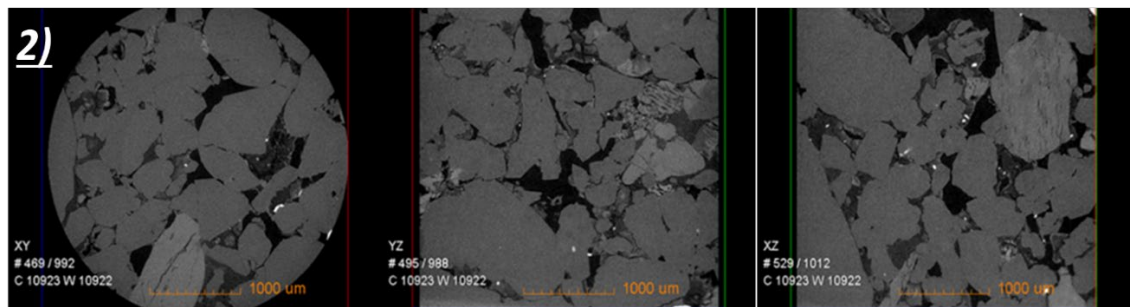
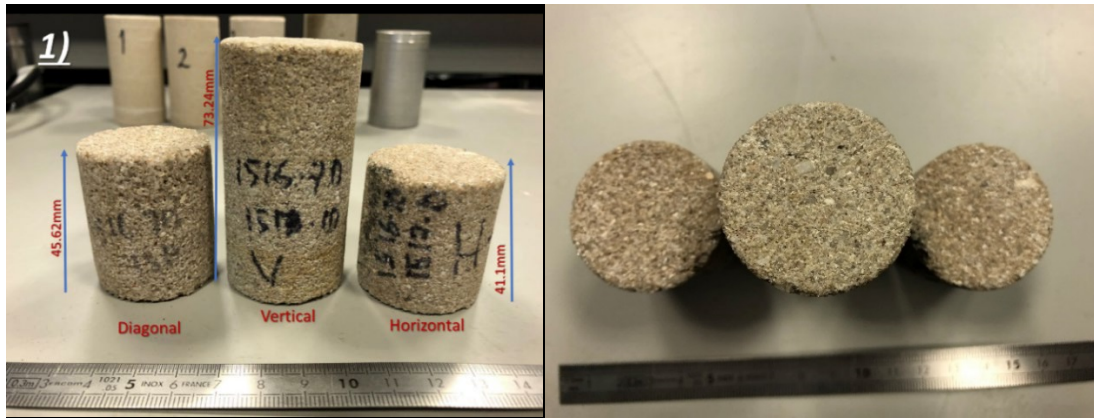


Figure 4-3 (1) Harvey-3 sandstone samples extracted in three directions: horizontal, vertical and diagonal to the deposition system; (2) mutual orthogonal cross-sectional slices, obtained from micro-CT images, field of view is 3 mm; and (3) schematic demonstration on terms parallel and perpendicular to the layering states of the samples

The core plugs orientations are: Normal, parallel to the bedding, and at a 45 degree angle. In this study the velocities were measured by a pulse-transmission technique with two pairs of 1 MHz central frequency P- and S-wave transducers. The porosity was measured by full saturation with DI water inside the vacuum and by calculating the weight after an oven-drying process at 80° C for 48 hrs.

4.6.1 Experimental set-up

The use of ultrasonic measurements to investigate the pulse velocities and elastic constants for rocks has been standardised in the American Society for Testing and Materials (ASTM) standard D2845-95. Based on this standard, P- and S-wave velocities were measured using a standard ultrasonic pulse transmission technique while loading and unloading the samples. The ultrasonic set-up consists of a pair of V153, 1 MHz S-wave transducers (Olympus Ltd) housed inside a brass mould. These transducers contain a 15mm piezo ceramic disk. A pulser/receiver 5077PR (Olympus Ltd) electronic block, and a digital 300MHz 2.5GS/s 4-channel oscilloscope TDS3034C (Tektronix Ltd) were implemented to record the electrical signals. PEEK rods were used for the sake of uniformity of stress application and they were in direct contact with the transducers block. The sample sits right between PEEKs on the same diameter inside the Hook cell membrane. A square electrical pulse of 1 μ s in duration with a 400 amplitude was applied to the transmitter transducer, which converted the electrical pulse to a mechanical pulse at the sample's boundary and generates an ultrasonic wave that propagates inside the sample. The receiver is housed on the opposite surface of the sample, which then converts the mechanical pulse into an electrical pulse. To ensure uniform stress application the sample was placed in between two PEEK rods of the same diameter and attached to the transducers inside the mould blocks. The axial pressure actuator applied pressure on the top plane. The sample was placed inside the Hook cell for the lateral pressure by hydraulic pump. The pulse transmission technique was used to record the P- and S-wave velocities. The velocities of either P- or S-waves were calculated from the measured travel time and the distance between the transmitter and receiver. To record the wavelets it should be remembered that the noise level should not be greater than one tenth of the amplitude of the first peak. The travel times should be measured to a precision and accuracy of 1 part in 100 for the P-wave and 1 part in 50 for the S-wave by using delaying circuits in conjunction with the oscilloscope. The hydrostatic stress frame and its components are labelled in *Figure 4-4*. The pressure system for this experiment consists of hydrostatic loading and an automatic pore pressure pump for injecting DI water with constant pressure throughout the experiment.

The following steps of loading and saturation were practiced for each sample (horizontal, vertical and diagonal) while the ultrasonic waves were recorded: a) Loading of stress from 2 MPa to 32 MPa with intervals of 4 MPa; b) unloading; c) saturating the unloaded sample by DI-water inside the set-up by use of the controlled pump and vacuum for 24 hrs, d) by reaching the full saturation the constant pore pressure sat at 5 MPa and the sample and the saturated experiment began on the same sequences of effective stress at the same orientation of sample while subjected to stress and wave propagation, e) unloading the sample and removing it from the pressure cell (while the polarisation of S-wave was marked on the sample), weighing the sample right after the removal and putting into the oven for 72 hrs to dry and the dry weight was recorded, and f) putting the sample into the pressure cell for the uniaxial experiment with the same sequences and intervals of the stresses as the hydrostatic experiment to measure the anisotropy-induced velocities.



Figure 4-4 Layout of the experimental set-up: 1) Hook's cell and injection valves a) axial actuator, b) S-wave transducer, c) PEEK part, d) Hook's cell, e) input valve for fluid injection, and f) output valve for discharge and vacuum of the liquid. 2) a) hydrostatic pressure frame, b) pore pressure pump, and c) Ultrasonic bench equipment to record wavelets.

4.6.2 Initial velocity measurement at ambient

Before inserting the sample inside the pressure cell, precise measurement of the S- and P-wave velocities was performed to register the initial velocities. In these measurements, since no stress was applied, the velocity is considered as the velocity of background compliances, and cracks and pore compliances together. Each core sample (representative of one individual direction) was measured by a pair of P-wave transducers and a pair of S-wave transducers. The change in velocities and amplitudes clearly indicates the anisotropy of the sample based on the different directions. The P-wave signal transmitted through the dry vertical sample is quite weak and the noise ratio (marked in *Figure 4-5* in yellow) demonstrates the high damping effect of this direction for Harvey-3 sandstone. This signal was later enhanced once the sample was placed inside the pressure cell due to the compaction and saturation.

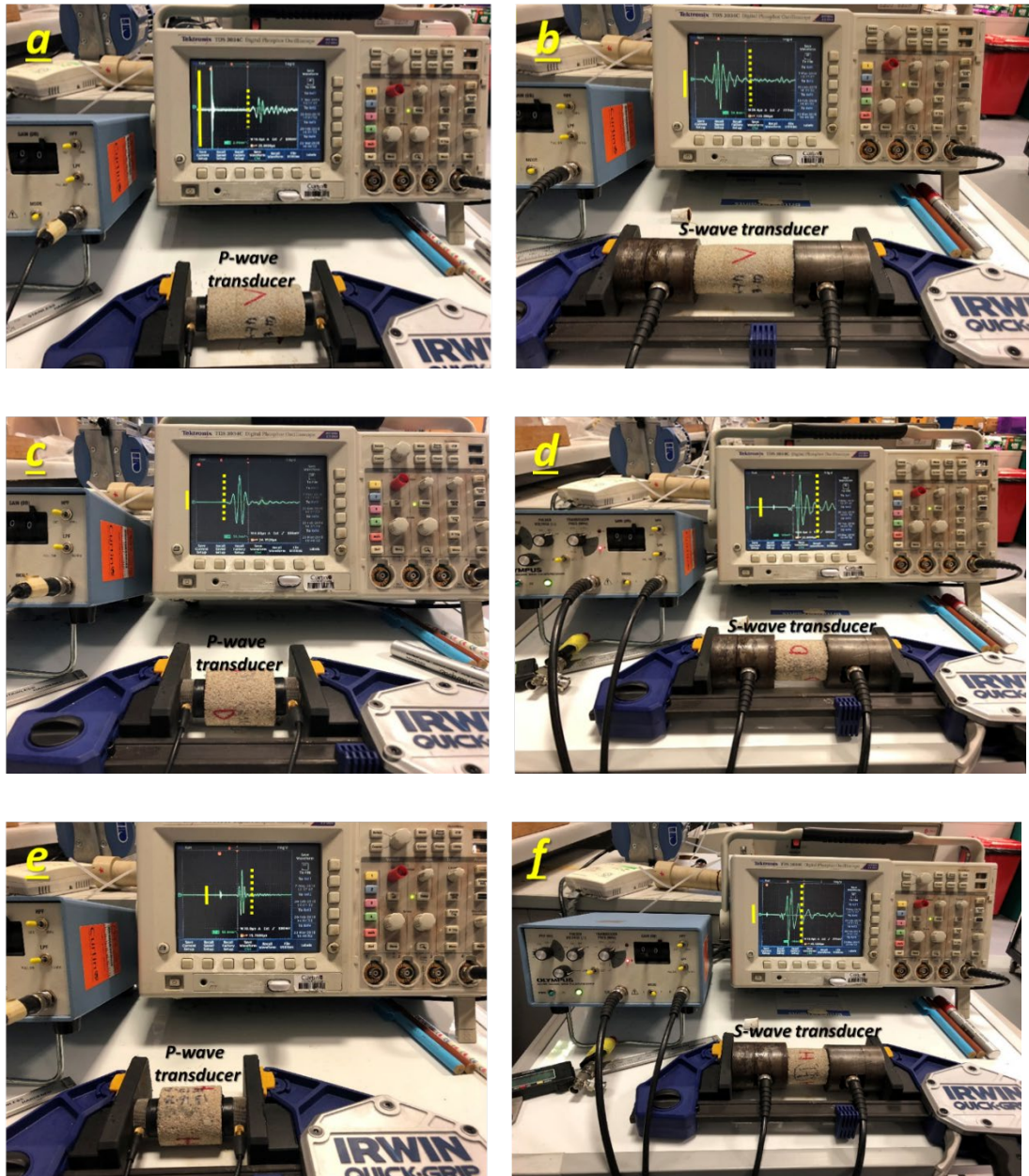


Figure 4-5 Initial measurement of Harvey-3 samples in the lab before being subjected to stress. (a b) Vertical sample, (c d) diagonal sample, and (e f) horizontal sample. The rigid yellow line defines the noise and dotted yellow line shows the observed wavelet for the P- and S- transducer measurements.

4.6.3 Aluminium calibration

To calibrate the pressure cell for the dynamic experiment we used an aluminium plug to extract the equation of line for PEEK's blocks (Figure 4-6). Later this equation was used to correct the first arrivals for the Harvey-3 core samples.

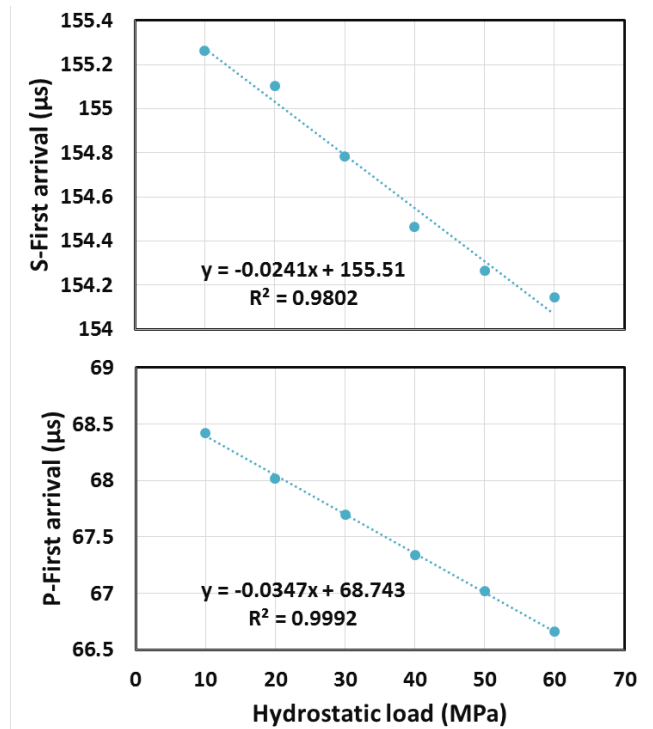


Figure 4-6 The equation of the line to the correct first arrival by passing through the PEEK blocks located at the top and the bottom of the tested samples.

4.7 Results and discussions

The velocities of P- and S-waves in three directional samples have been plotted in *Figure 4-7* and *Figure 4-8*. This graph shows that the velocities of both P- and S-waves in both dry and saturated conditions increased with increased effective stress. This graphs also stated the variations in velocities by different orientation of the layering, which clearly indicates the sample is anisotropic. V_p and V_s diagonal show the highest value among all the directions.

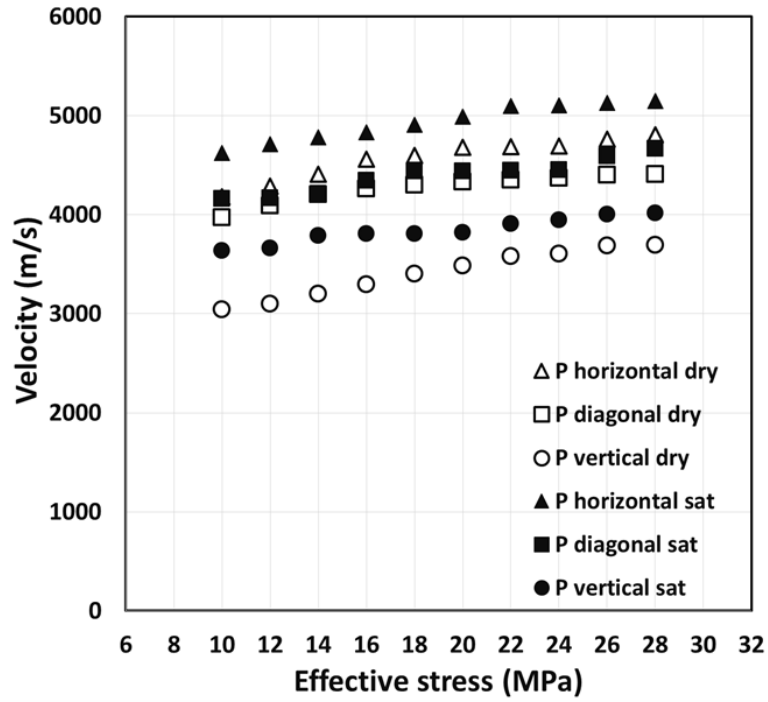


Figure 4-7 Stress dependency of P wave velocities for three dry and saturated samples of Harvey 3 (1516.7-1517.1m).

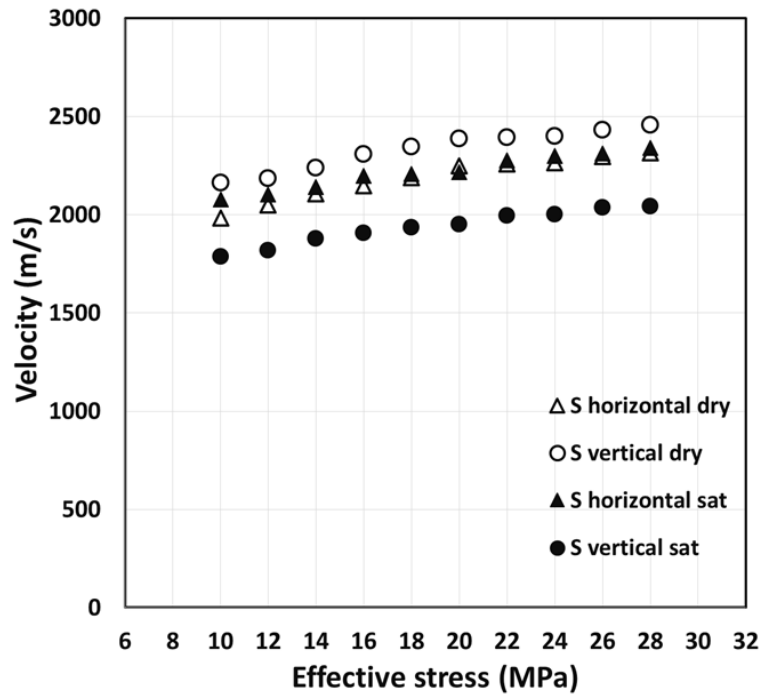


Figure 4-8 Stress dependency of S wave velocities for two dry and saturated samples of Harvey 3 (1516.7-1517.1m).

The effect of full saturation on the raw waveforms is quite obvious (*Figure 4-9* and *Figure 4-10*) for both P- and S-wave first arrivals. Saturation increased V_p in all

samples and this increase is more obvious for the vertical orientation. Full saturation decreases V_s at a higher rate than V_p ; therefore, we can conclude that S-wave velocity is more sensitive to full saturation than P-wave. The amplitude of the wave's increases with saturation and this change is the good indication of fully saturated sample. Partial saturation leads to reduced amplitude in the wavelets and in all three samples the recorded wavelets in the saturated state show an increase for this experiment.

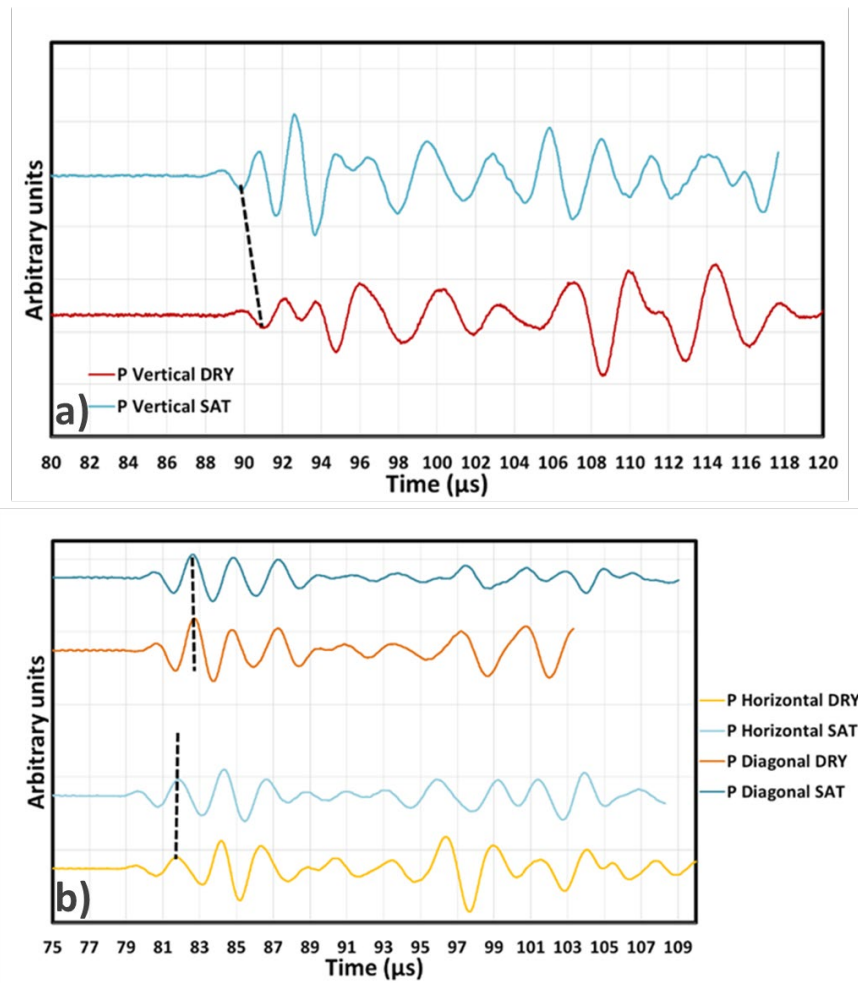


Figure 4-9 The effect of saturation on P-wave first arrivals of Harvey-3 at maximum hydrostatic effective stress (32 MPa) for horizontal (b), vertical (a) and diagonal (b) orientations.

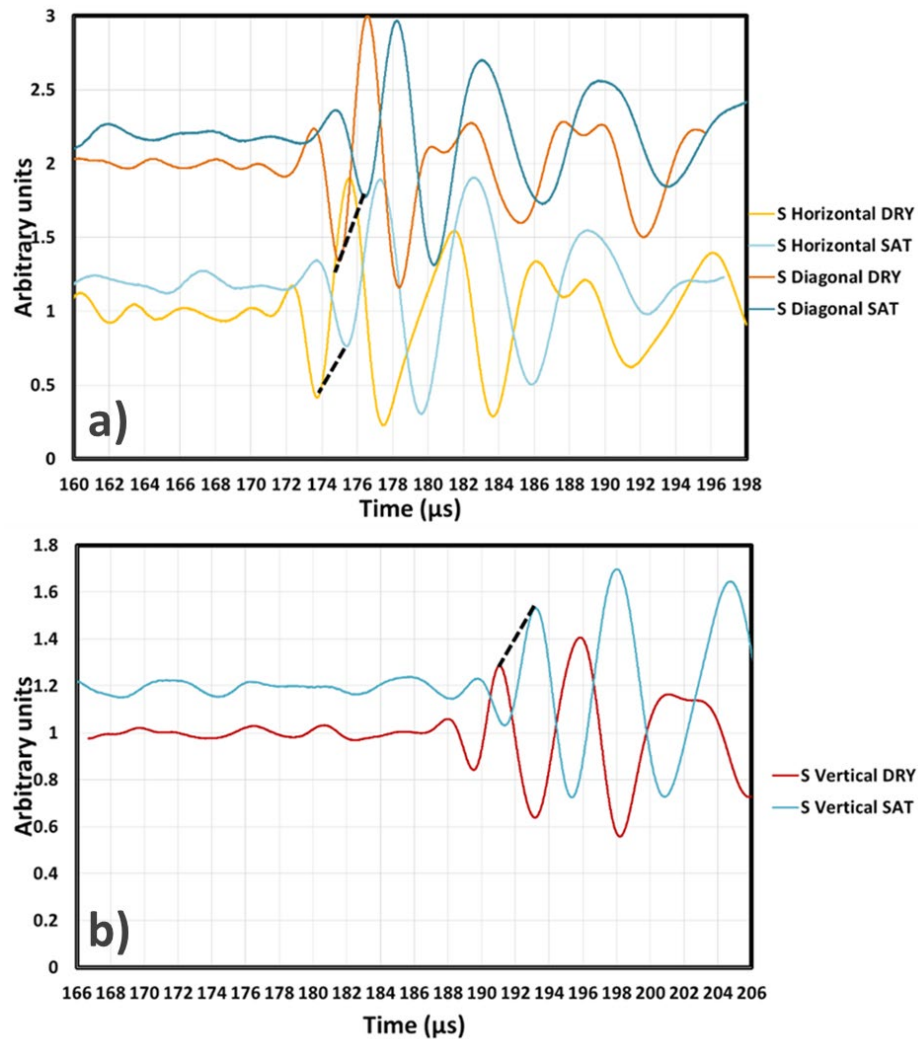


Figure 4-10 The effect of saturation on S-wave first arrivals of Harvey-3 at maximum hydrostatic effective stress (32 MPa) for horizontal (a), vertical (b) and diagonal (a) orientations.

The result plots the variation in P-wave velocity of 22 percent in dry and 15 percent in fully saturated horizontal and vertical samples at applied effective stress from 4 to 32 MPa respectively. The same trend was achieved by plotting the results of the diagonal (45 degree) sample of 16 percent in a dry and 8 percent in a fully saturated sample at applied effective stress of 4 to 32 MPa respectively. The reasons for the shifts of wavelets from dry to full saturation is well understood and predicted by the Gassmann theory (Gassmann 1951). While the sample is in the process of becoming saturated with water it enhances the total density and consequently reduces the velocities for P- and S-waves (partial saturation). Once it reaches full saturation and water fills all the gaps and pores inside the rock matrix, the sample becomes less compressible. Full

saturation increases the effective Bulk modulus; however, it has little effect on the Shear modulus. Consequently, compressional velocity (P-wave) increases while shear velocity (S-wave) reaches a minimum. Both statements have been clearly observed in *Figure 4-7* and *Figure 4-8*.

By drying out the sample after the experiment and conducting a new uniaxial test on the same orientation of the samples, *Figure 4-11* was extracted. For the uniaxial test the maximum applied stress was set below the UCS from 2 to 12 Mpa with the intervals of 2 MPa. The results clearly illustrate lower velocities due to the stress anisotropy ($x=y=0$ and $z>0$) and perhaps as a result of the creation of minor cracks inside the samples by double experiments of loading–unloading for two sets of dry and saturated experiments in the past. It should be noted that the experiment was conducted on the same orientation of each sample and therefore the results were expected to have less variation at low stress with regards to the hydrostatic dry experiment. However, this was not fulfilled. The sample horizontal failed at 12 MPa while doing the uniaxial experiment. This happens as a result of horizontal layering, which creates the weakest orientation, while applying stress parallel to this layering – especially if there is no support at the opposite directions. The next two samples (90 and 45 degrees to layering) possess higher UCS based on their layering orientations. This supports the statement that failure will be preceded by the growth of micro fractures parallel to the direction of maximum principal compressive stress in a horizontal direction (Sayers et al. 1990).

4.7.1 Ultrasonic velocities and anisotropy

By plotting the vertical and horizontal P-wave velocities (in orbit format) and comparing them to the diagonal recorded velocity (in dotted points) it can be observed that the P-wave velocity of the diagonal does not match the orbit of the P-wave velocities of the horizontal and vertical orientations in a dry condition (*Figure 4-11*). This difference seems to reduce and results match better for the samples tested in a saturated conditions (*Figure 4-12*). It should be noted that on higher stresses this difference is smaller than in lower stresses. This can be interpreted as being due to the closure of the pores and micro-cracks while subjected to hydrostatic pressure, and the sample becoming more isotropic due to this change. For a Transverse Isotropic (TI)

media such as paper-reinforced phenolic material (*Figure 4-13*) we can clearly see this dependency, and the results of three-directional measurement on P-wave velocity clearly indicate that the diagonal value matches perfectly with the elliptical measurement of the horizontal and vertical velocity data. The TI material measurement can be considered as the calibration test for the experiment while the same directional measurement is performed for the Harvey-3 sandstone.

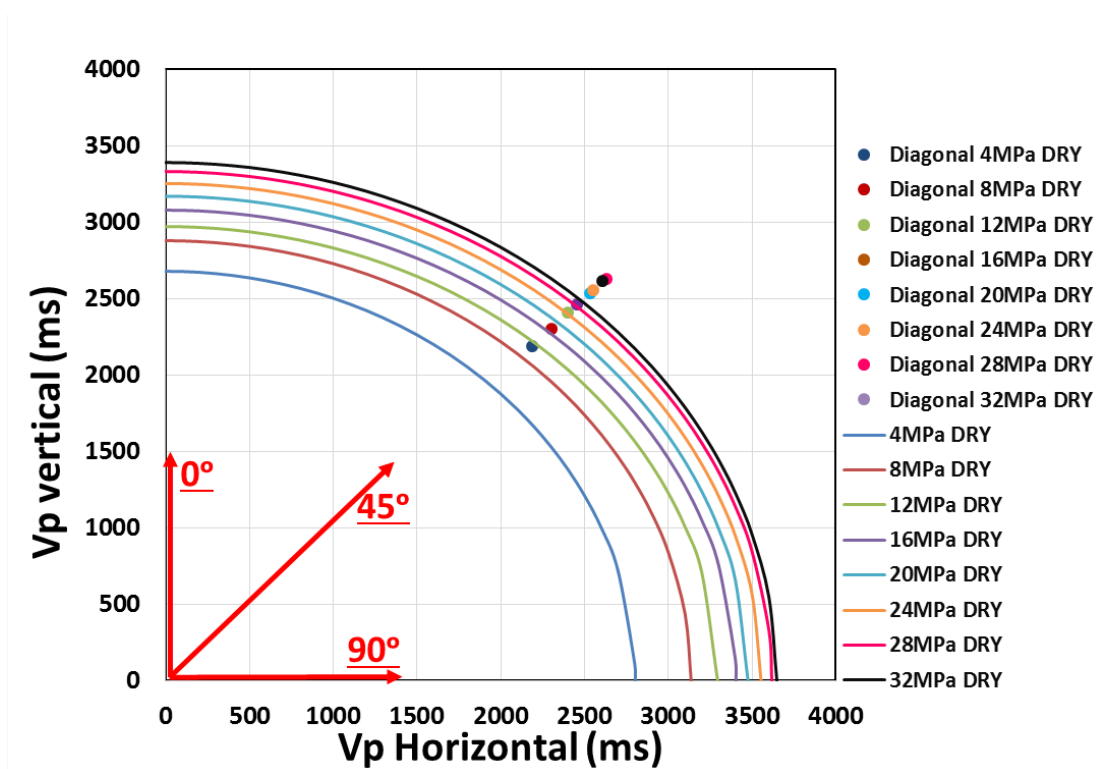


Figure 4-11 P-wave velocities of vertical and horizontal in comparison to P-wave velocity diagonal in a dry condition.

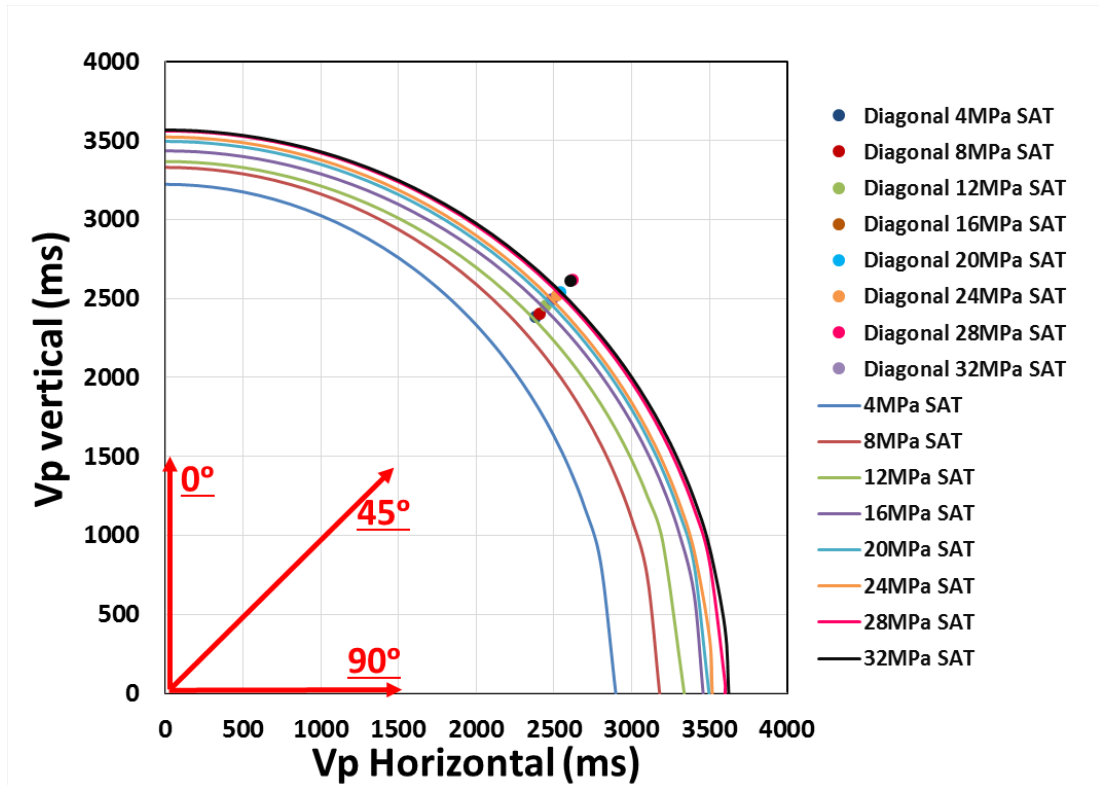


Figure 4-12 P-wave velocities of vertical and horizontal in comparison to P-wave velocity diagonal in a saturated condition.

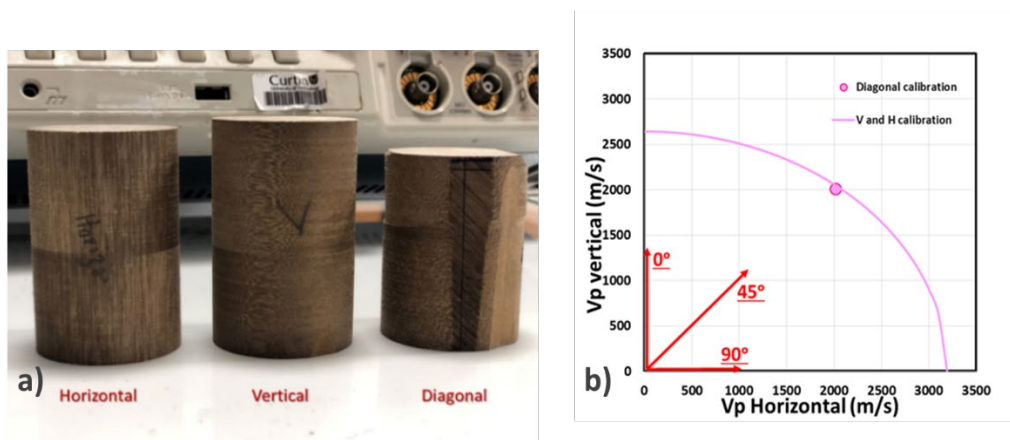


Figure 4-13 Synthetic Transverse Isotropic (TI) media (paper-reinforced phenolic material) (a) tested as calibration to present the elliptical anisotropy based on placement of diagonal location on the elliptical of the vertical and horizontal velocity of the P-wave (b).

4.7.2 Anisotropy affected by saturation and stress

Transverse isotropic media can be adequately described by five independent elastic constants: C_{11} , C_{33} , C_{44} , C_{66} , and C_{13} . After White (1965) and Lyakhovitsky (1988) the three phase velocities of waves propagating at an angle θ to the symmetry axis are given by three convenient anisotropy parameters introduced by Thomsen (1986) as

equations 4.10, 4.11 and 4.12. *Figure 4-14* demonstrates the results of calculated anisotropy in saturated and dry conditions. According to Thomsen (1986), this indicates that the sample possesses a higher degree of anisotropy than ellipticity in a dry condition and nearly elliptical anisotropy at full saturation. It is obvious that saturation and high confining stress lower the anisotropy and eliminate the effect of pores and micro-cracks Harvey-3 sandstone.

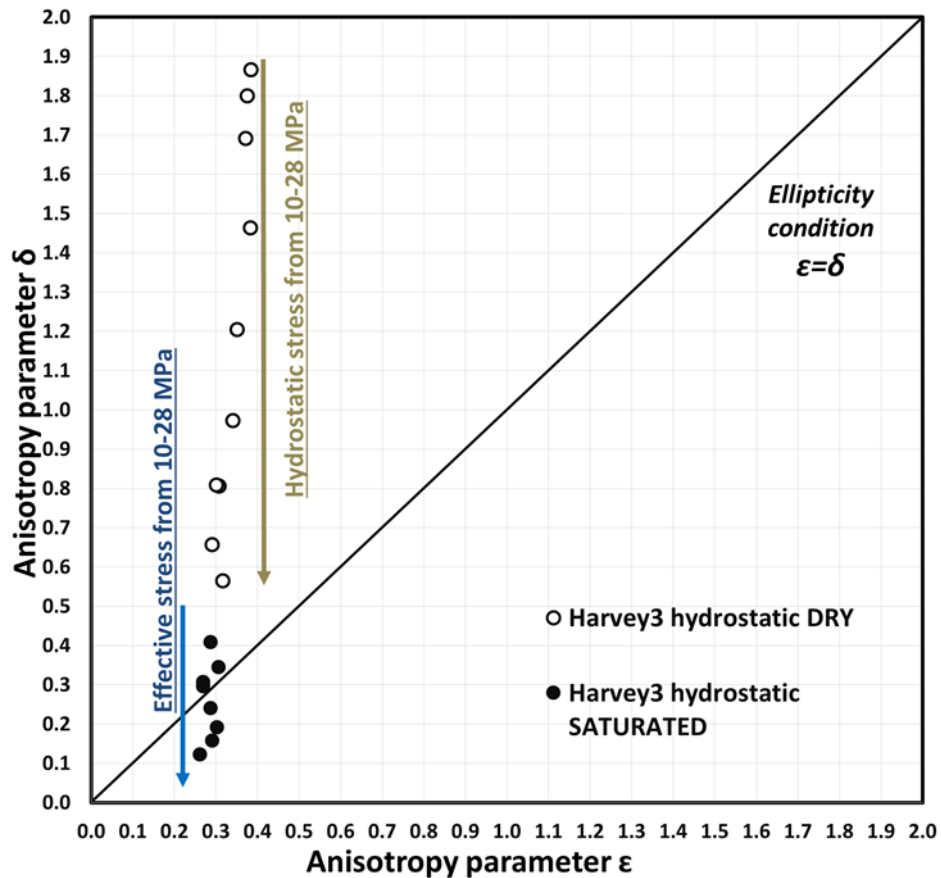


Figure 4-14 Comparison of P-wave anisotropies for hydrostatic condition.

The differences to the elliptical anisotropy have been calculated and plotted in *Figure 4-15*. By increasing the stress, the anisotropy parameters changed (*Figure 4-16*). The results are in agreement with past studies on reducing the anisotropy degree by pressure and saturation. It should be noted that the difference between the diagonal value and horizontal-vertical value is due to a small anisotropy that leads to an 8–5% change in a dry state and 4–2% difference in a saturated state for these two values by applying stress from 8 to 32 MPa. The effective stress below 8 MPa shows the high variation and therefore has been eliminated from the results graph.

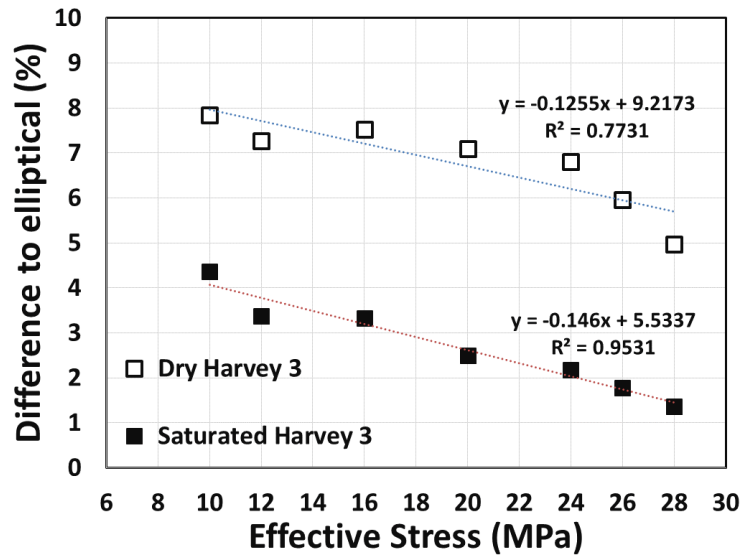


Figure 4-15 The differences to the elliptical condition caused by the effective stress for dry and saturated conditions.

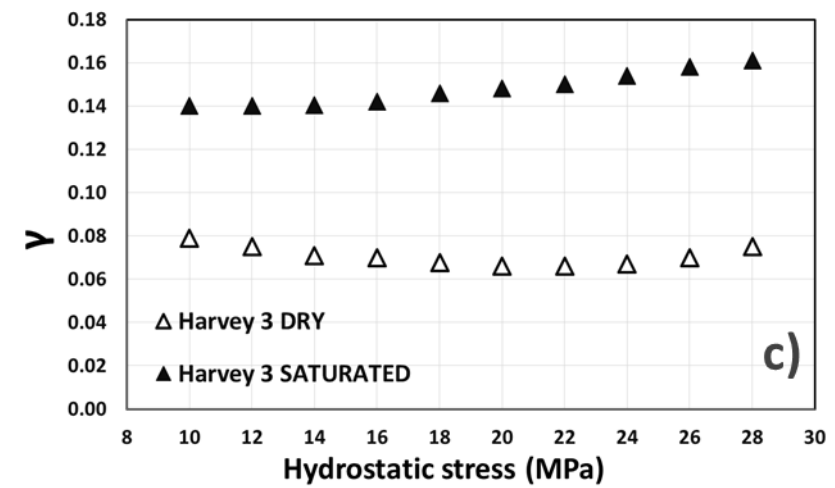
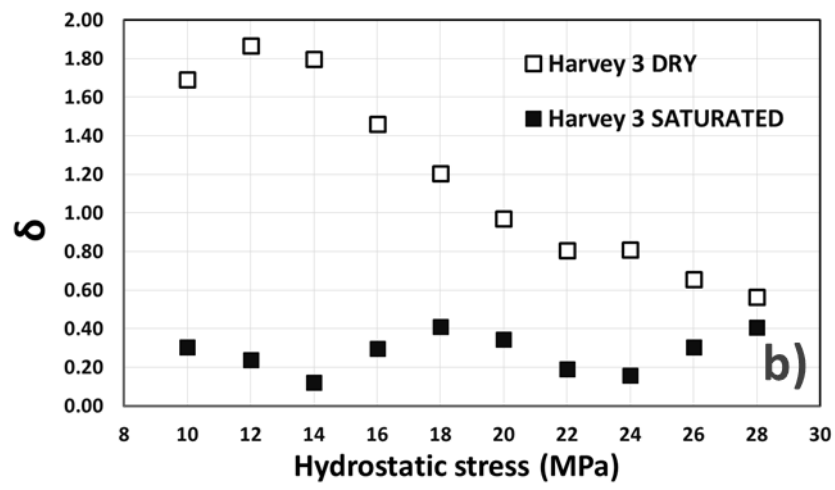
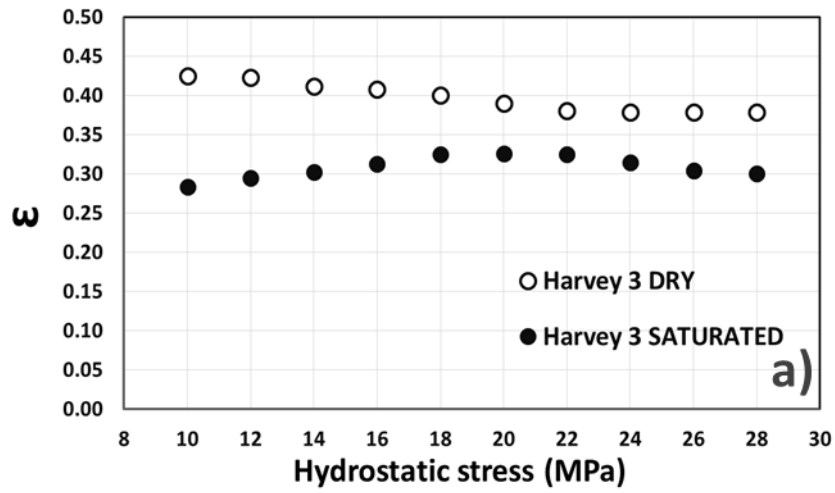


Figure 4-16 Anisotropy parameters described by (a) ϵ , (b) δ and (c) γ in dry and saturated states for Harvey-3 sandstone.

4.8 Conclusion

In this chapter we experimentally studied the effect of saturation and confining stress on the anisotropy parameters for the Harvey 3 sandstone. To perform this comparative test, we evaluated lab data on dry and fully saturated states of material in three directions of the medium. The stress configuration sat in an isotropic stress state for both saturated and dry tests. For saturated tests the effective stress sat similar to dry condition by the applying constant pore pressure for all intervals of confining stress. To complete this study, we varied the applied hydrostatic stress and compared the data measured in the two different states. The objective of this comparison was to experimentally observe the behaviour of anisotropic, porous sandstone while it was subjected to changes in the density and structure of its pores and micro-cracks. The core plugs of tested sandstone have poor sorting and the average density of the samples was measured 2.06 g/cm³ and the porosity estimated to be 14%. S- and P-waves velocity measured by ultrasonic transducers in a hydrostatic loading frame inside the Hook's cell. The effective loading of the hydrostatic stress ranged from 10 to 28MPa. This range is right below the sample's UCS (>40MPa). Anisotropic velocities were then calculated for three individual directions of Harvey 3 sandstone at dry and saturated conditions. The higher grade of anisotropy in the dry state of the Harvey 3 sandstone becomes near elliptical anisotropy by full saturation while applying stress. This confirms the theory in which the anisotropy degree decreases as pores and micro-cracks are eliminated. Such phenomenon of changing an elliptical anisotropy to non-elliptical one, in this particular reservoir, must be taking into account in the inversion of seismic data for 4D monitoring during, for example CO₂ injection. All three samples underwent a uniaxial test (the vertical component at z-axis was increasing while the confine support was zero) and the horizontal core plug failed at 14MPa. This direction was confirmed to be the weakest due to the collinearity of the force and the layering. The other two directions possess higher values of UCS as expected and this sheds light on the importance of correct detection of layering, even for non-obvious layered sandstones, such as medium-grain, porous the Harvey 3 sandstone.

Finally, we recommend that investigators apply this type of comparative analysis to precise laboratory data acquired on core samples for developing rock physical models, and reduce the number of unknown parameters - such as using estimated S-wave

velocities instead of directly measuring of such values - to enhance the accuracy of predictions. Such laboratory data clearly maps the real behaviour of the porous rock while subject to stress and saturation.

4.9 References to Chapter Four

Bakulin, A., V. Grechka, and I. Tsvankin, 2000, Estimation from fracture parameters from reflection seismic data-Part I: HTI model due to a single fracture set: *Geophysics*, 65,no. 6, 1788-1802.

Biot M. A. 1956. Theory of Propagation of Elastic Waves in a Fluid-Saturated Porous Solid. II. Higher Frequency Range. *The Journal of the Acoustical Society of America* 28, 179 (1956); <https://doi.org/10.1121/1.1908241>

Bonner, B., 1974, Shear wave birefringence in dilating granite: *Geophysical Research Letters*, 1, no. 5, 217-220.

Bording, R., and L. Lines, 1997, *Seismic Modeling and Imaging with the Complete Wave Equation*: Society of Exploration Geophysicists

Boulanouar A., Rahmouni A., Boukalouch M., Samaouali A., Géraud Y., Harnafi M., Sebbani J. 2013. Determination of Thermal Conductivity and Porosity of Building Stone from Ultrasonic Velocity Measurements, *Geomaterials* Vol.3 No.4(2013), Article ID:37908,7 pages DOI:10.4236/gm.2013.34018

Brandt H. 1955. A study of the speed of sound in porous granular media. *J. Applied Mech.* : 22, 479-486

Gao, F., A. Levander, G. Pratt, and C. Zelt, 2005, Seismic velocity, Q, geological structure and lithology estimation at a ground water contamination site: *SEG Technical Program Expanded Abstracts 2005*, 1561-1564.

Gibson, R. L., and M. N. Toksz, 1989, Permeability estimation from velocity anisotropy in fractured rock: *SEG Technical Program Expanded Abstracts 1989*, 573-575.

Grechka, V., and I. Tsvankin, 1999, 3-D moveout inversion in azimuthally anisotropic media with lateral velocity variation: Theory and a case study: *Geophysics*, 64, 1202-1218.

- Gregory, A. R. 1976. Fluid saturation effect on dynamic elastic properties of sedimentary rocks, *GEOPHYSICS*(1976),41(5):895
<http://dx.doi.org/10.1190/1.1440671>
- Gurevich, B., M. Pervukhina, and D. Makarynska, 2011, An analytic model for the stress induced anisotropy of dry rocks: *Geophysics*, 76, no 3., WA125-WA133.
- Hicks, W. G., and Berry J. E. 1956. Application of continuous logs to determination of fluid saturation of reservoir rocks, *Geophysics*, 21, 739-754.
- Hornby, B., J. Howie, and D. Ince, 2003, Anisotropy correction for deviated-well sonic logs: Application to seismic well tie: *Geophysics*, 68, no. 2, 464-471.
- ISRM .2007. The Complete ISRM Suggested Methods for Rock Characterization, Testing and Monitoring: 1974-2006. Suggested Methods Prepared by the Commission on Testing Methods, International Society for Rock Mechanics, Compilation Arranged by the ISRM Turkish National Group Ankara, Turkey, 628 p.
- Kassab M. A. , Weller A. 2015. Study on P-wave and S-wave velocity in dry and wet sandstones of Tushka region, Egypt. *Egyptian Journal of Petroleum* (2015) 24, 1–11
- Li, R., K. Dodds, A. Siggins, and M. Urosevic, 2006, A rock physics simulator and its application for CO₂ sequestration process: *Exploration Geophysics*, 37, no. 1, 67-72.
- Li, X., 1999, Fracture detection using azimuthal variation of P-wave moveout from orthogonal seismic survey lines: *Geophysics*, 64, no. 4, 240-256.
- Mavko, G., T. Mukerji, and N. Godfrey, 1995, Predicting stress induced velocity anisotropy in rocks: *Geophysics*, 60, 1081-1087.
- Nur, A., and G. Simmons, 1969, Stress-induced velocity anisotropy in rock: An experimental study: *Journal of Geophysical Research*, 74, 6667-6674.
- Nur, A., 1971, Effects of stress on velocity anisotropy in rocks with cracks: *Journal of Geophysical Research*, 76, no. 8, 2022-2034.
- Restrepo B. J., Shragge J., Lumley D. 2019. A Comparison of Rock Physics Models for Stress-related Seismic Azimuthal Anisotropy. *Journal of the Australian Society of Exploration Geophysicists*. EG17132 Accepted 24 May 2018

- Ruger, A., 1998, Variations of P-wave reflectivity with offset and azimuth in anisotropic media: *Geophysics*, 63, no. 3, 935-947.
- Sayers, C., J. V. Munster, and M. King, 1990, Stress-induced ultrasonic anisotropy in Berea Sandstone: *International Journal of Rock Mechanics and Mining Sciences & Geomechanics Abstracts*, 27, no. 5, 429-436.
- Shragge, J., and D. Lumley, 2012, Elliptical dip moveout for 3D seismic imaging in the presence of azimuthal anisotropy: *Geophysics*, 77, no. 1, C1-C12.
- Thomsen, L., 1999, Coarse-layer stripping of vertically variable azimuthal anisotropy from shear wave data: *Geophysics*, 64, 1126-1138.
- Tsvankin, I., J. Gaiser, V. Grechka, M. van der Baan, and L. Thomsen, 2010, Seismic anisotropy in exploration and reservoir characterization: An overview: *Geophysics*, 75, no. 5, A15-A29.
- Vavrycuk, V., and I. Psencik, 1998, Pp wave reflections coefficients in weakly anisotropic elastic media: *Geophysics*, 63, 2129-2141.
- Wang, S. X., and X. Li, 2006, Layer stripping of azimuthal anisotropy from P-wave reflection moveout in orthogonal survey line: *Journal of Geophysics and Engineering*, 3, no. 1, 1-11.
- Yo Fukushima, Osamu Nishizawa, Haruo Sato, and Masakazu Ohtake, 2003, Laboratory Study on Scattering Characteristics of Shear Waves in Rock Samples, *Bulletin of the Seismological Society of America*, Vol. 93, No. 1, pp. 253-263, February 2003

Chapter 5 Petrophysical analysis using ultrasonic waves in porous media by Laser Doppler Interferometry

5.1 Foreword

This chapter investigates the core scale ultrasonic velocity analysis utilizing Laser Doppler Interferometry (LDI) in the presence of no confining pressure for samples of the Gosford sandstone. The results of this chapter has been submitted in *Geophysical Prospecting* and is currently under review.

5.2 Abstract

The change of ultrasonic velocities and displacement on the core scale for the isotropic Gosford sandstone was studied using the Laser Doppler Interferometry method. We observed that the P- and S-wave velocities and the corresponding surface displacements of the sample can consist of multiple wavelets at core scale. We propose a method to determine the velocity field on the Gosford sandstone using Laser Doppler Interferometry (LDI) as a point receiver. Ultrasonic velocity experiments are implemented to investigate the elastic properties and internal structure of a sample. This usually takes place by measuring the average wavelet recorded by the receiver transducer. We designed an experiment to measure points inside and outside the transducer zone by dividing the surface into inner and outer orbits to investigate wave propagation on the micro scale for Gosford sandstone. The recorded travel velocity varies as a function of the material's mechanical properties, therefore knowing these averaged components can be used to understand such behaviour in detail. By changing the monitoring system from a receiving transducer (which normally has a 10 to 15 mm diameter) to a laser beam (which occupies an area of diameter of 0.2 mm on the same surface) enables us to scan the behaviour of transmitted wave at much higher spatial resolution and observe different zones on the surface of sample. A Laser Doppler Interferometer, as a receiver, benefits this experimental study over piezoelectric transducers because: a) A much smaller area of measurement than the wavelength is covered, and b) it records the full particle-velocity wave field and displacement vector. This study can map the displacement field within the boundaries of the source transducer and outer orbit of this region. The study of such displacement on the surface of source transducer also gives the baseline as a comparison once the wave passes

through the sample. We investigated such changes for the engineered PMMA and Gosford sandstone and compared the displacement rate for the sample on the nanometre scale. Finally, by observing the averaging of the recorded wavelets on random surface measuring points, the resemblance to the velocity recorded by a receiver transducer (instead of a laser) was in good agreement, which verified the accuracy of the component's wavelets and validity of this experimental approach.

5.3 Introduction

An elastic wave is the propagation of a disturbance through a medium, caused by the vibration of the particles. Two types of body waves can propagate through a solid medium: P-wave (longitudinal wave), and S-waves (shear waves). A P-wave creates particle vibration parallel to the direction of the wave traveling (the wave front propagation direction), while an S-waves which are orthogonally polarized creates vibration perpendicular to the wave propagation direction. As a result of such a difference in wave propagation pattern and relevant material properties, P-waves travel faster than S waves. Also, S-waves travel only through solid bodies and cannot pass through fluid or gas because their material, have no shear strength. The velocity the wave travels at depends on the material and the type of the wave (P- or S-wave). The frequency of the wave is defined as the number of cycles of particle vibration per second. The frequency of a wave depends on the impact of the input source and uses Hertz (Hz) as the measurement units. The wavelength is expressed as the distance between successive vibration peaks. The wavelength, frequency and velocity of a wave relate to one another by equation 5.1:

$$V = \lambda f = dx/dt \quad (\text{Eq. 5.1})$$

Low frequencies possess longer wavelengths, which because of per wave cycle attenuation effects, enable the waves to travel farther; however, long wavelengths cannot detect small defects in a tested medium. The attenuation of P- and S-waves depend on the nature of the material and, in particular, on the matrix framework, pores, and cracks the sample's interior. Attenuation is quite sensitive to the heterogeneity and pore density of the material because these inner spaces impede the path of the wave. Consequently, a material such as steel has less wave attenuation, and rocks (in particular, porous sandstones with fluids inside) possess higher attenuation in

comparison. Porous materials also display high refraction due to the heterogeneity of their inner structure. When an incoming wave interacts with the boundary of two different materials the wave splits in form. One part is reflected and the other transmitted on different angle.

Ultrasonic acoustic study is a non-destructive standard test to determine the dynamic properties of the materials. It is usually conducted using a pair of transducers, as discussed in previous chapters. A source transducer emits an ultrasonic wave and the receiver transducer records the emitted wave after it passes through the sample. Based on the diameter of the piezoelectric crystal inside the transducers, the recorded velocity can be considered as the average signal which arrives to the surface of the piezoelectric receiver transducer. With that in mind, we are dealing with an averaged value over a small surface area (usually in a circle shape with a diameter equal than or greater than 10 mm). In contrast to this spatial averaging, laser point as a receiver of a wave covers a much smaller area and gives us great flexibility to monitor more points on the surface of the sample to measure precise direct displacement. To investigate this method, sets of individual experiments were designed and conducted on the surface of a transducer and representative samples. By calculating average of the recorded waveforms and comparing this with measurements recorded using a standard pair of the transducers we can ascertain whether the data is accountable for further investigations (with the purpose of local investigations). If the average wavelet by LDI on random points equals the standard wavelet recorded by transducer that would give us this capability to measure the velocity on a much smaller area. This means that defects, pores and anisotropy can be measured on a much smaller scale. This technique can further be useful for investigating internal structures and measuring the changes in scale over structure's life span.

The detection of pores and discontinuities is one of the capabilities of using a laser/ultrasonic method. Basically, these waves cannot pass through such spaces and the abnormality can be easily observed via attenuation and a change in the travel time. This change occurs because the first arriving propagating wave is travelling along on alternative path around the pores instead of passing through them.

For engineered material, when the base velocity of the medium is known (before applying loads) then the velocity can be monitored in the course of the life span on that structure. Any change in the velocity or waveform indicates the inner structure deformation or the creation of new voids as a result of inner compression, tension or torsion. For natural in-situ geo-materials, the velocities measured in the field are normally higher than those measured in a lab under lower stress. The variation in velocities at different pressures gives invaluable information about the topology of the pores, and compliant cracks as these indicate a change in stress concentration inside the rocks. Often slowing in velocity from its original baseline value indicates the creation of new voids inside the medium's structure (McCann and Forde 2001).

The detection of discontinuities and new voids are key for the quality control of steel (ASTM Standard A388/ A388M-16a), concrete (ASTM Standard D6760-16) and rocks (Aydin 2015). The creation of new voids affects the strength of the material as stress propagates through the discontinuities, which weaken the boundaries and lead to the creation of fractures and eventual failure. Hydrostatic compaction results in a closing pores, which reduces the size of the voids and leads to greater densities in solid material. Such density increase causes faster wave velocities because the wave propagates through fewer gaps and pores.

Rock physical laboratory experiments are an important part of the study for elastic properties of the rocks to prove theoretical models and to calibrate seismic data (Bona et al. 2017). The elastic properties of rocks are computed by velocity measurements/estimation in different directions as a common laboratory procedure by ultrasonic piezoelectric transducers based on travel times (Vernik and Nur 1992; Allan et al. 2015). These transducers are larger than the dominant ultrasonic wavelength; consequently, this affects the waveform, amplitude and type of the velocity (i.e., a phase or a group velocity) (Bona et al. 2017). To make the lab results comparable to those of seismic fields we need to make the receivers as small possible. Laser Doppler Interferometry (LDI) is a well-known receiver for ultrasonic waves. It has a small surface monitor size of 0.2 mm^2 (laser-focused point), which is much smaller than a wavelength (in this study the wavelength of Gosford sandstone measured 3 mm) . As a receivers, LDI is superior to transducers because of the small diameter it covers on the surface of the sample. The mentioned area is much smaller than the wavelength of

a studied material. LDI measures the displacement of the surface particle (in the direction of a laser beam) and its small, focused points enable the results to be comparable to the results of the seismic fields.

The difference between the phase and group velocities in an anisotropic media is ambiguous. In general, the diameter of the source wave plays an important role in distinguishing between these two velocities. The smaller the pulser wave face diameter in comparison with sample length, the higher the possibility of group velocity measurement and, if not, it can be considered as the phase/wavefront velocity. However, it's quite hard to eliminate uncertainties due to limitations of source/receiver transducers (Dellinger and Vernik 1994; Vestrum 1994; Siggins and Dewhurst 2007, Lebedev et al. 2011). Receivers in the field are much smaller than the wavelength, and velocity-type detection and direction of polarisation are not much of the problem with the measured data; however, in the lab such a task is hard to undertake. To estimate the elastic anisotropy in the lab, the polarisation of waves and velocity is required (Dewangan and Grechka 2003). To follow the same calculation technique in the laboratory, LDI gives the smallest possible receiver in comparison with the wavelength.

5.4 Literature review

The Laser Doppler Interferometry technique has been used as a receiver for elastic waves in many past studies (Dainty 1975; Ennos 1978; Monchalin 1986; Monchalin et al. 1989; Scruby and Drain 1990; Jacquot and Fournier 2000; Lebedev et al. 2011; Nourifard and Lebedev 2018; Yurikov et al. 2019; Nourifard et al. 2019). Using this technique, the elastic properties of anisotropic materials have been measured (Guilbaud and Audoin 1999). Later, this technique was used to investigate the polarisation of shear waves (Pouet and Rasolofosaon 1990; Martin et al. 1994; Rasolofosaon and Yin 1996). Nishizawa et al. (1997) conducted a method using LDI to detect shear-wave in the lab, which included measuring the displacement caused by wave-induced deformation on the micro-scale inside the particles of the sample, and reached to the other surface of the sample on a small area. In this technique, P- and S-waves were distinguished by measurements in two independent directions. The projections of such records estimate the displacement of the perpendicular and parallel displacement with regards to the surface (Lebedev et al. 2011). To detect S-wave

measurements carried out in two directions, Bayo and Rasolofosaon (1996) tested and successfully demonstrated the measurement of particle-displacement by this method. Detection of S-wave polarisation using LDI was studied by Fukushima et al. (2003) in rock samples.

LDI measures the wave displacement and recovers the full wave field displacement vector by three independent measurements simultaneously collected at three different angles. By producing a displacement vector we can follow the particle motion to pick the precise travel time based on propagation directions (Martin et al. 1992, 1994; Guilbaud and Audoin 1999; Lebedev et al. 2011; Shragge et al. 2015; Bona et al. 2017). The measurement of the particle velocity and displacement by LDI can be determined because of the phase shift between the frequencies of the incident and the reflective light (Lebedev et al. 2011). The source of ultrasonic waves for such an experiment is usually the standard piezoelectric transducers, which creates uncertainty in the associated velocity type (ray or phase velocity). The complication of recording ray velocity (which is mostly the case in small dimension lab experiments) is that no exact analytic expression is yet available to describe the dependency of ray velocities in the ray direction (Bona et al. 2017). The current approximations are limited to VTI mediums, mainly by Golikov and Stovas (2012) and Asgharzadeh et al. (2014), yet they are not accurate for different ranges of offsets. Bona et al. (2017) addressed the issue by numerically computing the exact ray velocities for a given measurement direction and using them for the inversion of the elasticity parameters. An experimental study by Lebedev et al. (2011) estimated the elastic properties using the mentioned approach for the anisotropic sample; however, the experimental set up in their study was based on near offsets to invert the measured travel times using numerically computed ray velocities. To overcome the near offsets limitation, which may reduce the accuracy of the inversion in current research, we utilised larger offsets as well.

In this chapter, we explain our experimental set-up, followed by an analysis of the three components of the recorded displacement at the surface near and far offsets of the sample to directly measure the surface displacement as a result of an ultrasonic wave passing through the sample.

5.5 Method and material

Data acquisition units for this experiment contain a Laser Doppler Interferometer (LDI) and the vibrometer, an oscilloscope, an electric pulser and a pair of S-transducers responsible for transmitting and receiving ultrasonic waves. The source S-wave transducer embodies a piezoelectric (PZT) crystal, which vibrates at a pre-determined frequency of central 1 MHz. This crystal produces a mechanical pulse when stimulated by an electric signal. The source transducer generates the vibration of an elastic wave, which propagates through the sample. Located on the other side of the sample is the receiver transducer, which receives the propagated wave and sends it to an oscilloscope for display and recording. We designed the experiment based on the transmission–receiver technique; however, our receiver is the LDI which sends the received signal to the oscilloscope for further analysis.

During the experiment, an electric pulse is generated and sent to the source transducer. The source transducer then creates an elastic ultrasonic wave, which travels directly through to the opposite face of the sample to where the source is attached. The ultrasonic wave propagates through the medium. Ultrasonic waves go through framework matrix, pores and cracks inside the sample, and the ultrasonic wave travels through specific sample regions of that particular path arrives at the other end of the sample and is recorded at the receiving transducer. The received ultrasonic vibration creates an electric signal, which needs to be amplified for better detection. The received wave goes to an amplifier to enhance the power and gain of the electrical signal after it gets to the receiver. When we apply the amplifier effect on the received wave we improve the signal clarity, but at the same time we are amplifying the noise in the waveform. Therefore, setting a careful threshold – especially when dealing with sensitive, Laser-recorded signal – is an important task for this experiment. In the final stage, the outcome wave can be displayed by oscilloscope and recorded for processing. The ultimate goal of the LDI test is to obtain the time of first arrival of P- and S-waves to compare to the standard transducer test, and to record the clear ultrasonic wavelets to convert into displacement to monitor the response of the sample once subjected to ultrasonic impact. This technique enables us to record more wavelets on the surface of the sample by comparison to the size-limited conventional transducers, which record only one wavelet over a significantly larger area. A Gosford sandstone 50 mm sample

was prepared for this experiment. The specifications of the tested sample are listed in Table 5-1.

<i>Properties</i>	<i>Value</i>
<i>Porosity</i>	13 ± 1.7%
<i>Bulk density</i>	1800 ± 20 kg/m ³
<i>Grain density</i>	2590 ± 30 kg/m ³
<i>Permeability on bedding (waterflow)</i>	350 ± 70 × 10 ⁻¹⁵ m ²
<i>Permeability perpendicular to bedding</i>	200 ± 30 × 10 ⁻¹⁵ m ²
<i>Young's modulus (dry)</i>	4.6 ± 0.7 GPa
<i>Mineralogy</i> (the range of volumetric fraction and mean value is given)	Quartz 26–44% (30%), Felspar 13–26% (18%), Detrital clays (mainly illite) 3–29% (12%), Mica 0–7% (2%), Heavy minerals <3%

Table 5-1 Average elastic properties and mineralogical content of the LDI tested Gosford sandstone.

5.5.1 Sample preparation

For laser experiments, the most important aspect of sample preparation is to reduce any extra (unwanted) angles, which can affect the axis matrix transformation. This is necessary to create parallel faces for the sample, and cubic sample geometry makes it easier to fulfil this requirement. Reducing the surface roughness is another important factor to be taken into consideration. Studies by Nagy et al. 1987 and Nagy and Adler (1988), emphasise the fact that increasing surface roughness increases signal attenuation. A diamond polish machines with an accuracy of 0.3 mm is recommended to treat rougher profiles, such as sandstones.

Moreover, the standard time of flight protocol from the International Society of Rock Mechanics (ISRM) states that sample preparation requires test specimens with smooth, flat, and parallel faces. In the current experiment the sample surface was polished and covered with epoxy resin to create a smooth surface for better contact. The front surface of the sample was divided into 17 measurement points, each on an equal radial distance from the centre point, called inner and outer orbits. The inner orbit indicates

the same piezoelectric size of the attached transducer at the bottom side of the sample, and the outer orbit is the measurement on the offset nearly two times farther than the crystal size. *Figure 5-1* demonstrates the preparation of the Gosford sample, the position of the bottom transducer, and the measurement points on the orbits towards the centre point. For the connection between the transducer and the sample, a layer of couplant is often applied to ensure efficient energy transfer between the transducers and the sample. There is a large variety of couplant options, including grease, glycerin, putty, Vaseline, and oil (Aydin, 2015). Although a gel couplant is normally used during testing to improve energy transmission, it may also cause shear movement when low or no pressure is involved. Instead of such a couplant, we used a superglue to permanently attach the S-wave transducer to the bottom of the sample and, at the end of the experiment when the sample was no longer used, we submerged the sample and transducer in acetone; after 48 hrs the transducer could be removed.

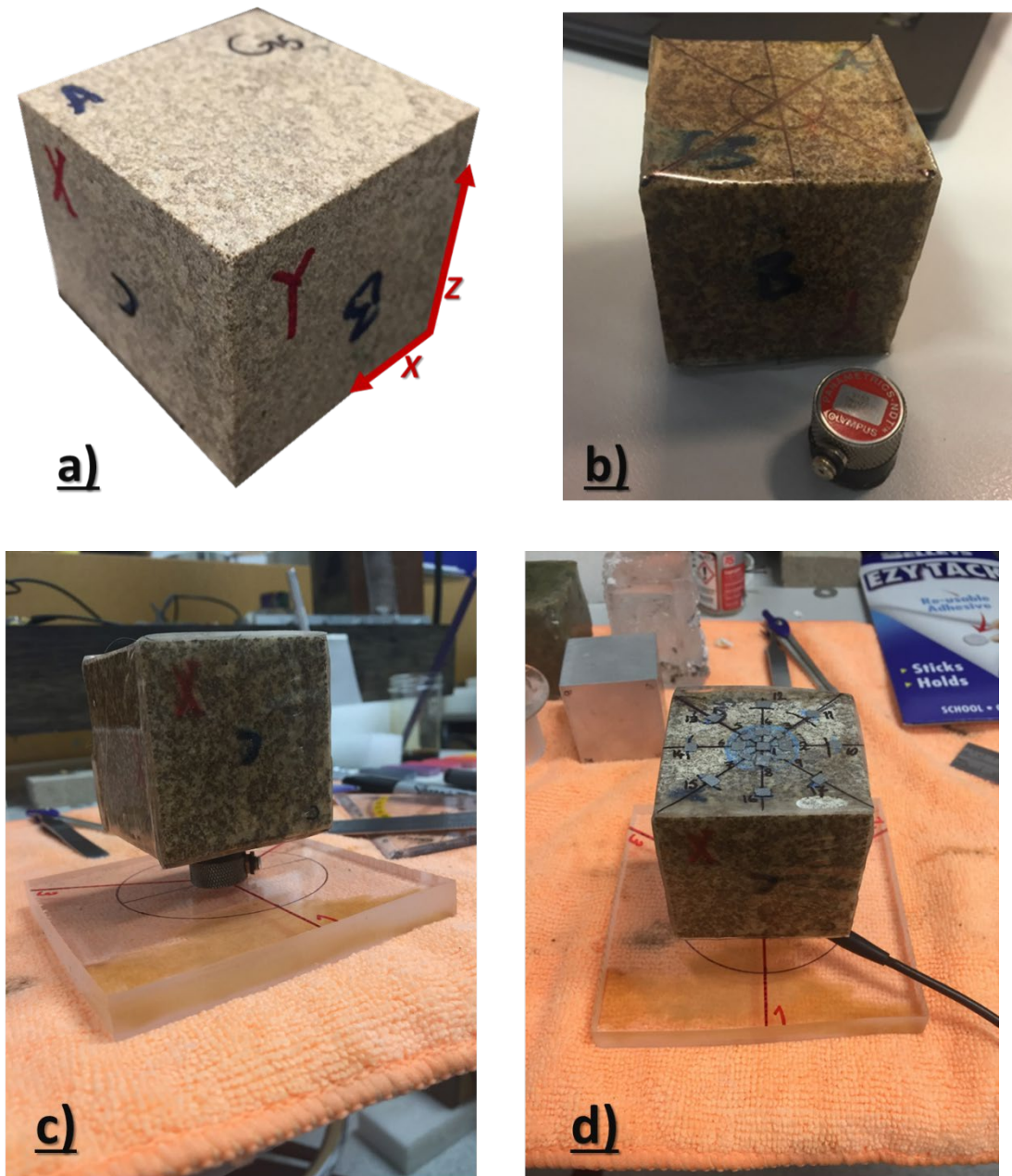


Figure 5-1 a) Cubic cut of 50mm Gosford sandstone, b) surface treatment with a layer of smooth epoxy resin. The measurement points have been marked on the sample for laser points with regards to the location of source transducer, c) the location of the bottom (source) S-wave transducer and the attachment to the rotational top plate, and d) 17 surface measurement points for the LDI device on the Gosford sample.

5.5.2 Experimental set-up

The experimental set-up was modified from that described in the work of Lebedev et al. (2011). The LDI experiments employed laser equipment and ultrasonic facilities (Figure 3-1 and Figure 5-2). To determine the body-wave velocities the ultrasonic pulse

transmission technique was used on the following samples: Polymethylmethacrylate (PMMA), Gosford sandstone, and Aluminium. The ultrasonic system included of a pair of S-wave transducers with a nominal centre frequency of 1 MHz to generate and detect P- and S-waves, 5077PR Pulser and Receiver units (Panametrics-Olympus), and a digital oscilloscope Tektronix TDS 2022C (200MHz). The Laser Doppler Interferometry set up contains a Vibrometer OFV-5000 Modular, Vibrometer Controller, Vibrometer Sensor Head OFV-503 (Politec Ltd.), and noise-cancelling platform (*Figure 5-2*). Equipment was synchronised by a 5077PR pulser–receiver. For each medium, the transmitter–receiver configuration was fixed to the centre of the cube surface. The pulser frequency was on dominant 1 MHz. The vibrometer OFV-5000 and the sensor head OFV-503 (Politec Ltd) measured the displacement of the particle on the surface of the sample on first arrival of the ultrasonic waves. Displacement measurements were carried out for three different directions to calculate three components of each measured point (*Figure 5-3* and *Figure 5-4*).

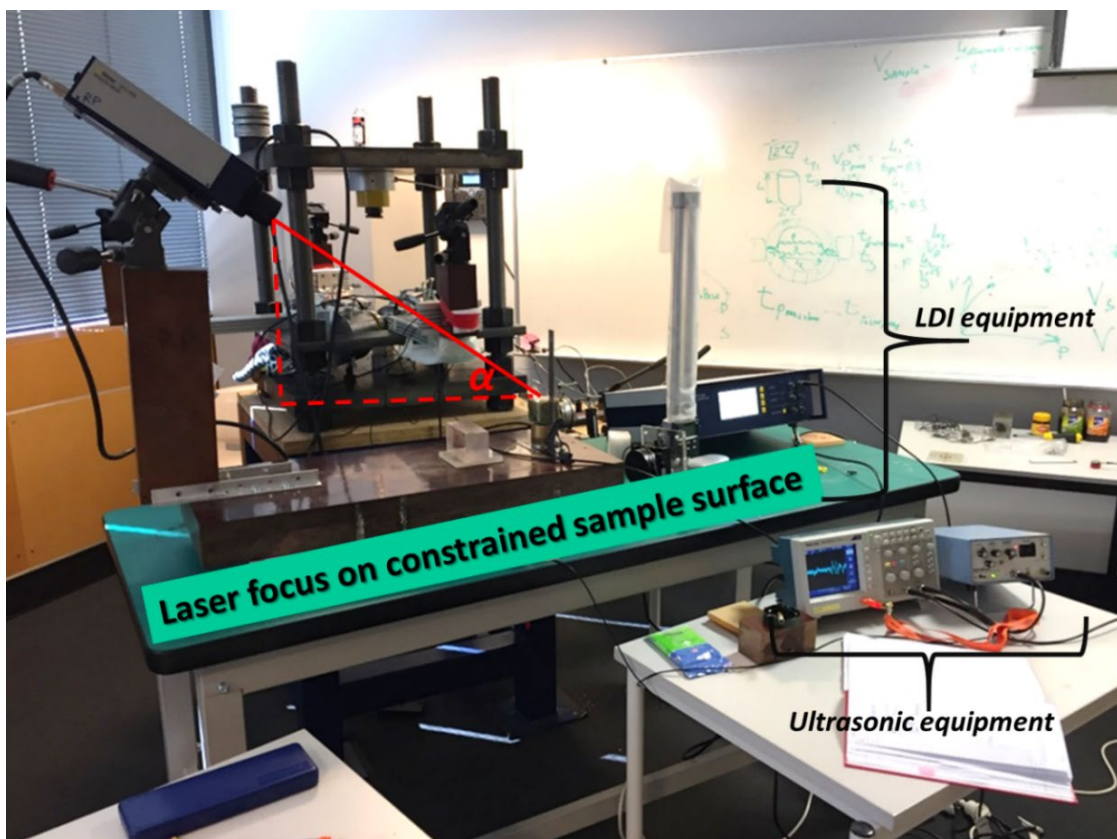


Figure 5-2 Layout of the experimental set-up consisting of LDI and ultrasonic equipment. The LDI laser beam was fixed at α for all the measured points in all directions.

The precise behaviour of any experimental system itself should be well established before conducting tests, and should be reviewed when a new experiment is proposed. Since we are keen to get the precise time of the first arrival for the sample, we should first ask: has the system deadtime (or the time delay) been corrected for the tested sample. Depending on the type and diameter of the transducer, the deadtime can be different. It was recorded from 180 to 320 ns for different kinds of P- and S-wave transducers; however, with the LDI as the receiver, this deadtime is significantly larger as the electronic recording system is more complicated. The calibration test in that regard consists of the direct contact between two source and receiver transducers (in this case 15 mm in diameter S-wave transducers), and for laser deadtime we put the laser beam directly on the surface of the transducer and measured the first break as the deadtime of the system (*Figure 5-3*). The recorded delay in time is called the “machine dead-time”. This delay in time will later be eliminated from all the recordings of wavelets of the samples. The recorded LDI dead-time at all three directions of X_1 , X_2 and X_3 shows 3.9 μs time delay for electronics (The dead-time is 0.3 μs for transducer on transducer for this experiment).

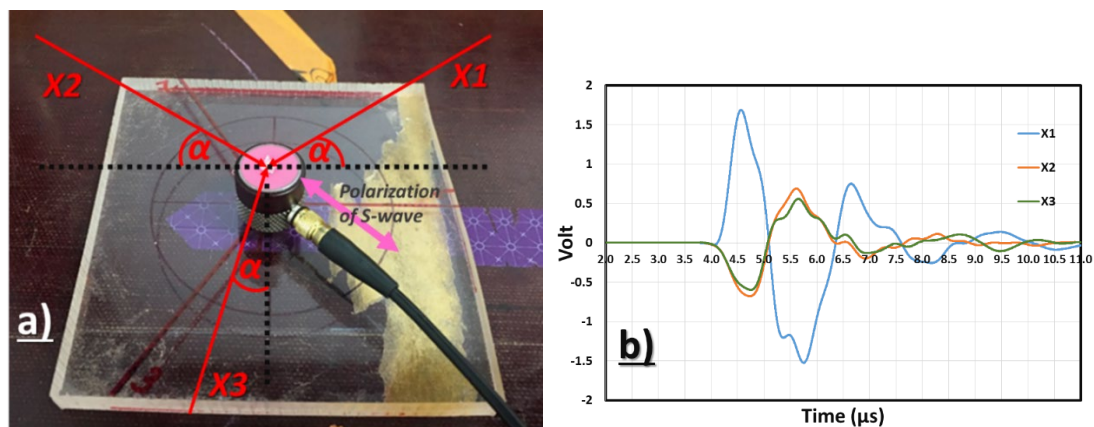


Figure 5-3 a) Free surface of the source S-wave transducer monitored by LDI to measure the raw wavelets in three directions (each 120 degrees apart and marked by the red rigid line). α is the incident angle of the laser beam collinear to the surface (horizontal surface marked by dotted black line), α kept at fixed angle for X_1 , X_2 and X_3 at 46 degrees. X_1 , X_2 and X_3 are apart from one another by 120 degrees, and, b) the raw waveform before processing to calculate the displacement. The first arrival of these three wavelets (3.9 μs) is also the indication of system dead-time and will be used to correct the time of first arrival once the sample is attached to the source transducer.

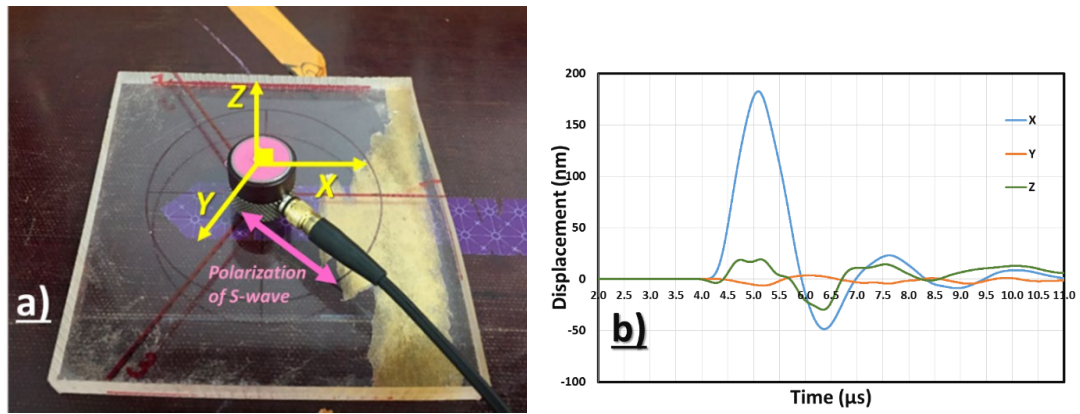


Figure 5-4 a) The particle displacement on the free surface of the source S-wave transducer, which has been calculated from LDI raw wavelets and by matrix transformation converted to the Cartesian coordinate system of X,Y, and Z. b) Calculated displacement in three Cartesian coordinate system as the indication of particle displacement in nanometres on the surface of the free transducer. This S-wave transducer will later be attached to the bottom of the sample as the source of ultrasonic wave.

5.5.3 Experimental procedure

To measure the surface displacement, we conducted the test on a cube of Gosford sandstone measuring 50 mm x 50 mm x 50 mm. An S-wave transducer able to produce both P- and S-waves was glued on a diagonal to the X and Y axis at the bottom of the sample by superglue for the best possible contact (*Figure 5-1*). A small weight of 3.5 kg was placed on the top of the sample with an open middle area equal to the outer orbit of the measurements for better coupling for noise control. The entire set-up was placed on the optical desk to eliminate environmental vibrations. *Table 5-2* summarises the normal laboratory testing conditions for this experiment, based on ASTM.

To record the three components of the particle on the top surface of the sample, three equal directions (each 120 degrees apart) were marked on the rotational plate attached at the bottom of the source transducer, which was placed on the optical desk. This plate enabled precise rotation for each point on the surface of the sample. Once the free surface of the transducer was measured, the transducer was attached at the bottom of the sample and the same procedure of measuring three components on marked points on the surface of the sample was measured by LDI. The incident angle of laser beam (α) remains the same for all the recordings at 46 degrees. Three recorded wavelets of X_1 , X_2 and X_3 were then rotated and went through matrix transformation to a Cartesian

coordinate system (X, Y, and Z). The evolution of raw wavelets to displacement in the Cartesian coordinate system is plotted in *Figure 5-3* and *Figure 5-4*.

We performed the measurements of the velocity using LDI and piezoelectric transducer as receiver. Waveforms were then recorded by a digital oscilloscope (TDS3001, Tektronix). The first step was to measure the first arrival using LDI on all 17 points on the surface of the sample on the inner and outer orbit (*Figure 5-5*). The average velocity over these points by LDI was then calculated for the inner and outer orbits. Then, we glued the receiver (second transducer) on the position of inner orbit at the top surface of the sample and measured the average velocity for comparison with the ones with the averaging laser. We can see that the velocities measured by both methods are identical for Gosford sandstone. The polarisations and the recorded wavelets are also identical for the transducer-recorded raw wavelet and axis X_3 of the LDI averaging raw data. The results are in agreement with our previous studies (Nourifard and Lebedev 2018; Yurikov et al. 2019) that shows the transducer measures the “average” arrival of the wave over a large area, and LDI measures the local velocity of a small surface area (0.3 mm); by obtaining the averaging of such measurement points, the results resemble the transducer sensor results. This initial result confirms the viability of the proposed method, which can be used even for offset measurement (“outer orbit”).

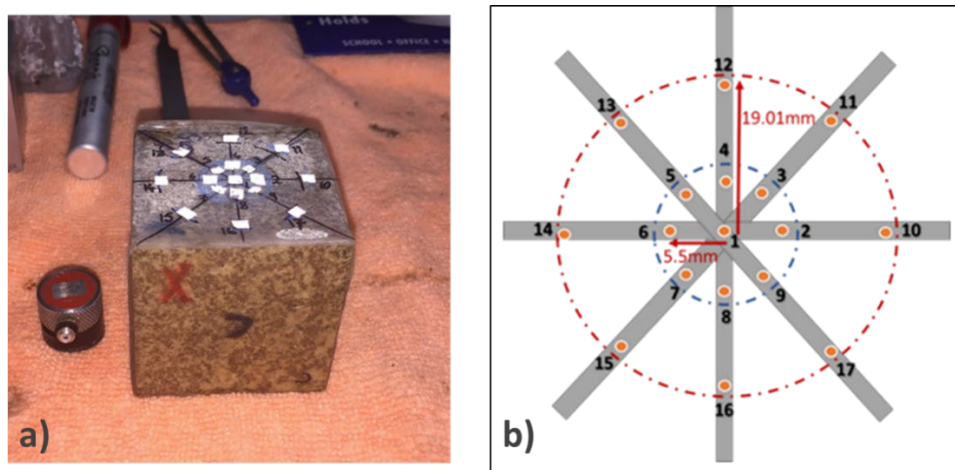


Figure 5-5 (a and b) Seventeen measurement points on the sample face of the Gosford sandstone divided into two orbits: inner orbit, representative of the area with the same diameter as the ceramic piezoelectric ceramics disk of the source transducer, and outer orbit, the area at the far edges of the source transducer zone on the opposite face of the sample.

<i>Parameter</i>	<i>Standard</i>
<i>Sample geometry</i>	Smooth, flat and parallel faces
<i>Coupling medium</i>	Application of superglue between transducer and sample
<i>Coupling stress</i>	Small stress for a given transducer diameter
<i>Transducer alignment</i>	Normal to both faces
<i>Moisture content</i>	Either dry or fully saturated
<i>Wave travel distance</i>	10X the average grain size

Table 5-2 Normal Laboratory Testing Conditions (After Aydin, 2015; ASTM Standard D2845-08).

5.6 Results and discussion

5.6.1 Raw waveform comparison between LDI points and a pair of S-wave transducers

To compare the first arrivals register by LDI with the same from the pair of transducers, we measured the same centre point of the Gosford sample using a pair of 15 mm 1 MHz S-wave transducers. The location of the receiver transducer on the top surface of the sample was precisely marked and measured to make sure both source and receiver transducers were exactly collinear on the opposite faces. This step happens after the 17 points have been measured by laser in the inner and outer orbits. The inner orbit of nine laser points was marked on the transducer zone, and the raw waveform of the three component (3C) measurement of each of the nine inner points was recorded. The averaging of nine wavelets demonstrated a great resemblance to the raw wavelet recorded by a pair of standard S-wave transducers, as shown in Figure 5-6. The first arrival of P-waves were recorded the same as each other, while for S-wave raw wavelet recorded by LDI, only one axis of each showed great resemblance to the original S-wave recorded by the transducer. We expected such behaviour, as S-waves propagate in two motions of X and Y directions and among the independent axes of X_1 , X_2 and X_3 only one can be a good match based on the S-wave polarisation. This comparative study showed that using LDI as a receiver instead of a pair of transducers

can still register a reliable waveform, which can measure even smaller events through the sample for detailed study. This enables us to have more flexibility over the choosing of random points either in the transducer zone or offset. *Figure 5-6* illustrates the resemblance of wave averaging by LDI to wavelets recorded by a pair of S-wave transducers.

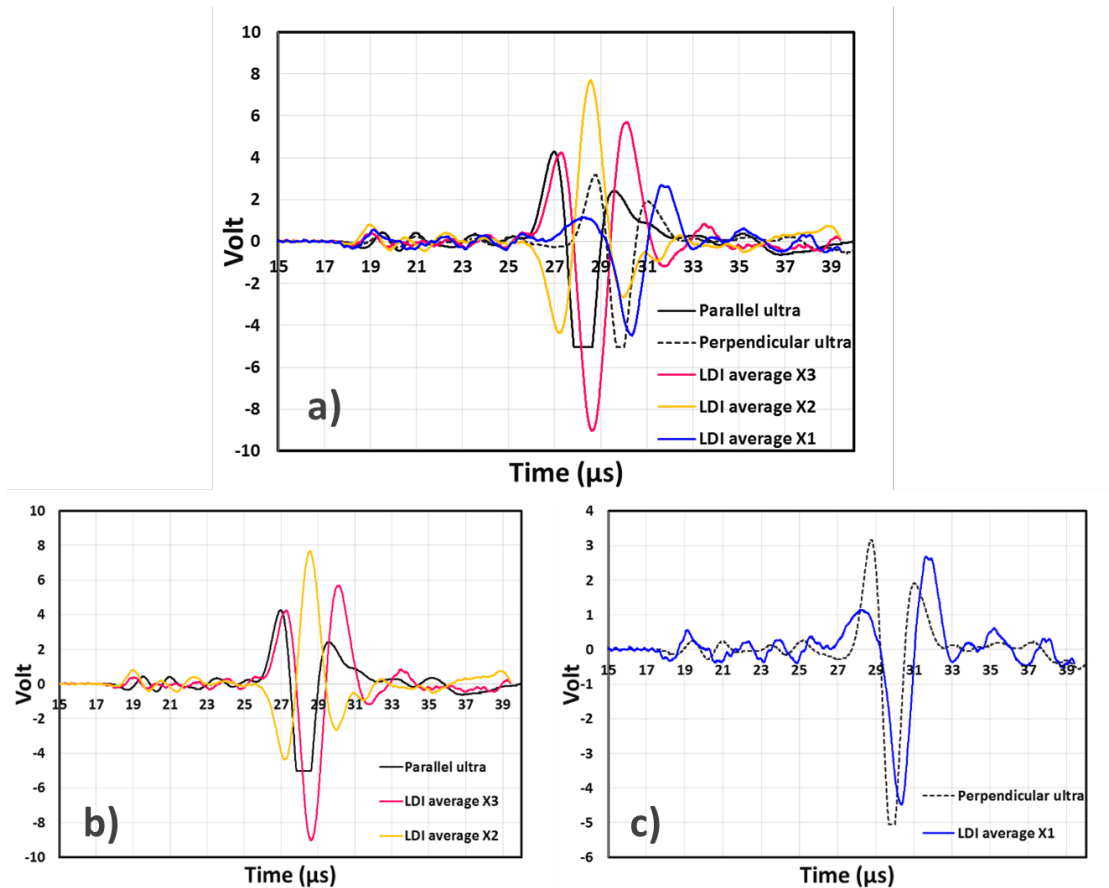


Figure 5-6 (a) Averaging of LDI raw waveforms in three individual directions (3C measurement) vs raw waveform recorded by ultrasonic transducer measurement. (b and c) X₂ and X₃ measurement can be compared with parallel S-wave polarisation conducted by a pair of transducers, and X₁ is comparable with perpendicular polarisation of S-waves for a pair of S-wave transducers.

5.6.2 Shift of the P-wave polarisation of wavelets on half of the monitored area

Mapping the recorded wavelets on the 17 points of the sample demonstrated that the first break of the recorded wave – which corresponded to the P-wave recorded by the S-transducer – did not have identical behaviour for all points on the measured area. In other words, based on the polarisation of the S-wave transducer, the recorded P-wave first arrival possesses positive and negative poles. These results are in agreement with

the study by Yurikov et Al. (2019), which studied the bi-polarity of the P-wave produced by S-wave transducers. *Figure 5-7* illustrates the change of P-wave polarity on the measured points by LDI.

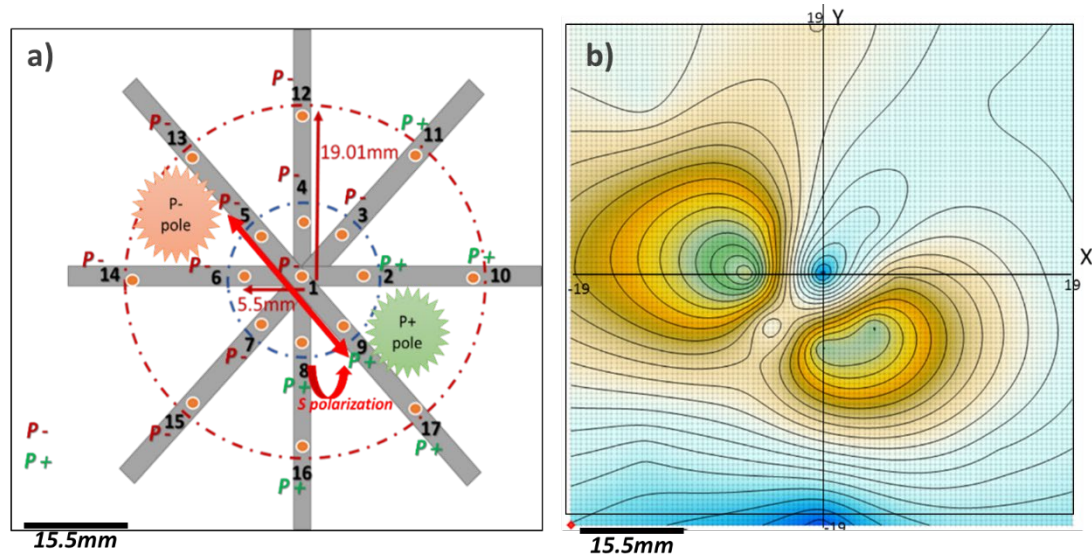


Figure 5-7 (a and b) The recorded raw wavelets showing positive and negative P-poles of the source transducer

5.6.3 Displacement caused by Shear-Wave Polarisation

In a homogeneous isotropic medium, compressional and shear waves are linearly polarised parallel with and perpendicular to the propagating direction respectively, if the wave source is pure compression or pure shear. However, in a heterogeneous medium, particle motions are distorted, and polarisations deviate from linear motions. Wave distortion can be characterised by tracing the trajectory of particle motions and determining the shape of the particle-motion spheroids.

Several studies have been performed to investigate the underground scattering properties by analysing the particle motions of seismic waves (Sato and Matsumura 1980; Matsumura 1981; Nishizawa et al. 1983; Nishimura 1996). It is interesting to compare the distortion of shear-wave particle motions and the characteristics of random heterogeneities. *Figure 10* shows the particle motions of the direct shear wave portion in the X and Y plane at for all the 17 points. Since the X and Y directions are the polarisation directions of the source, these directions are registered for the particle motion caused by the S-wave, and the recorded Z displacement can be interpreted as

the recording of the produced P-wave as the by-product of the propagating S-wave through the medium. The surface particle motion in all three principle axes gradually decreases and vanishes once it reaches to offset and the edges of the sample (outer orbit), when the energy of ultrasonic wave dispersal is based on a longer distance. *Figure 5-8, Figure 5-9, and Figure 5-10* plot the particle displacement in X, Y and Z directions based on the 17 measured points on the surface of the Gosford sample.

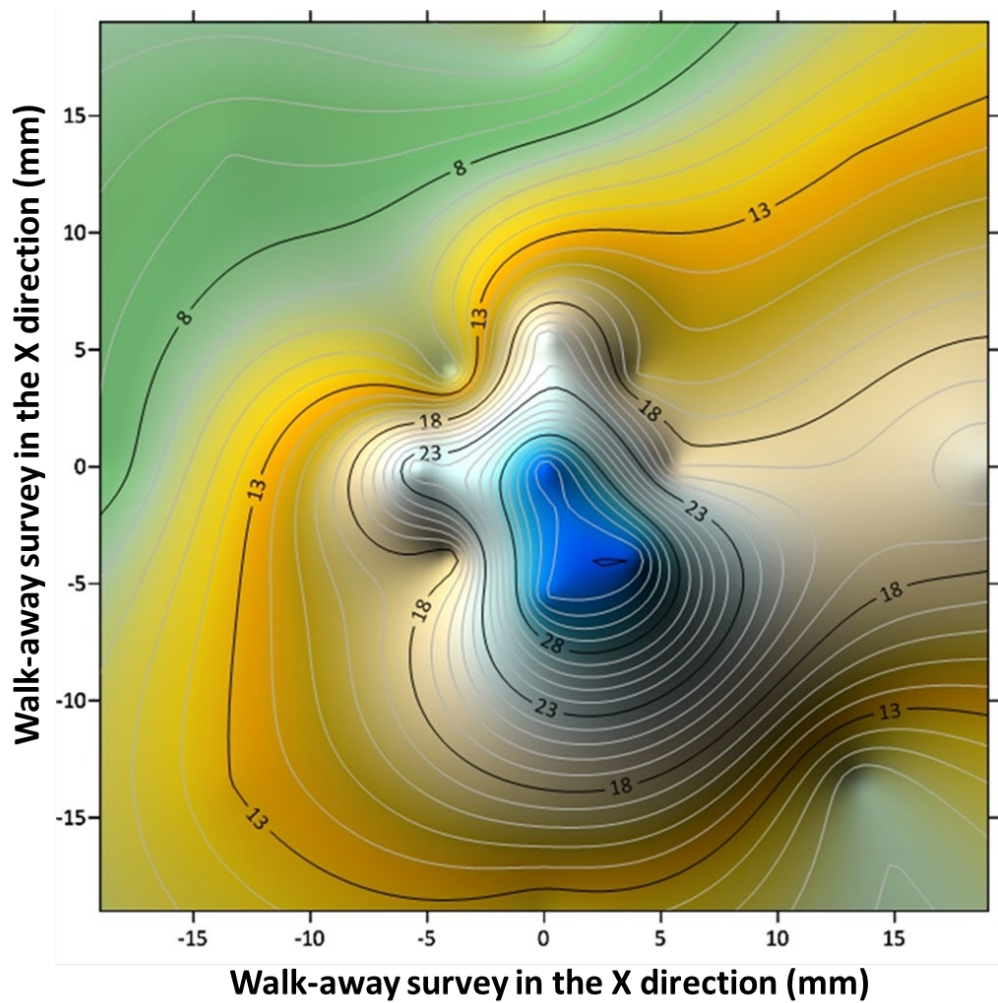


Figure 5-8 The shaded recorded interpolated displacement (Kriging interpolation) of the S-wave transducer in the X axis on the surface of cubic Gosford sandstone (the counter values are in nanometres). The location of measuring points are shown in Figure 5-7.

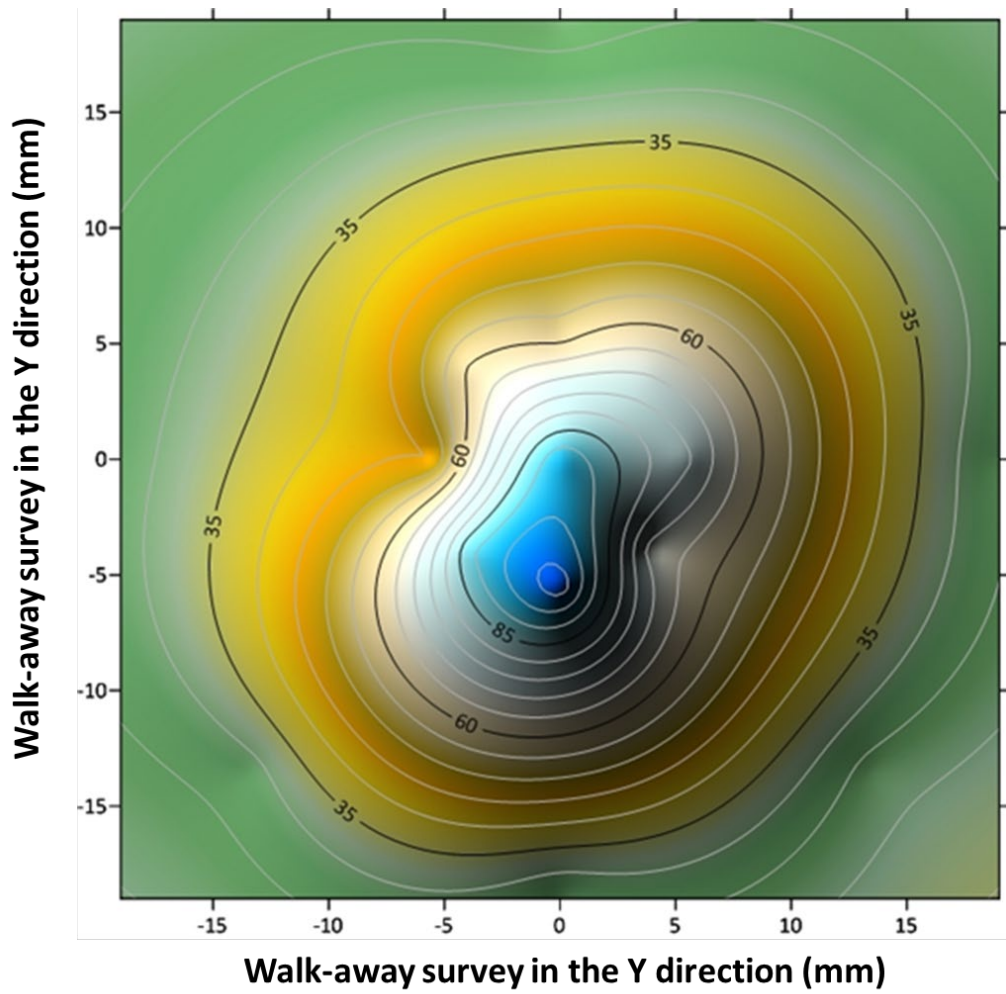


Figure 5-9 The shaded recorded interpolated displacement by the S-wave transducer in the Y axis on the surface of cubic Gosford sandstone (the counter values are in nanometres) The location of measuring points are mapped in Figure 5-7.

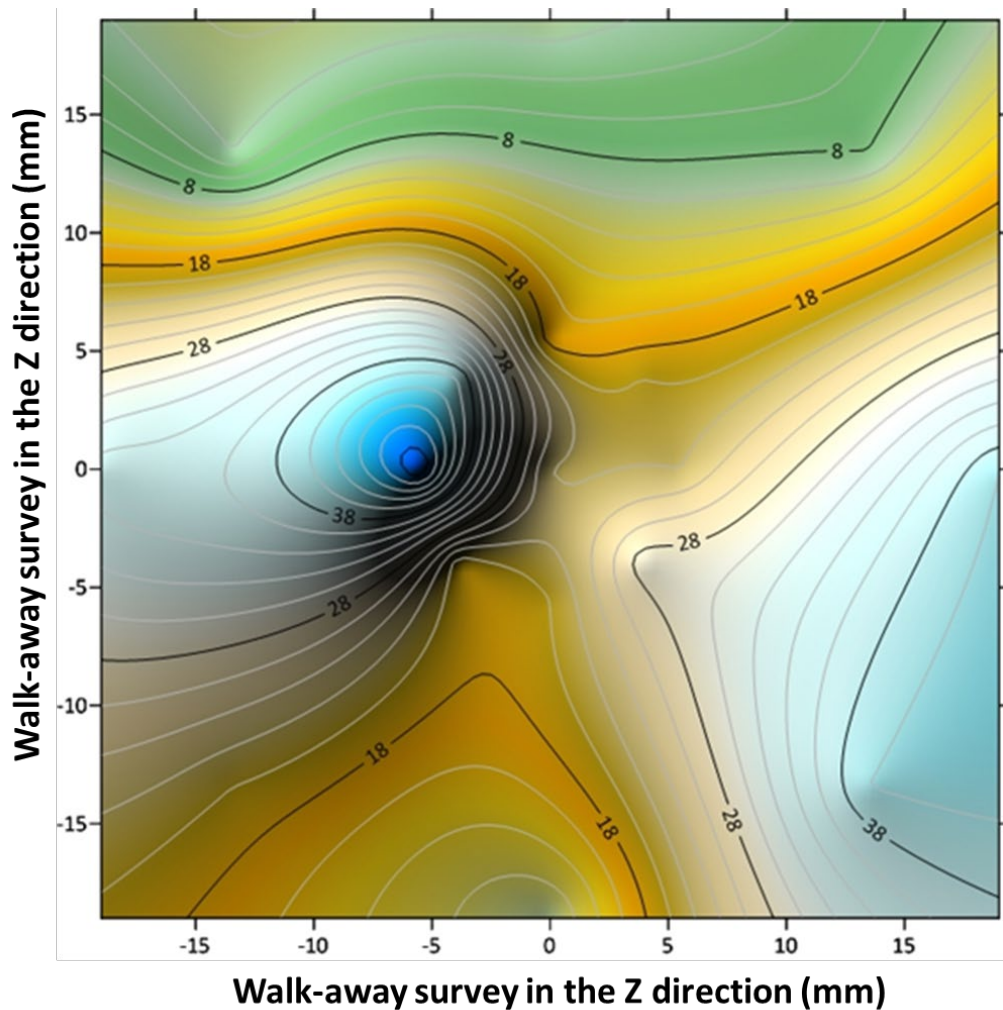


Figure 5-10 The shaded recorded interpolated displacement by the S-wave transducer in the Z axis on the surface of cubic Gosford sandstone (the counter values are in nanometres). The location of measuring points are mapped in Figure 5-7.

5.7 Conclusion and recommendations

Laser Doppler Interferometry (LDI) can record ultrasonic elastic wave propagation and is an advanced and emerging technique in rock physics (Adam et al. 2014, Shragge et al. 2015, Hitchman et al. 2015). Up until now it was believed that a laser could measure the displacement of an acoustic wave, and when it comes to measuring precise velocity it was believed that the results obtained by a laser do not have enough accuracy. We investigated increasing the displacement spatial resolution by increasing the number of laser measurements in an area comparable to the source of the ultrasonic wave, and by averaging the recorded wavelets the first arrivals possess enough accuracy to be compared with the results of the conventional technique using

transducers. LDI enables us to perform the measurement over a small area of the sample for precise investigation of the acoustic behaviour of the sample. It helps to detect any local defects inside the sample in a much smaller area and can result in better insights.

The velocity of ultrasonic waves can be used to qualitatively determine the internal structure of a sample as well as provide empirical estimations for mechanical properties such as compressive strength. LDI experiments can be conducted on any specimen without limitations on shape or dimensions as long as the test can provide a distinguishable waveform. The roughness of the sample surface is the only concern, which can be resolved by careful machine diamond polish, even for porous materials such as sandstones. Further research is required to assess LDI's ability to investigate dynamic modulus at variations of stress, where the system is exposed to the noise created by the micro-events inside the sample while subjected to stress. This topic can benefit both the rock-physics and the rock-mechanics community in the future.

5.8 References to Chapter Five

Adam, L., Ou, F., Strachan, L., Johnson, J., Wijk, K.V. & Field, B. 2014. Mudstone P-wave anisotropy measurements with non-contacting lasers under confining pressure. SEG Technical Program Expanded Abstracts 2014. <https://doi.org/10.1190/segam2014-0999.1>.

Allan, A. M., Kanitpanyacharoen, W. & Vanorio, T. 2015. A multi-scale methodology for the analysis of velocity anisotropy in organic-rich shale: *Geophysics*, 80, no. 4, C73–C88, doi: 10.1190/geo2014-0192.

Asgharzadeh, M., Nadri, D. & Bóna, A. 2014. Inversion based accuracy comparison of non-hyperbolic moveout approximations for P-waves in VTI media: 76th Conference and Exhibition, EAGE, Extended Abstracts, 1–4.

Aydin, A. 2014. Upgraded ISRM suggested method for determining sound velocity by ultrasonic pulse transmission technique. *Rock Mechanics and Rock Engineering* 47, 255–259.

Bayo, A., Rasolofosaon, P. N. J. 1996. Three-Component Recording of Ultrasonic

Transient Vibration by Optical Heterodyne Interferometry. Multicomponent Recording, and B Y Speckle. 99 (2): 954–61. <https://doi.org/10.1121/1.414623>.

Bóna, A., Lebedev, M., Pevzner, R., Gurevich, B. & Madadi, M. 2017. Estimation of elastic anisotropy from three-component ultrasonic measurements using laser Doppler interferometry, *Exploration Geophysics* <https://doi.org/10.1071/EG16156>.

Dainty, J.C. 1975. *Laser Speckle and Related Phenomena*. Vol. 9. Topics in Applied Physics. Berlin, Heidelberg: Springer Berlin Heidelberg. <https://doi.org/10.1007/BFb0111434>.

Dellinger, J., and L. Vernik, 1994, Do traveltimes in pulse-transmission experiments yield anisotropic group or phase velocities?: *Geophysics*, 59, 1774–1779, doi:10.1190/1.1443564.

Dewangan, P. & Grechka, V .2003. Inversion of multi-component, multi-azimuth, walk-away VSP data for the stiffness tensor: *Geophysics*,68,1022–1031, doi:10.1190/1.1581073.

Ennos, A.E. 1978. IV Speckle Interferometry. *Progress in Optics* 16 (January): 233–88. [https://doi.org/10.1016/S0079-6638\(08\)70073-8](https://doi.org/10.1016/S0079-6638(08)70073-8).

Fukushima, Y., Nishizawa, O., Sato, H. & Ohtake, M. 2003. Laboratory Study on Scattering Characteristics of Shear Waves in Rock Samples. *Bull Seismol Soc Am* 93 (1): 253–63.

Golikov, P. & Stovas, A. 2012. Accuracy comparison of nonhyperbolic moveout approximations for qP-waves in VTI media. *Journal of Geophysics and Engineering*, 9, 428-432.

Guilbaud, S. & Audoin, B.1999. Measurement of the stiffness coefficients of a viscoelastic composite material with laser-generated and detected ultrasound: *The Journal of the Acoustical Society of America*, 105, 2226–2235.

Hitchman, S., Wijk, K.V., Broderick, N. & Adam, L. 2015. Heterodyne interferometry for the detection of elastic waves: a tutorial and open-hardware project. *European Journal of Physics* 36(3) DOI: 10.1088/0143-0807/36/3/035011.

- Jacouot, P. & Fournier, J. M. 2000. *Interferometry in Speckl Light - Theory and Applications*.
- Johnson, P. A., Zinszner, B. & Rasolofosoan, P. N. J. 1996. Resonance and elastic nonlinear phenomena in rock *J. Geophys. Res. B* 101 11553–64.
- Lebedev, M., Bona, A., Pevzner, R. & Gurevich, B. 2011. Elastic anisotropy estimation from laboratory measurements of velocity and polarization of quasi-P-waves using laser interferometry, *Geophysics*, 76, 3; P. WA83–WA89.
- Martin, D., Ehinger, A. & Rasolofosaon, P. N. J. 1992. Some aspects of seismic modeling and imaging in anisotropic media using laser ultrasonics: SEG Technical Program, Expanded Abstracts, 1373–1376.
- Martin, D., Rasolofosaon, P. N. J., Gascón, F., Bayón, A. & Varadé, A. 1994. Physical modeling of 3D seismic wave propagation, in K. Helbig, ed., *Modeling the earth for oil exploration*: Pergamon, 637–686.
- Mashinskii, E. I. 1994. Quasi-micro-plasticity processes and nonlinear seismicity *Phys. Solid Earth* 30 97–102.
- Mashinskii, E. I. 2004. Variants of the strain-amplitude dependence of elastic wave velocities in rocks under pressure *J. Geophys. Eng.* 1 295–306.
- Mashinskii, E.I. 2005. Experimental study of the amplitude effect on wave velocity and attenuation in consolidated rocks under confining pressure, *Journal of Geophysics and Engineering*, *J. Geophys. Eng.* 2 (2005) 199–212.
- Matsumura, S. 1981. Three-dimensional expression of seismic particle motions by the trajectory ellipsoid and its application to the seismic data observed in the Kanto district, Japan, *J. Phys. Earth* 29, 221– 239.
- McCann, D. & Forde, M. 2001. Review of NDT methods in the assessment of concrete and masonry structures. *NDT&E International*, 71- 84.
- Monchalín, J. P., Aussel, J. D., Héon, R. , Jen, C. K. , Boudreault, A. & Bernier, R. 1989. Measurement of In-Plane and out-of-Plane Ultrasonic Displacements by Optical Heterodyne Interferometry. *Journal of Nondestructive Evaluation* 8 (2): 121–33.

<https://doi.org/10.1007/BF00565636>.

Monchalin, J. P. 1986. Optical Detection of Ultrasound. *IEEE Transactions on Ultrasonics, Ferroelectrics, and Frequency Control* 33 (5): 485–99. <https://doi.org/10.1109/T-UFFC.1986.26860>.

Nagy, P. B., Rypien, D. V. & Adler, L. 1987. Ultrasonic attenuation measurement by backscattering analysis, in *Review of Progress in Quantitative Nondestructive Evaluation* (Springer, New York), Vol. 6A, pp. 1411–1418.

Nagy, P. B. & Adler, L. 1988. Scattering induced attenuation of ultrasonic backscattering, in *Review of Progress in Quantitative Nondestructive Evaluation* (Springer, New York), Vol. 7B, pp. 1263–1271.

Nishimura, T. 1996. Horizontal layered structure with heterogeneity beneath continents and island arcs from particle orbits of long-period P waves, *Geophys. J. Int.* 127, 773–782.

Nishizawa, O., Pearson, C. & Albright, J. 1983. Properties of seismic wave scattering around water injection well at Fenton Hill hot dry rock geothermal site, *Geophys. Res. Lett.* 10, 101–104.

Nishizawa, O., Satoh, T., Lei, X. & Kuwahara, Y. 1997. Laboratory Studies of Seismic Wave Propagation in Inhomogeneous Media Using a Laser Doppler Vibrometer. *Bulletin of the Seismological Society of America* 87 (4): 809–23. <http://www.bssaonline.org/content/87/4/809.short>.

Nourifard, N. & Lebedev, M. 2018. Research Note: The Effect of Strain Amplitude Produced by Ultrasonic Waves on Its Velocity. *Geophysical Prospecting*, 1–8. <https://doi.org/10.1111/1365-2478.12674>.

Nourifard, N., Mashinskii, E., Lebedev, M. 2019. The effect of wave amplitude on S-wave velocity in porous media: An experimental study by Laser Doppler Interferometry: *Exploration Geophysics*. DOI: 10.1080/08123985.2019.1667228.

Ostrovsky, L. A. & Johnson, P. A. 2001. Dynamic nonlinear elasticity in geomaterials *Riv. Nuovo Cimento* 24 7.

Pouet, B. & Rasolofosaon, P. N. J. 1990. Seismic Physical Modeling Using Laser Ultrasonics. 60th Ann. Internat. Mtg, no. January: 841–44. <https://doi.org/10.1190/1.1890357>.

Rasolofosaon, P. N. J. & Yin, H. 1996. Simultaneous characterization of anisotropy and non-linearity in arbitrary elastic media - Reflections on experimental data -, in Fjaer, E., Holt, R., Rathore, J. S., Eds., Seismic anisotropy: Society of Exploration Geophysicists, 141-179.

Sato, H. & Matsumura, S. 1980. Three-dimensional analysis of scattered P waves on the basis of the PP single isotropic scattering model, J. Phys. Earth 28, 521–530.

Scruby, C. B. & Drain, L. E. 1990. Laser Ultrasonics : Techniques and Applications. A. Hilger. <https://www.crcpress.com/Laser-Ultrasonics-Techniques-and-Applications/Scruby-Drain/p/book/9780750300506>.

Shragge, J., Blum, Th. E., Wijk, K. V. & Adam, L. 2015. Full-wavefield modeling and reverse time migration of laser ultrasound data: A feasibility study. Geophysics; 80 (6): D553–D563. doi: <https://doi.org/10.1190/geo2015-0020.1>.

Siggins, A. F. & Dewhurst, D. N. 2007. Ultrasonic determination of the elastic constants of VTI shale: Proceedings of the International Congress on Ultrasonics, 2007, Paper ID 1075, doi:10.3728/ICUltrasonics.

2007.

Ten Cate, J. A. & Shankland, T. J. 1996. Slow dynamics in the nonlinear elastic response Geophys. Res. Lett. 23 3019–22.

Thomas, W. E. 2017. Evaluation of Ultrasonic Velocity Tests to Characterize Extraterrestrial Rock Masses, Department of Mining Engineering, Morgantown, West Virginia.

Tutuncu, A. N., Podio, A. L. & Sharma, M. M. 1994. Strain amplitude and stress dependence of static moduli in sandstones and limestones Rock Mechanics: Models and Measurements. Challenges from Industry ed P Nelson and S Laubach (Rotterdam: Balkema) pp 489–96.

- Tutuncu, A. N., Podio, A. L., Gregory, A. R. & Sharma, M. M. 1998a. Nonlinear viscoelastic behavior of sedimentary rocks. Part I: effect of frequency and strain amplitude *Geophysics* 63 184–94.
- Tutuncu, A. N., Podio, A. L. & Sharma, M. M. 1998b. Nonlinear viscoelastic behavior of sedimentary rocks. Part II: hysteresis effect and influence of type of fluid on elastic moduli *Geophysics* 63 195–203.
- Van Den Abeele, K. E.A., Johnson, P. A. & Guyer, R. A. 1997. On the quasi-analytic treatment of hysteretic nonlinear response in elastic wave propagation *J. Acoust. Soc. Am.* 101 1885–98.
- Vernik, L. & Nur, A. 1992. Ultrasonic velocity and anisotropy of hydrocarbon source rocks: *Geophysics*, 57, 727–735, doi: 10.1190/1.1443286.
- Vestrum, R. W. 1994. Group and phase-velocity inversions for the general anisotropic stiffness tensor: M.S. thesis, University of Calgary.
- Winkler, K. W., & Nur, A. 1982. Seismic attenuation: Effects of pore fluids and frictional sliding, 18.83.7.105.
- Yurikov, A., Nourifard, N., Pervukhina, M. & Lebedev, M. 2019. Laboratory ultrasonic measurements: Shear transducers for compressional waves. The leading edge. 38 322–416. <https://doi.org/10.1190/tle38050392.1>.
- Zinszner, B., Johnson, P. A. & Rasolofosoan, P. N. J. 1997. Influence of change in physical state on elastic nonlinear response in rock: significance of effective pressure and water saturation *J. Geophys. Res. B* 102 8105–20.

Chapter 6 Conclusion

The research objective of this study was to better understand the behaviour of reservoir rocks subjected to stress by novel acoustic approaches. One of the difficulties of earlier experimental rock physics studies is they have not provided thorough meta-data about laboratory conditions, rates or, the system accuracies themselves. We decided not only to provide a well-planned experimental study, but also to document our data for future rock physicists to fully use the data. Natural phenomena like rocks remain an equation with no absolute solution to detect all the participating factors unless we validate the models with trusted data. Experimental science has great potential to add accuracy to models and mathematical equations if well conducted and well documented. To determine the underlying cause of velocity anisotropy, an experiment on a sample cannot be solely accurate unless we put that particular system to the test. Wave propagation patterns give invaluable insight about the inner structure of a medium. A well-planned test dictates some level of control over the original state of the tested material to follow one particular event at a time. Stress, strain, saturation degree, transmitted wave, and orientation of layers have always been rock physics control parameters; however, data from examining each parameter separately without the influence of another – also using new techniques – has not been gathered in a single publication before. An accurate conclusion on the sandstone's elastic properties relies on the experimental system itself being well studied.

6.1 Summary

We investigated the effect of strain amplitude on velocity, and this effect has not been considered in past experimental studies. Strains in the waves were measured by a Laser Doppler Interferometer (LDI) upon wave arrival on a free surface of the sample. The ultrasonic velocities were measured by a pair of P-wave and a pair of S-wave transducers located at the same measuring point as the laser beam of the LDI. The effect of strain on velocity varied for different materials. The velocities were calculated using both a first arrival and a first maximum peak at different applied voltage. For P-wave velocity our findings contradict past studies as we observed an increase in velocity of 0.8%. These results drew our attention to this phenomenon and we expanded our study for S-wave velocity. We observed that unlike P-waves, which increase while the strain amplitude increases inside the wave, S-waves decrease by

almost 5%. This result is in agreement with a couple of classic past studies. In all these studies, the strain amplitude was not directly measured in the lab; therefore, our findings have significance in that we measured this strain with no assumption and no estimation. As a result of this effect on the velocities of P- and S-waves, the dynamic elastic modulus is also influenced by strain amplitude. Our study documents the importance of considering strain amplitude for all rock physics experiments and consider this evaluation as an important calibration step for the system.

Applying stress variation on a medium affects the topology of the pores and micro-cracks in the following ways: It either close the pores and cracks (high hydrostatic stress) or creates secondary cracks as a result of anisotropy and non-uniform stress concentration. To study the effect of hydrostatic stress and uniaxial stress on the elastic moduli of the reservoir rocks, we deployed static and dynamic approaches simultaneously to monitor the changes while subjected to stress. The results show that the dynamic modulus is higher than the static modulus for porous media. In this study we highlighted the importance of measuring both S- and P-waves in estimating the dynamic elastic moduli. In classic studies, the S-wave was usually estimated by its P-wave because the process of picking S-wave first arrival for porous media is challenging. Our direct measurement for both P- and S-waves for dozens of sandstones shows that the rough estimation of S-wave from its P-wave is not always accurate, and the V_p/V_s ratio does not necessarily obey the classic ratio of 1.5 – especially for porous materials. In chapter two we also practiced different techniques of picking S-wave first arrivals, which enhanced the accuracy of first-arrivals pickings. A couple of empirical equations on estimating elastic moduli from their dynamic recordings were examined. Most past studies formulised the hard rocks and only a few of the equations ranged for weak rocks and sandstones; however, some show good correlation with our measured elastic moduli. The results of chapter two also show that non-destructive acoustic tests can estimate accurate UCS values. To estimate this value, the velocity of P-waves at ambient is recorded, and this cheap and fast experiment can easily be conducted at rock mechanical labs. We tested the accuracy of literature equations for sandstones and more comprehensive tests covering a vast variety of rock types are recommended to better evaluate this method.

To study the effect of stress and saturation on anisotropy parameters, a typical reservoir sample was chosen to be studied against pure TI engineered material with elliptical anisotropy. The reason for this comparison was to investigate whether the nominated reservoir rock possessed elliptical anisotropy (weak anisotropy). The results of chapter four show that full saturation and hydrostatic stress eventually reduce the degree of anisotropy for porous, anisotropic reservoir rock. This corresponds to the closure or filling of the pores and cracks inside the rock matrix. This experiment set a good example for the effect of pore presence on the total anisotropy degree of a medium.

In the last stage of our experimental study, we planned to record the localised velocity of a sandstone by use of Laser Doppler Interferometry (LDI) as a receiver. In the first round we had to make sure the recorded first arrivals of P- and S-waves by LDI were accurate and to do that we measured couple of points in the zone of equal diameter of the transmitter source on the sample. By averaging the recorded wavelets and comparing the end result with the standard wavelet extracted by a pair of transducers we determined that both results were almost identical; therefore, LDI can be considered as a local receiver that reflected the local micro-structure on the rocks. This finding sheds light on the possibility of using the LDI technique measure accurate velocities of both P- and S-waves for samples, and the small size of the laser beam enables measurement over the irregular bodies of samples with a much smaller area. The displacement caused by the P- and S-waves was measured on the opposite surface of the sample from the source location by this technique. This displacement was then mapped, and the results show the bi-polarity of the source transducer as the first impact point.

6.2 Recommendations for future work

Chapter 2 presents the results of the measurement of static and dynamic moduli for various sandstones subjected to an isotropic and uniaxial stress regime. The elastic moduli of these samples were simultaneously measured by strain gauges and ultrasonic transducers. Thus, these samples were under exactly the same stress condition. The results then were compared with existing empirical equations that relate static moduli to dynamic measurements. Although many experiments have been reported by others previously and in this thesis, there is still a significant gap in

understanding the relationship between static and dynamic moduli. Empirical relationships between static and dynamic moduli will contribute to this important understanding. Most empirical equations are created for igneous and consolidated sedimentary rocks; few of them represent soft rocks. Acoustic measurements are less expensive and, most importantly, non-destructive, and can be performed on rocks of different shapes. Therefore, we suggest future studies investigate a broader group of sandstones to derive more accurate equations for each type of sandstone, focusing on a sample's microstructure. This will close the gap between experimental data and the current empirical relationships used by industry. We think that will be beneficial to geo-mechanical and geophysical communities.

Chapter three demonstrates that P-and S-wave velocity depends on the strain amplitude produced inside the wave. We show the technique of directly measuring this effect by LDI and not relying on old estimations. Our results for P-wave velocity dependence with strain contradict previously reported results; however, for S-wave velocity they are in agreement with the literature. More theoretical studies are recommended to understand and explain this phenomenon, especially for P-wave velocity dependence. Our study only covers a limited number of sandstones and to drive a more general pattern it is highly recommended that this technique is used on soft and hard rocks to expand the inventory of samples. To study this phenomenon we were eager to observe the effect on a non-disturbed system so we performed the measurement at ambient conditions. We recommend further study of this effect while the sample is subjected to stress to evaluate the influence of pore spaces on strain amplitude effect for the S- and P-wave velocities. In either case (an increase or decrease in velocity), this effect should be taken into account in all rock physics experiment.

In Chapter four we present the results of a case study for stress and fluid effect on anisotropy parameter of a reservoir rock from the Harvey CCS site. We observed that for non-saturated samples anisotropy is decreasing with applying hydrostatic stress, stress possibly due to pores and micro cracks closure. Anisotropy becomes elliptical by increasing of applied hydrostatic stress. Where the most enlarged pore spaces is expected. Water saturated sample has elliptical anisotropy at all stress levels. We observed that in intermediate isotropic stress the anisotropy parameter decreases to

elliptical anisotropy however to study the effect of pores higher level of stress >100 MPa is recommended to have the assumption of full closure of pores and micro structures. This allows rock physical models to be examine by such experimental data as in most of the theoretical models the full closure of the pores is a requirement. We also recommend to use LDI as the receiver to measure the wave's velocity at different angles which in that case the study could be conducted on one sample which adds to the accuracy of the data. Future work could include extending the measurement to orthorhombic symmetry class and linking the experimental data to anisotropic rock physical models.

In Chapter five we investigate uniformity of waves arrives on the surface of the samples. We measure the first wave arrivals by LDI in different locations. We compared this results with the results produced by a large receiver ultrasonic transducer. We did the three-component measurements by LDI and calculated the displacement in X, Y and Z direction caused by ultrasonic wave. The results of this study showed that for P-wave produced by shear transducer the source has dipole structure. This study also demonstrates that by increasing the number of measurements of local velocity by LDI, such technique can provide enough accuracy to substitute the receiver ultrasonic transducer. LDI technique as a receiver allows to detect wave arrivals in local area on the samples, thus we think that implementation of LDI technique in the future will allow to investigate the effect of micro structure on wave propagation for sample with different shapes.

Every reasonable effort has been made to acknowledge the owners of copyright material. I would be pleased to hear from any copyright owner who has been omitted or incorrectly acknowledged.

Appendix 1: Nomenclature

<i>Term</i>	<i>Description</i>
3C	Three components
C_{ij}	Stiffness components in Voigt matrix notation
C	Elastic stiffness tensor
CCS	Carbon Capture and Storage
E	Young's modulus
G	Shear modulus
HTI	Horizontal Transverse Isotropy
K	Bulk modulus
LVDT	Linear Variable Differential Transformer
LDI	Laser Doppler Interferometry
MHz	Mega Hertz
MPa	Mega Pascal (SI unit of pressure)
R^2	Regression coefficient accuracy (1 indicates a perfect fit)
P_c	Confine pressure
P_{eff}	Effective pressure
P_p	Pore pressure
PMMA	Poly(methyl methacrylate): acrylic (isotropic reference material)
TI	Transverse isotropy
V_p	P-wave velocity
V_s	S-wave velocity
VTI	Vertical transverse isotropy
γ	Thomsen parameter for S-wave anisotropy
ν	Poisson's ratio
δ	Thomsen parameter which controls near angular velocity range
ϵ	Thomsen parameter for P-wave anisotropy
ϵ_{axial}	Axial strain
$\epsilon_{diametric}$	Diametric (lateral) strain
μs	Micro second
θ	Incident angle
ρ	Density

σ	Stress
φ	Porosity

Table A1, Nomenclature: description of terms used in this thesis.



Title: Research note: the effect of strain amplitude produced by ultrasonic waves on its velocity
Author: Nazanin Nourifard, Maxim Lebedev
Publication: Geophysical Prospecting
Publisher: John Wiley and Sons
Date: Aug 8, 2018

© European Association of Geoscientists & Engineers

Logged in as:
 Nazanin Nourifard
 Account #:
 3001449382

LOGOUT

Order Completed

Thank you for your order.

This Agreement between ARRC/CSIRO Building, 26 Dick Perry Avenue, Kensington ("You") and John Wiley and Sons ("John Wiley and Sons") consists of your license details and the terms and conditions provided by John Wiley and Sons and Copyright Clearance Center.

Your confirmation email will contain your order number for future reference.

[printable details](#)

License Number	4587500697735
License date	May 14, 2019
Licensed Content Publisher	John Wiley and Sons
Licensed Content Publication	Geophysical Prospecting
Licensed Content Title	Research note: the effect of strain amplitude produced by ultrasonic waves on its velocity
Licensed Content Author	Nazanin Nourifard, Maxim Lebedev
Licensed Content Date	Aug 8, 2018
Licensed Content Volume	67
Licensed Content Issue	4
Licensed Content Pages	8
Type of use	Dissertation/Thesis
Requestor type	Author of this Wiley article
Format	Electronic
Portion	Full article
Will you be translating?	No
Title of your thesis / dissertation	Effect of stress magnitude and stress rate on elastic properties of the reservoir rocks
Expected completion date	Jun 2019
Expected size (number of pages)	150
Requestor Location	ARRC/CSIRO Building, 26 Dick Perry Avenue, Kensington 26 Dick Perry Avenue, Kensington

Perth, WA 6152
Australia
Attn: ARRC/CSIRO Building, 26 Dick Perry Avenue,
Kensington

Publisher Tax ID

EU826007151

Total

0.00 AUD

Copyright © 2019 [Copyright Clearance Center, Inc.](#) All Rights Reserved. [Privacy statement](#). [Terms and Conditions](#).
Comments? We would like to hear from you. E-mail us at customercare@copyright.com

Taylor & Francis
Taylor & Francis Group**Title:** The effect of wave amplitude on S-wave velocity in porous media: an experimental study by Laser Doppler Interferometry**Author:** Nazanin Nourifard, , Eduard Mashinskii, et al**Publication:** Exploration Geophysics**Publisher:** Taylor & Francis**Date:** Oct 1, 2019

Rights managed by Taylor & Francis

LOGIN

If you're a [copyright.com](#) user, you can login to RightsLink using your [copyright.com](#) credentials.

Already a [RightsLink](#) user or want to [learn more?](#)

Thesis/Dissertation Reuse Request

Taylor & Francis is pleased to offer reuses of its content for a thesis or dissertation free of charge contingent on resubmission of permission request if work is published.

BACK

CLOSE WINDOW

Copyright © 2019 [Copyright Clearance Center, Inc.](#) All Rights Reserved. [Privacy statement.](#) [Terms and Conditions.](#) Comments? We would like to hear from you. E-mail us at customercare@copyright.com